

UNIVERSITÀ DEGLI STUDI DI PADOVA

Dipartimento di Fisica e Astronomia “Galileo Galilei”

Master Degree in Physics of Data

Final Dissertation

Simulation studies for a double-crystal channeling

experiment at the LHC

Thesis supervisor

Dr. Massimiliano Ferro-Luzzi

Candidate

Chiara Maccani

Thesis co-supervisor

Prof. Marco Zanetti

Academic Year 2022/2023

Contents

1	Introduction	1
2	The Experiment	3
2.1	Physics background	3
2.1.1	Magnetic Dipole Moment	3
2.1.2	Electric Dipole Moment	4
2.1.3	The Λ_c^+ particle and its electromagnetic moments	6
2.2	The experimental principle: measuring spin precession through bent crystals	8
2.2.1	Physical motivation	8
2.2.2	The measurement method	9
2.2.3	Λ_c^+ production, polarization and decays	11
2.3	Crystal Channeling	13
2.3.1	Electric Field in a Channel	13
2.3.2	Channeling in Straight Crystals	16
2.3.3	Channeling in Bent Crystal	17
2.3.4	Dechanneling	18
2.3.5	Other crystal processes: Volume Capture and Volume Reflection	19
2.4	Layout of the Experiment and of the Proof of Principle	22
2.4.1	Proof of Principle	25
2.4.2	Crystals and Target	26
2.4.3	LHCb VELO Pixel Detector	27
3	Simulation Framework	31
3.1	Simulation Software Description	31
3.1.1	DD4hep	31
3.1.2	Geant4	32
3.1.3	DDG4: the DD4hep interface to Geant4	34
3.1.4	Crystal Channeling routine in Geant4	34
3.2	IR3 Detector implementation in DD4hep	38
3.2.1	Introduction of the Channeling routine in DD4hep	39
3.2.2	Development of new plugins for the IR3 detector simulation	39
4	Proof of Principle tests	45
4.1	CPU time analysis	45
4.2	Simulations without the target	50
4.2.1	Signal and background analysis of 2000 events simulation	50
4.2.2	VELO Noise	57
4.3	Preliminary simulations with the target	58
4.3.1	Channeling studies with an analytical approach	62
5	Conclusions	67

Introduction

Magnetic and Electric Dipole Moments (MDMs and EDMs) are important static properties of particles that determine their behavior, along with charge, spin, mass, and lifetime. The study of these properties is fundamental to contributing to the understanding of the structure of matter and fundamental interactions. Numerous experiments have been conducted to study the MDM of various elementary particles, confirming, for example, the composite nature of protons and neutrons. In this scenario, precise measurements of baryon magnetic moments would serve as valuable tools for imposing constraints on hadronic structure models and offer crucial insights into the nature of hadron constituents.

Since both electromagnetic moments are defined to be proportional to the spin of the particle, that can interact with external electromagnetic fields, and given their behaviour under discrete symmetries transformations, the EDM turns out to be a direct signal of parity symmetry and time-reversal symmetry violation. Relying on the CPT theorem of relativistic field theories, this implies that the observation of a non-zero EDM is also a CP violation signal. CP violation is required as one of Sakharov's conditions [1] to explain baryon asymmetry, which is responsible for the presence of more matter than antimatter in the universe. The Standard Model of particle physics (SM) includes CP violation through the CKM mechanism; however, its predictions are not quantitatively sufficient to explain the amount of the observed asymmetry, so extensions of the model that include new CP-violating interactions are needed. Nowadays, CP violation of the SM model needs to be tested to high accuracy, since any deviation from the prediction, including a nonzero EDM, would be a clear sign of new physics. The baryon EDM is highly suppressed in the SM but there exist some extension in which it can be enhanced.

Recently, an experiment has been proposed at LHC to directly measure the EDM and MDM of quark charm-containing baryons. This consists in a fixed-target experiment that aims to use bent crystals to induce spin precession of short-lived baryons by exploiting a crystal lattice phenomenon called channeling in order to measure electromagnetic dipole moments. Another bent crystal is used to deflect protons from the main beam halo onto the target.

Prior to Long Shutdown 3 of the LHC, a proof-of-principle is planned to be carried out to verify the feasibility of the experimental idea. It is necessary, therefore, to carry out simulations of the experimental setup to advance the design and implementation.

The content of this thesis summarises the work done to integrate the channelling routine into the simulation framework chosen by the collaboration which is designing the experiment, and reports the results of some preliminary simulations of the first type of measurements that will be performed during the proof of principle. In Chapter 1, an overview of the physics background is given and the concept of the experiment is described in detail. In Chapter 2, the simulation framework is explained and all the upgrades that have been brought to the software are described. In Chapter 3, the results of the preliminary simulations are shown.

The Experiment

2.1 Physics background

The following sections are meant to give an insight on the physics under study and on its application to the Λ_c^+ baryon.

2.1.1 Magnetic Dipole Moment

The *magnetic dipole moment* (MDM) measures the strength and orientation of the magnetic field generated by the motion of electric charges or by intrinsic magnetism of matter.

Assuming natural units $\hbar = c = 1$, the magnetic dipole moment of a spin- $\frac{1}{2}$ particle of mass m and charge Q is defined as

$$\boldsymbol{\mu} = g \frac{eQ}{2m} \mathbf{s} \quad (2.1)$$

where $\mathbf{s} = \frac{\sigma}{2}$ represents the spin operator (with σ the Pauli matrices), while g is called *gyromagnetic factor* or *g-factor*. According to Dirac theory, the magnetic moment of point-like fermions is predicted to be exactly equal to 2. However, quantum loop effects can modify this value, leading to a deviation known as the anomalous MDM. This deviation is particularly important because it can reveal the presence of new physics, such as the propagation of new particles in the loop. Therefore, it is crucial to measure the MDM with high precision in order to gain insight into the underlying physics. Furthermore a measure of g far from 2 is an indication of the substructure of a particle.

In the quark model description, mesons are assumed to be bound states of quark and anti-quark while baryons are bound states of three quarks. The magnitude of the MDM of a quark $q = u, d, \dots$ is expressed as

$$\mu_q = g_q \frac{eQ_q}{2m_q} \quad . \quad (2.2)$$

Therefore, the magnetic dipole moment of a baryon B can be computed as a sum of the MDMs of the three constituent quarks

$$\mu_B = \langle B; J, J_z | \mu_1 \sigma_{1z} + \mu_2 \sigma_{2z} + \mu_3 \sigma_{3z} | B; J, J_z \rangle \quad . \quad (2.3)$$

where μ_i is the magnetic moment of the i -th quark in Eq. (2.2) and $|B; J, J_z\rangle$ the baryon's spin-flavor wave function in the quark model description.

Determining if the quark g -factor is in agreement with Dirac theory is not trivial: in fact what can be effectively measured in experiments is the ratio g_q/m_q , so the determination of g depends on the assumption of the constituent quark mass and its uncertainty.

The interaction between the magnetic dipole moment $\boldsymbol{\mu}$ and an external magnetic field \mathbf{B} is described by the Hamiltonian defined as the negative scalar product between the dipole and the field, i.e. $\mathcal{H} = -\boldsymbol{\mu} \cdot \mathbf{B}$.

2.1.2 Electric Dipole Moment

The *electric dipole moment* (EDM) of a system measures the separation of the positive and negative electric charge distribution. In classical mechanics the EDM of a charge distribution $\rho(\mathbf{r})$ is defined as $\boldsymbol{\delta} = \int \rho(\mathbf{r}) \mathbf{r} d^3 r$. Its interaction with an external electric fields \mathbf{E} can be described by an Hamiltonian to that defined for the magnetic case, i.e. $\mathcal{H} = -\boldsymbol{\delta} \cdot \mathbf{E}$.

In a quantum system, the EDM of a particle of mass m and charge Q is defined proportional to the spin operator \mathbf{s} and to a constant d :

$$\boldsymbol{\delta} = d \frac{eQ}{2m} \mathbf{s} . \quad (2.4)$$

As with any vector-like quantity in a subatomic system, the electric dipole moment and the magnetic dipole moment (which also depends on \mathbf{s} , see Eq.(2.1)) must be either parallel or anti-parallel to the spin. Under parity (P) and time-reversal (T) discrete transformations, the magnetic moment interaction is invariant, as both the spin and the magnetic field transform in the same way as axial vectors, while the electric dipole interaction violates both symmetries separately, as \mathbf{E} transforms as a polar vector:

$$\begin{aligned} \mathcal{H} = -\boldsymbol{\mu} \cdot \mathbf{B} - \boldsymbol{\delta} \cdot \mathbf{E} &\xrightarrow{P} \mathcal{H} = -\boldsymbol{\mu} \cdot \mathbf{B} + \boldsymbol{\delta} \cdot \mathbf{E} \\ \mathcal{H} = -\boldsymbol{\mu} \cdot \mathbf{B} - \boldsymbol{\delta} \cdot \mathbf{E} &\xrightarrow{T} \mathcal{H} = -\boldsymbol{\mu} \cdot \mathbf{B} + \boldsymbol{\delta} \cdot \mathbf{E} . \end{aligned} \quad (2.5)$$

This means that, if parity and time-reversal transformations are symmetries of the physical laws, fundamental particles must have zero electric dipole moment. Hence, any measurement of a permanent EDM $\boldsymbol{\delta} \neq 0$ would require the violation of P and T symmetries and thus, relying on the validity of the CPT theorem, the violation of CP symmetry. Figure 2.1 shows the effects of the application of P and T symmetries on the vectors \mathbf{s} , $\boldsymbol{\mu}$ and $\boldsymbol{\delta}$.

In the Standard Model any contribution to an EDM is highly suppressed (e.g. the SM theoretical limit for the neutron δ_n is of the order of $10^{-31} e \text{ cm}$ [2]) but there exist some extension of the SM in which it can be enhanced, with the inclusion in the model of new sources of CP violation, in addition to those known (CKM phase in the weak sector and Θ -QCD term in the strong sector). In the case of baryons, an EDM could arise from a collective CP-violation interaction of its constituent quark and gluon fields with the electromagnetic field. Figure 2.2 shows the current status of EDM predictions and measurements [3]. As an example, the current experimental upper limit for the neutron is $\delta_n \leq 3.0 \cdot 10^{-26} e \text{ cm}$ [4].

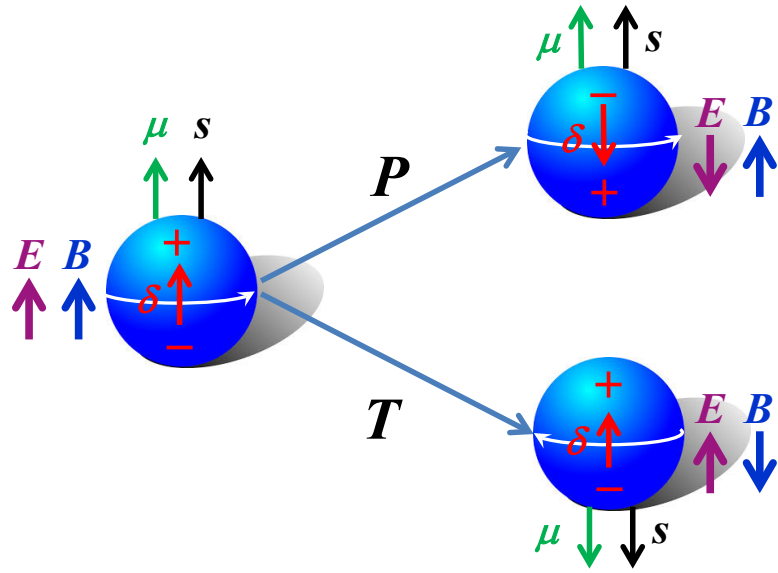


Figure 2.1: Representation of particle with spin \mathbf{s} and of its magnetic dipole moment $\boldsymbol{\mu}$ and electric dipole moment $\boldsymbol{\delta}$, where the latter describes the charge distribution. Under parity (P) and time-reversal (T) transformations, it is shown that the external magnetic field \mathbf{B} transforms together as \mathbf{s} , differently from the external electric field \mathbf{E} , which violates both symmetries. From Ref. [5].

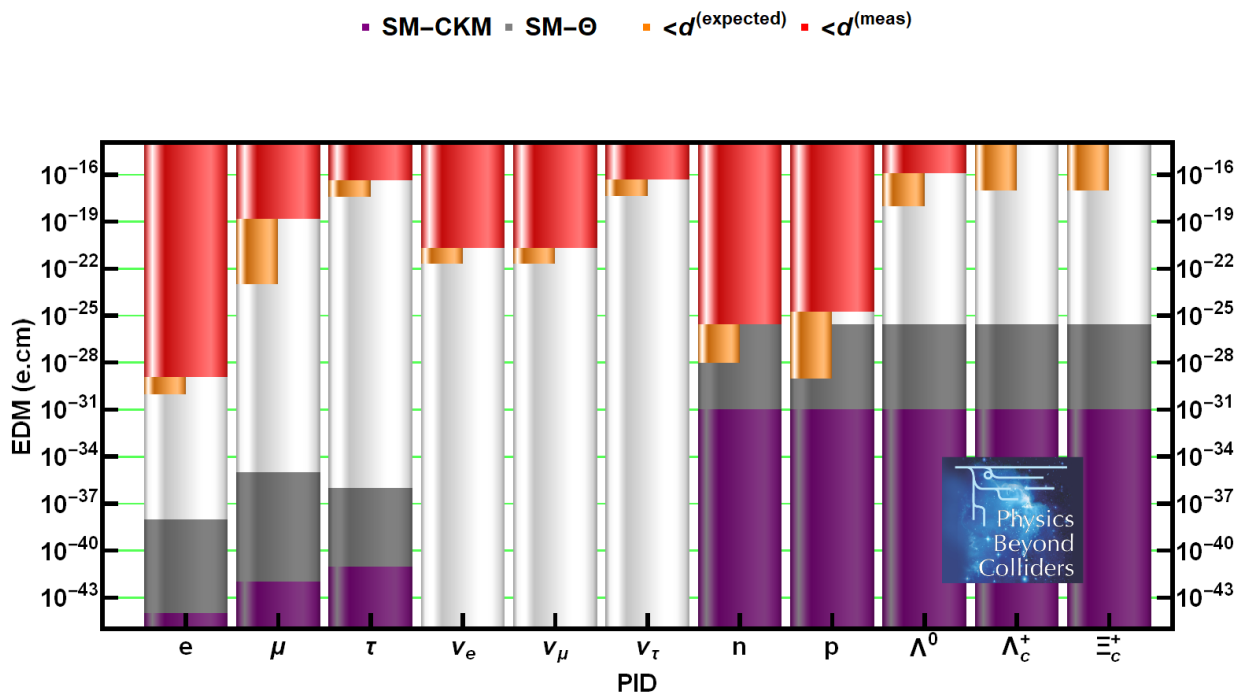


Figure 2.2: Current status of electric dipole moment measurements of leptons, neutrinos, proton, neutron, Λ and charmed baryons. From the top, the experimental limits on EDMs are represented with red bars and indirect limits derived from other measurements as orange bars. From below, the SM estimates from CKM CP-violation and Θ -QCD interaction term are represented respectively with violet and grey bars. For what concern charmed baryons, no direct measurements are currently available. From Ref. [3]

2.1.3 The Λ_c^+ particle and its electromagnetic moments

The Λ_c^+ particle is a charmed baryon composed by (u,d,c) , observed for the first time in 1975 in a bubble chamber exposed to a neutrino beam [6]. It is characterized by isospin quantum number $I = 0$ and spin-parity $J^P = \frac{1}{2}^+$. According to what is currently stated by the *Particle Data Group* [7], its mass is measured to be $m_{\Lambda_c^+} = 2286.46 \pm 0.14$ MeV (Babar Collaboration [8]) and its mean life is measured to be $\tau_{\Lambda_c^+} = (2.015 \pm 0.027) \cdot 10^{-13}$ s, that corresponds to a life length of $L_{\Lambda_c^+} = 60.0 \pm 1.2 \mu\text{m}$.

In general, the quark model predicts that baryons composed of u, d, s and c quarks can be organized into $SU(4)$ multiplets based on the symmetry of their flavor, spin, and spatial wavefunctions. The addition of the c quark to the light quarks u, d, s extends the flavor symmetry from $SU(3)_f$ to $SU(4)_f$. As a result, the ground state baryons that were previously arranged into a spin- $\frac{1}{2}$ octet and a spin- $\frac{3}{2}$ decuplet are now represented into a spin- $\frac{1}{2}$ 20-plet and a spin- $\frac{3}{2}$ 20-plet, respectively. By introducing the additive charm quantum number C , the baryons can be classified in a 3-dimensional representation with three coordinates (I_z, Y, C) , where I_z is the third component of isospin and Y the hypercharge. Having $J^P = \frac{1}{2}^+$ and $C = 1$, Λ_c^+ particle belongs to the spin- $\frac{1}{2}$ 20-plet shown in Figure 2.3.

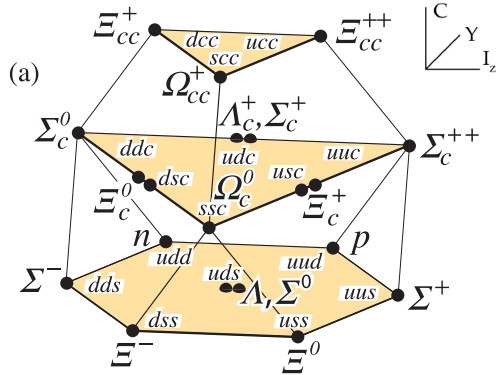


Figure 2.3: Diagram of the $SU(4)_f$ spin- $\frac{1}{2}$ 20-plet of baryons qqq made of u, d, s and c quarks. It extends the charmless $SU(3)_f$ octet, here represented in the lowest level of the diagram, including charmed particles with quantum number $C = 1, 2$ represented respectively in the second and third level. From Ref. [7].

The Pauli exclusion principle requires the overall wave function of a fermion to be antisymmetric, including both the spatial part (which describes the location of the quarks and is symmetric in the ground state) and the color part (which must be antisymmetric since every particle is a color singlet). This implies the spin-flavor part to be completely symmetric. Single-charmed baryons with charm quantum number $C = 1$ can be viewed as composed of a heavy c quark and a light diquark made of u, d, s quarks. From the flavor perspective, the diquark can be decomposed into an antisymmetric triplet and a symmetric sextuplet. So, for ground-state baryons, overall antisymmetry requires the light diquark to be symmetric under the exchange of spin and flavor, meaning that they must both be either symmetric or antisymmetric. Then, the antisymmetric triplet combines with the c quark to form $J^P = 1/2^+$ states, while the symmetric sextuplet combines with the c quark to form $J^P = 1/2^+$ or $J^P = 3/2^+$ states.

Therefore, considering Λ_c^+ quantum numbers, its spin-flavour wave function [9] is constructed by composing the antisymmetric flavour function $\psi_{f,\Lambda_c^+} = \frac{1}{\sqrt{2}}[u, d]c$ with the antisymmetric spin function $\psi_s = \frac{1}{\sqrt{2}}(\uparrow\downarrow\uparrow - \downarrow\uparrow\uparrow)$, obtained from $SU(2)$ decomposition and assuming $J = 1/2$ and $J_z = 1/2^+$.

This can be written as:

$$\left| \Lambda_c^+; \frac{1}{2}, +\frac{1}{2} \right\rangle = \frac{1}{2} (u_\uparrow d_\downarrow c_\uparrow - u_\downarrow d_\uparrow c_\uparrow - d_\uparrow u_\downarrow c_\uparrow + d_\downarrow u_\uparrow c_\uparrow) \quad (2.6)$$

The magnetic dipole moment is defined as

$$\mu_{\Lambda_c^+} = \frac{g_{\Lambda_c^+}}{2} \frac{e}{2m_{\Lambda_c^+}} . \quad (2.7)$$

Applying Eq. (2.3), the MDM of Λ_c^+ in the quark model results to be equal to the charm quark MDM:

$$\mu_{\Lambda_c^+} = \mu_c = \frac{g_c}{2} \frac{2/3 e}{2m_c} . \quad (2.8)$$

This means that a measure of $\mu_{\Lambda_c^+}$ can be translated into a measure of the charm gyromagnetic factor and its anomaly. If this quark behaves as a point-like Dirac particle, then the corresponding gyromagnetic factor g_c is equal or close to 2, while if the charm quark has a composite structure we can expect a sizable deviation from this value. Note that this result would suffer of systematic error due to the charm mass ambiguity $m_c = 1.5 \pm 0.3$ GeV.

Beyond the quark model, there exist many model predictions of the baryon MDM which are sensitive to the interactions of heavy quark and photons within the hadron (e.g. QCD sum rules, QCD spectral sum rules, chiral perturbation theory and others). These theoretical results often obtain the charm quark mass from other observables. For Λ_c^+ , MDM predictions lay in the range [10] (written in terms of the nuclear magneton μ_N units):

$$\mu_{\Lambda_c^+} = (0.34 - 0.43)\mu_N, \quad \mu_N = \frac{e}{2m_p} . \quad (2.9)$$

In 2017 the BESIII Collaboration reported the measurements of the amplitudes of transitions in the cascade radiative decays of charmonium $\psi(2S)$ produced from e^+e^- collisions [11], from which an estimation of $g_c/2m_c$ can be extracted. Given the relation (2.8), this experimental result can provide a prediction of the Λ_c^+ magnetic dipole moment in the constituent quark model, without any charm quark mass uncertainty [10]:

$$\frac{g_c}{2m_c} = 0.76 \pm 0.05 \text{ GeV}^{-1}, \quad \mu_{\Lambda_c^+} = \mu_c = \frac{g_c}{2m_c} \frac{2}{3} m_p \mu_N = (0.48 \pm 0.03)\mu_N . \quad (2.10)$$

This indirect experimental result is found to be in tension with most of the theoretical predictions. In this prospective, a direct measure of Λ_c^+ MDM at high precision turns out to be a relevant and decisive result in determining the approach to this type of study.

For what concerns the EDM, an indirect bound on the charm quark EDM is derived from the experimental limit on the neutron EDM to be $\delta \leq 4.4 \cdot 10^{-17} e \text{ cm}$ [12], and a prediction of comparable magnitude is possible in extensions of the SM [13]. By now, no direct measurements exist for charmed baryons EDM, as showed in Figure 2.2, underlying the importance of the experimental proposal under study.

2.2 The experimental principle: measuring spin precession through bent crystals

2.2.1 Physical motivation

One of the main experimental methods to study electromagnetic moments in high energy physics consists of measuring the polarization vector of the incoming particles and the precession angle when the particle is travelling through an intense electromagnetic field. In the non-relativistic approximation, the polarization precession in an electromagnetic field \mathbf{E}^* and \mathbf{B}^* expressed in the rest frame of the particle is defined as:

$$\frac{ds}{d\tau} = \boldsymbol{\mu} \times \mathbf{B}^* + \boldsymbol{\delta} \times \mathbf{E}^* \quad (2.11)$$

where \mathbf{s} , $\boldsymbol{\mu}$ and $\boldsymbol{\delta}$ are, respectively, the expectation values of the spin, MDM and EDM operators. The final polarization can be evaluated by analyzing the angular distribution of the decay products.

To perform such measurements, it is necessary to design an experiment that can provide the following three fundamental elements: a polarized-particles source, an intense electromagnetic field able to induce a measurable spin precession and a detector capable to reconstruct the final polarization from the particle's decay products. The main problem encountered when applying this method to charmed baryons consists in the fact that their lifetime (of order 10^{-13} s) results to be too short compared to the time needed by the conventional electromagnetic fields to induce a sizable spin precession, preventing the possibility of performing a direct measurement.

This issue can be solved by exploiting the channeling process in a bent crystal (described in Sect.2.3): relativistic particles can be trapped into the intense crystal interatomic electric field \mathbf{E} (in the laboratory frame) of order 10^{11} V/m, which translates into a strong electromagnetic field in the instantaneous rest frame of the particle:

$$\mathbf{E}^* \approx \gamma \mathbf{E}, \quad \mathbf{B}^* \approx -\gamma \beta \times \frac{\mathbf{E}}{c}. \quad (2.12)$$

Producing the charmed baryons in proton on nucleus fixed-target interactions, harnessing the power of the LHC, the Lorentz boost factor γ of the produced charm baryons can achieve values up to 1000, which results into a amplification of the fields in the baryon rest frame and into a dilation of the baryon lifetime. In these conditions, the motion of channeled relativistic baryons in the interplanar electric field of a crystal bent at an angle θ_C imitates the particle motion in a magnetic field directed along the crystal bending axis. This magnetic field appears to be strong enough to make the polarization vector to rotate over a measurable angle Φ before the particle decays (Figure 2.4).

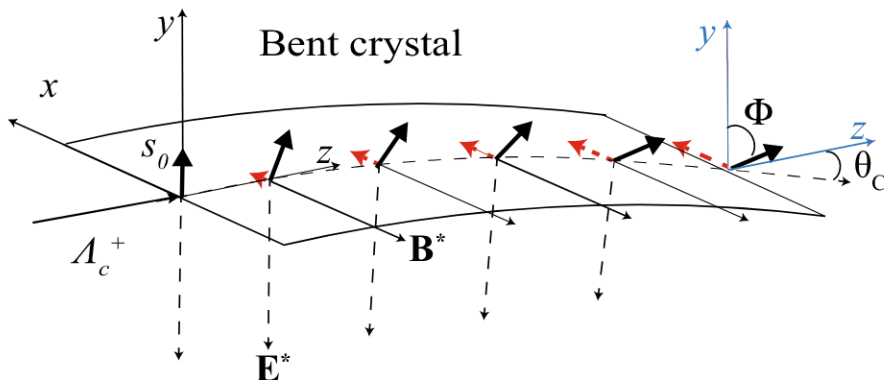
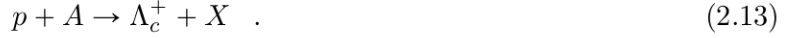


Figure 2.4: Diagram of the spin precession of the initial polarization vector of magnitude s_0 inside a bent crystal of bending angle θ_C . The fields \mathbf{B}^* and \mathbf{E}^* are, respectively, the magnetic and electric fields expressed in the instantaneous rest frame of the particle and the spin-precession angle is denoted as Φ . Red dashed arrows represent the precession component proportional to the particle electric dipole moment, that appears if a non-zero EDM exists. From Ref. [14].

2.2.2 The measurement method

In fixed-target experiments, polarized charm baryons can be produced through the interaction of the high-energy proton beam with a target composed of nuclei A .



Because of the conservation of parity in the strong interaction, the initial polarization vector $s_0 = (0, s_0, 0)$ of the charm baryon is initially along the y axis, perpendicular to the production plane xz defined by the proton and baryon momenta, where the z axis is defined by the latter (Figure 2.5).

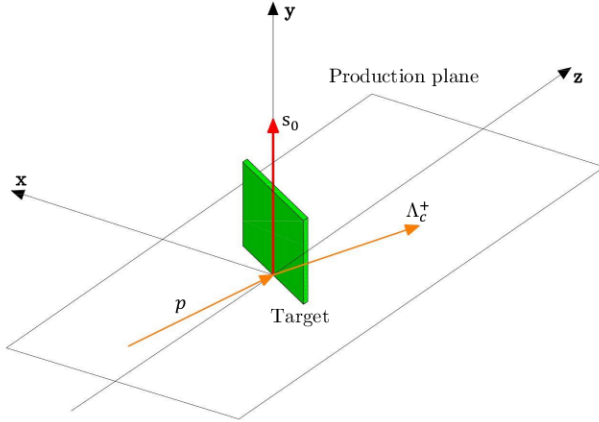


Figure 2.5: Representation of the production plane of the Λ_c^+ and its initial spin-polarization vector. The vector s_0 is generated in the interaction of protons with the target perpendicular to the production plane and, thus, parallel to the y axis, due to parity conservation in strong interactions. From Ref. [14].

The time evolution of the spin-polarization vector \mathbf{s} in an external electromagnetic field is regulated by the Thomas–Bargmann–Michel–Telegdi (T-BMT) equation:

$$\frac{d\mathbf{s}}{dt} = \mathbf{s} \times \boldsymbol{\Omega}, \quad \boldsymbol{\Omega} = \boldsymbol{\Omega}_{MDM} + \boldsymbol{\Omega}_{EDM} + \boldsymbol{\Omega}_{TH} \quad (2.14)$$

where t is the time in the laboratory frame, and the precession angular velocity vector $\boldsymbol{\Omega}$ has been split into three elements corresponding to the MDM, EDM and Thomas contributions:

$$\begin{aligned} \boldsymbol{\Omega}_{MDM} &= \frac{g\mu_B}{\hbar} \left(\mathbf{B} - \frac{\gamma}{\gamma+1} (\boldsymbol{\beta} \cdot \mathbf{B}) \boldsymbol{\beta} - \boldsymbol{\beta} \times \mathbf{E} \right), \\ \boldsymbol{\Omega}_{EDM} &= \frac{d\mu_B}{\hbar} \left(\mathbf{E} - \frac{\gamma}{\gamma+1} (\boldsymbol{\beta} \cdot \mathbf{E}) \boldsymbol{\beta} + \boldsymbol{\beta} \times \mathbf{B} \right), \\ \boldsymbol{\Omega}_{TH} &= \frac{\gamma^2}{\gamma+1} \boldsymbol{\beta} \times \frac{d\boldsymbol{\beta}}{dt} \\ &= \frac{q}{mc} \left[\left(\frac{1}{\gamma} - 1 \right) \mathbf{B} + \frac{\gamma}{\gamma+1} (\boldsymbol{\beta} \cdot \mathbf{B}) \boldsymbol{\beta} \right. \\ &\quad \left. - \left(\frac{1}{\gamma+1} - 1 \right) \boldsymbol{\beta} \times \mathbf{E} \right], \end{aligned} \quad (2.15)$$

with \mathbf{B} and \mathbf{E} expressed in the laboratory frame.

By integrating Eq.(2.14) in time, the spin evolution equation $\mathbf{s}(t)$ can be derived for positive baryons in bent crystals (where the electric potential is assumed to be harmonic, and the magnetic field in crystals in the laboratory frame is zero). The complete derivation can be found in the Appendix of [14]. Assuming that a channeled particle travels at a speed of $\approx c$ inside the entire length L of the crystal without decaying and remaining in the channeling status, the final polarization vector at the exit can be obtained as follows

$$\begin{cases} s_x \approx s_0 \frac{d}{g-2} (\cos \Phi - 1) \\ s_y \approx s_0 \cos \Phi \\ s_z \approx s_0 \sin \Phi \end{cases} \quad (2.16)$$

where Φ represents the spin precession angle in the yz plane, in the limit of large boost:

$$\Phi \approx \frac{g-2}{2} \gamma \theta_C \quad (2.17)$$

with θ_C crystal bending angle. In [15] it is demonstrated that identical equations can be derived also in presence of a non-harmonic potential and that the spin precession depends only on the crystal curvature.

From Eq.(2.16) it can be observed that in absence of EDM, i.e. $d = 0$, the spin precession inside the bent crystal occurs in the yz plane, while if a non-zero EDM exists, also a s_x component proportional to the particle EDM is present (red dashed arrows in Figure 2.4). EDM effects are assumed to be small compared to the main MDM ones.

The orientation of the baryon polarization vector after passing through the crystal can be determined by analyzing the angular distribution of its decay products. In the case of weak decays of spin- $\frac{1}{2}$ baryons into two-particle final states consisting of a baryon and a meson ($\frac{1}{2} \rightarrow \frac{1}{2} + 0, \frac{1}{2} \rightarrow \frac{1}{2} + 1, \frac{1}{2} \rightarrow \frac{3}{2} + 0$), the amplitude decay calculations allow us to derive the following relation for the angular distribution in the solid angle Ω (see the Appendix of [16] for the complete derivation)

$$\frac{dN}{d\Omega} \propto 1 + \alpha_f \mathbf{s} \cdot \hat{\mathbf{k}} \quad (2.18)$$

where α_f is the parity-violating coefficient depending on the final state, $\hat{\mathbf{k}}$ the direction of the final state baryon in the initial state baryon helicity frame, Ω the corresponding solid angle, and \mathbf{s} the initial baryon polarization vector. The charm hadron flight length and direction are determined by reconstructing the production and the decay vertex positions and its momentum can be estimated by reconstructing the decay kinematics.

Finally, the values of the factors d and g , associated respectively to EDM and MDM, can be evaluated as

$$\begin{aligned} d &\approx \frac{(g-2)A_x}{\alpha_f s_0 (\cos \Phi - 1)} \\ g - 2 &\approx \frac{2}{\gamma \theta_C} \arccos \left(\frac{A_y}{\alpha_f s_0} \right) \approx \frac{2}{\gamma \theta_C} \arccos \left(\frac{A_z}{\alpha_f s_0} \right) \end{aligned} \quad (2.19)$$

where the quantity $A_{x,y,z} = \alpha_f s_{x,y,z}$, called asymmetry parameter, is measured from a fit to the angular distribution of the decay products.

2.2.3 Λ_c^+ production, polarization and decays

When protons collide with a fixed target, Λ_c^+ particles are generated within an emission cone whose aperture is proportional to $1/\gamma = \pm 1$ mrad, where γ represents the boost of the center-of-momentum in the laboratory frame. The cross section $\sigma(pp \rightarrow \Lambda_c^+ X)$ has not been directly measured, but it can be estimated basing on other total charm production cross section measures. For the remainder of this work a $pp \rightarrow \Lambda_c^+$ production cross section value of $\sim 18.2 \mu\text{b}$ shall be assumed, as in [14].

The initial polarization vector is always perpendicular to the production plane, however the absolute value s_0 is unknown for Λ_c^+ particles produced by a 7 TeV beam. To determine s_0 , one would need to measure the angular distribution for unchanneled baryons. However, the proposed experiment could also estimate the absolute polarization as function of transverse momentum, since the measurement of the three components of the final polarization vector for channeled baryons allows for a simultaneous determination of g , d , and s_0 , as it is shown in Eq.(2.16). Basing on a phenomenological model used to describe experimental results provided by the E791 Collaboration [17], the initial polarization can be parameterized as a function of its transverse momentum p_T relative to the direction of the impinging proton [18]:

$$s_0 \approx A \cdot (1 - e^{-B \cdot p_T^2}) \quad (2.20)$$

where $A \approx -0.9$ and $B \approx 0.4 (\text{GeV}/c)^{-2}$. Additionally, the polarization of Λ_c^+ baryons as a function of p_T can be measured precisely in fixed-target $p - \text{Ne}$ collisions at LHCb using the SMOG system [19], which can further improve the polarization model.

Eq. (2.18) describes the angular distribution of baryon decay products in the case of two-particle final states. The parity violating parameter α_f is decay-channel dependent and it is crucial in determining the sensitivity to the initial polarization. In the Λ_c^+ case, only few decay parity violating parameters are known; in particular it has been measured only for some decay channels containing Λ or Σ^+ in the final states, such as $\Lambda_c^+ \rightarrow \Lambda(p\pi^-)\pi^+$, which was found to be $\alpha_{\Lambda\pi} = -0.84 \pm 0.09$ [7].

The three-body decay channel $\Lambda_c^+ \rightarrow pK^-\pi^+$ has a larger branching fraction compared to the other two-body decays, making it an interesting mode to exploit for electromagnetic dipole measurements. The E791 experiment [17] has reported measurements of the amplitudes for Λ_c^+ decay into nonresonant $pK^-\pi^+$, as well as into $p\bar{K}^*(890)^0$, $\Delta^{++}(1232)K^-$, and $\Lambda(1520)\pi^+$ modes. However, the decay amplitude is dominated by the sum of quasi two-body resonant contributions: $\mathcal{B}(\Lambda_c^+ \rightarrow pK^-\pi^+) \approx \mathcal{B}(\Lambda_c^+ \rightarrow pK^0) + \mathcal{B}(\Lambda_c^+ \rightarrow \Lambda\pi^+) + \mathcal{B}(\Lambda_c^+ \rightarrow \Delta^{++}K^-)$.

Amplitude analysis of Λ_c^+ decays can be used to extract the parity violating parameter α_f from Dalitz plot analysis of the $\Lambda_c^+ \rightarrow pK^-\pi^+$ decay, although with large uncertainties [14]. A Dalitz plot is a scatter plot that provides a visual representation of the phase space of a three-body decay of a particle. It shows the distribution of decay products, with the squares of the invariant masses of two pairs of decay products plotted against each other, respectively: in this case $m^2(pK^-)$ and $m^2(K^-\pi^+)$. Each point on the plot represents an event in which the parent particle decayed into the two daughter particles with the given squared masses. If there are no angular correlations between the decay products, the distribution of these variables is flat. However, if the three-body decay is dominated by resonant processes, the Dalitz plot will show a non-uniform distribution, with a peak around the mass of the resonant decay. By fitting the Dalitz plot using techniques such as maximum likelihood fits or Bayesian inference, the value of the asymmetry decay parameter can be extracted from the fit parameters.

The α_f parameters computed in [14] and the decays branching fractions [7] are listed in Table 2.1.

Λ_c^+ final state	$\mathcal{B}(\%)$	α_f
$pK^-\pi^+$	6.28 ± 0.32	unknown
$\bar{K}^*{}^0 p$	1.96 ± 0.27	-0.545 ± 0.345
$\bar{K}^*{}^0 \rightarrow K^-\pi^+$	100	—
$\Delta^{++} K^-$	1.08 ± 0.25	-0.666 ± 0.298
$\Delta^{++} \rightarrow p\pi^+$	99.4	—
$\Lambda(1520)\pi^+$	2.2 ± 0.5	-0.105 ± 0.604
$\Lambda(1520) \rightarrow pK^-$	45 ± 1	—
$\Lambda\pi^+$	1.07 ± 0.28	-0.84 ± 0.09
$\Lambda \rightarrow p\pi^-$	63.9 ± 0.5	—

Table 2.1: List of the branching fractions \mathcal{B} and of the decay parity violating parameter α_f for the decay modes $\Lambda_c^+ \rightarrow pK^-\pi^+$ and $\Lambda_c^+ \rightarrow \Lambda\pi^+$. Only $\alpha_{\Lambda\pi}$ was directly measured, the other ones are derived in [14]. The branching ratio of second level in the decay chain is reported too.

In addition, also three and four-body decays are considered in order to further increase the signal yield [18].

A pictorial description of a $\Lambda_c^+ \rightarrow pK^-\pi^+$ signal event is shown in Figure 2.6.

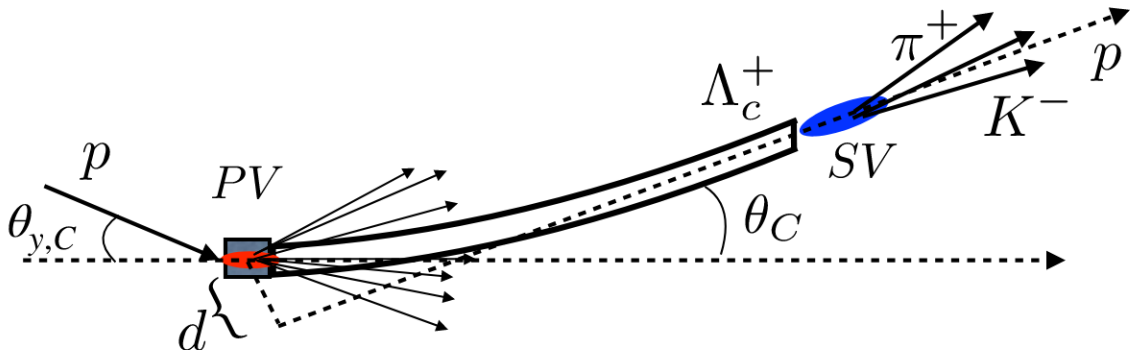


Figure 2.6: Sketch of a $\Lambda_c^+ \rightarrow pK^-\pi^+$ signal event. A proton p from the secondary halo collides with incident angle $\theta_{y,C}$ on the target where a Λ_c^+ particle is produced, defining the primary vertex (PV). The baryon is then channeled in a bent crystal of bending angle θ_C , at the end of which it decays into a three-body final state, defining the secondary vertex (SV). From Ref. [15].

2.3 Crystal Channeling

It is called *channeling* the phenomenon whereby the path of a charged particle is forced to follow the crystalline structure of a solid. Atoms in a crystal are arranged in an extremely symmetrical order, called crystal lattice, and the aligned atoms can be represented as planes or axis between which a strong electric field is present. If the crystal is well oriented with respect to an incident particle, that particle experiences an electric force that confines its trajectory between two planes (*planar channeling*) or around an axis (*axial channeling*). In this way, a positive channeled particle does not collide with nuclei but interacts coherently with them, moving in an electronic cloud characterized by a reduced density. This effect results to be very different from the case of motion in an amorphous material, where particles can undergo a large number of uncorrelated scatters with single atoms (multiple scattering) and loose energy by ionisation, colliding with atomic electrons.

In the following sections only planar channeling will be treated. Furthermore, it is important to note that all the relations given below can be evaluated using classical mechanics [20]. In what follows, unless otherwise stated, equations are taken from Ref. [21].

2.3.1 Electric Field in a Channel

Given a particular shape of the crystal elementary cell, which is repeated in space forming the lattice, a set of parallel planes can be specified by the Miller indices (hkl). Typically the materials used to build crystals for channeling application are elements of group 14 (Silicon, Germanium), characterized by a crystalline structure called *diamond cubic*. The elementary cell contains 8 atoms and the main possible planes between which a particle can be trapped are pictured in Figure 2.7.

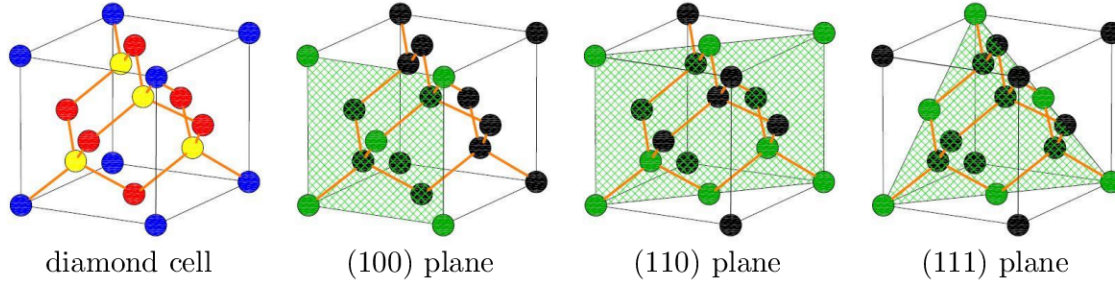


Figure 2.7: Diagram of a diamond cubic cell. It is composed by two identical face-centered lattices, pushed one into another and shifted along the bulk diagonal by one quarter of its length. The possible crystalline planes between which planar channeling can occur are shown.

The potential of the interaction between a single atom and a particle is defined by the Thomas-Fermi model:

$$V(r) = \frac{Z_i Z e^2}{r} \Phi\left(\frac{r}{a_{TF}}\right) \quad (2.21)$$

where $Z_i e$ is the charge of the incoming particle, Z the atomic number of the target atom, r the relative distance and Φ is the screening function which takes into account the electronic cloud around the nuclei. In the Moliere approximation

$$\Phi\left(\frac{r}{a_{TF}}\right) = \sum_{i=1}^3 \alpha_i \exp\left(-\frac{\beta_i r}{a_{TF}}\right) \quad (2.22)$$

with $a_{TF} = 0.8853 \cdot a_B Z^{-\frac{1}{3}}$ the screening distance where $a_B = 0.529 \text{ \AA}$, and $\alpha = (0.1, 0.55, 0.35)$ and $\beta = (6.0, 1.2, 0.3)$.

In the small-angle approximation, the single atom potential can be replaced with a continuous potential $U_{\text{pl}}(x)$, obtained averaging over two planar coordinates

$$U_{\text{pl}}(x) = Nd_p \int_{-\infty}^{+\infty} \int_{-\infty}^{+\infty} V(x, y, z) dy dz \quad (2.23)$$

with N the volume density of the atoms and d_p the inter-planar spacing.

Hence, the Moliere potential of a certain plane can be written as follows and results to be characterized by an exponential

$$U_{\text{pl}}(x) = 2\pi N d_p Z_i Z e^2 a_{\text{TF}} \sum_{i=1}^3 \frac{\alpha_i}{\beta_i} \exp\left(-\frac{\beta_i x}{a_{\text{TF}}}\right) \approx U_{\text{max}} \cdot \exp\left(-\frac{x}{a_{\text{TF}}}\right) . \quad (2.24)$$

Also thermal vibration should be taken into account, making Eq.(2.24) depend also on temperature (see [21] for the complete derivation), as shown in Figure 2.8.

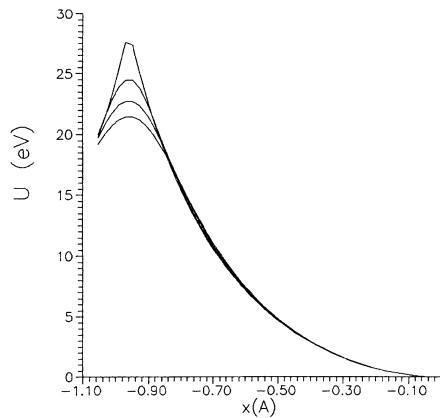


Figure 2.8: Plot of the Moliere potential of a single Si(110) plane at different temperatures. The curve at the top represents the potential of the static lattice. Downward looking, the curves at 77 K, 300 K and 500 K are shown. From Ref. [21].

Assuming that a particle moving in the lattice is influenced only by the nearest nearby planes, the potential experienced can be seen as the following sum

$$U(x) \approx U_{\text{pl}}\left(\frac{d_p}{2} - x\right) + U_{\text{pl}}\left(\frac{d_p}{2} + x\right) - 2U_{\text{pl}}\left(\frac{d_p}{2}\right) \approx U_{\text{max}} \cdot \left(\frac{2x}{d_p}\right)^2 . \quad (2.25)$$

This superposition of two plane potential can be approximated close to the minimum as harmonic $U(x) \sim x^2$ with good accuracy (Figure 2.9).

Under determined conditions described in the next Sections, a particle can be trapped in this potential well and forced to follow the direction of the crystal planes. Positive particles can penetrate deeper into the crystal because of repulsive interaction with nuclei, while negative particles turn out to collide much more often because of the attraction to regions with high densities of positive nuclei. In fact, in the case of negative particles, the interplanar potential shown in Figure 2.9 must be reversed in sign, thus becoming non-harmonic, with a minimum in the middle of the well. From now on only situations concerning positive particles will be treated. A summary schema of planar channeling for a positive particle is pictured in Figure 2.10.

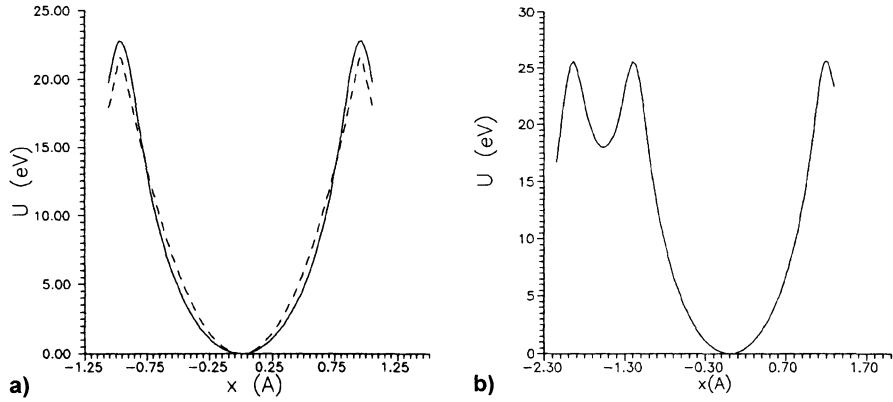


Figure 2.9: Plot of the interplanar Moliere potential for (a) the Si channels (110) and (b) the Si channels (111). In the Si(110) case, also the harmonic curve is represented with a dashed lines, which turns out to be an accurate approximation. From Ref [21].

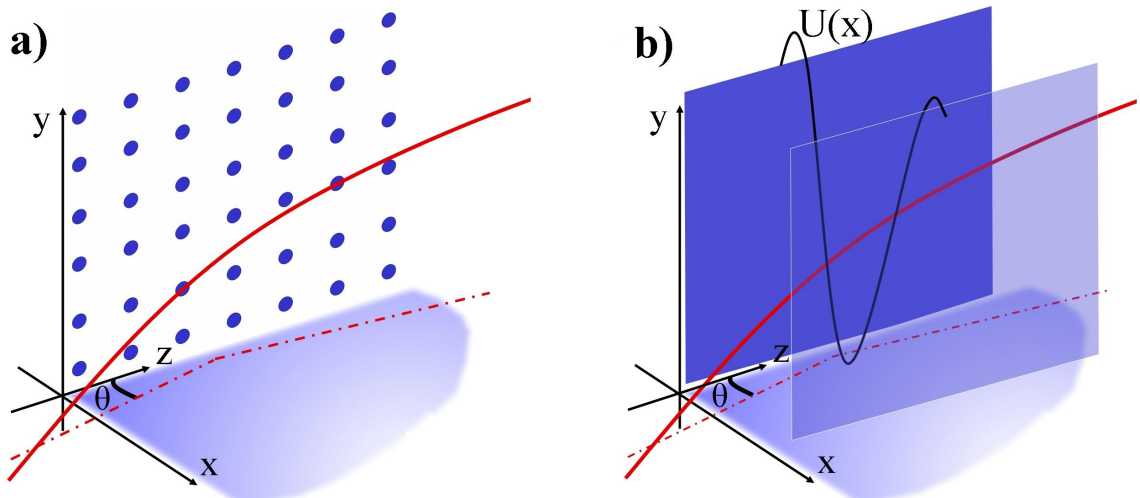


Figure 2.10: Visual representation of how a particle impacting the crystal with inciding angle θ can be trapped between the crystalline planes (a) by the potential well (b) generated between a pair of them. From Ref. [22].

The main parameters of silicon crystals with (110) orientation are reported in Table 2.2. The potential U and the electric field U' are evaluated at the critical position $x_{crit} = \frac{d_p}{2} - 2u_T$ with u_T the thermal vibration root-mean-square amplitude. The potential at the origin was set to zero $U(0) = 0$.

Properties of a Si(110) crystal	
Lattice constant of the unit cell	d_{cell} 5.43 Å
Interplanar distance	d_p 1.92 Å
Screening distance	a_{TF} 0.194 Å
Thermal vibration root-mean-square amplitude	u_T 0.075 Å
Interplanar potential at x_{crit}	$U(x_{crit})$ 16 eV
Interplanar electric field at x_{crit}	$U'(x_{crit})$ $5.7 \cdot 10^9$ eV/cm
Ionization potential	I 172 eV
Interaction length	X_0 9.37 cm

Table 2.2: List of the main properties of a silicon crystal with channeling plane defined by (110). From Ref. [21].

2.3.2 Channeling in Straight Crystals

Let us consider the motion of a particle with energy $E = \sqrt{p^2 c^2 + m^2 c^4}$ in a system where x and z are, respectively, the transverse and the longitudinal coordinate. In order to be trapped, an incoming particle must have transverse momentum p_x such that the particle cannot overcome the maximum of the transverse potential well. The impact angle with the crystal can be defined as

$$\theta = \tan \left(\frac{p_x}{p_z} \right) \approx \frac{p_x}{p_z} \quad (2.26)$$

if the transverse component is small with respect to the longitudinal one $p_x \ll p_z$.

The total energy E is conserved and it can be written in terms of a transverse and a longitudinal component, which must in turn be conserved separately since only transverse forces are acting. Assuming $E_z \approx E$ and $p_z \approx p$ the transverse energy can be written as

$$E_T = \frac{pv}{2} \theta^2 + U(x) = \text{const} \quad (2.27)$$

where $v = \frac{pc^2}{E}$ is the velocity of the particle.

The channeling condition results to be

$$\frac{pv}{2} \theta^2 + U(x) \leq U_{max} \quad (2.28)$$

from which an expression of the limiting angle of capture, called *Lindhard angle*, can be derived assuming $x = 0$

$$\theta_L = \sqrt{\frac{2U_{max}}{pv}} \quad . \quad (2.29)$$

A critical coordinate representing the maximum position at which a trapped particle can approach the atomic plane remaining in the channeling status can be defined as $x_{crit} \sim \frac{d_p}{2} - a_{TF}$. It can be viewed as a sort of channel border and it can also be written in terms of u_T , taking into account the thermal vibrations. The corresponding critical angle is

$$\theta_{crit} = \sqrt{\frac{2U(x_{crit})}{pv}} \quad . \quad (2.30)$$

It is important to note that this limit depends on the incoming particle momentum. Given the harmonic approximation in Eq.(2.25) one can derive the equation of motion and find that the trajectory of a channeled particle is sinusoidal with period $\lambda = \pi d_p \sqrt{\frac{pv}{2U_{max}}}$.

If the particles in a beam impacting a crystal are assumed to be distributed uniformly in $(-d_p/2, -d_p/2)$ with incident angles uniformly distributed in $(-\theta_{crit}, \theta_{crit})$, the probability of each particle to be captured is called *straight crystal acceptance* and can be written as

$$A_s = \frac{2x_{crit}}{d_p} \frac{\pi}{4} \frac{\theta_{crit}}{\varphi} \quad (2.31)$$

with φ the beam divergence. This expression is valid restricting to the case of harmonic interplanar potential.

2.3.3 Channeling in Bent Crystal

Let us consider a crystal bent in the xz plane with constant bending radius R and corresponding curvature $1/R$. In the non-inertial frame related to the lattice, a channeled particle results to be affected by a centrifugal force pv/R and its motion is still sinusoidal with the same period, but around a new equilibrium point. This effect can be taken into account considering an effective interplanar potential equal to

$$U_{eff}(x) = U(x) + \frac{pv}{R}x \quad (2.32)$$

and the transverse energy of a particle in the crystal becomes

$$E_T = \frac{pv}{2}\theta^2 + U_{eff}(x) \quad . \quad (2.33)$$

Thus, the presence in Eq.(2.32) of a new term proportional to pv/R modifies the shape of the potential as shown in Figure 2.11: the bigger the pv/R term is, the smaller becomes the potential well depth. The position of the minimum is also shifted. Increasing pv/R more and more, if the particle momentum or the crystal curvature are too big, it could be reached a condition in which the well disappears and the channelling phenomenon is not possible anymore. A critical radius can be defined by imposing the centrifugal force to be equal to the maximum interplanar field:

$$R_{crit} = \frac{pv}{U'(x_{crit})} \quad . \quad (2.34)$$

In these conditions, the critical angle results to be reduced by a factor depending on the critical radius and the crystal curvature

$$\theta_{crit}(R_{crit}/R) = \theta_{crit,0} \left(1 - \frac{R_{crit}}{R}\right) \quad . \quad (2.35)$$

In the small-angle approximation, given a crystal of length $L \ll R$ a channeled particle results to be deflected by an angle θ_C equal to the crystal bending

$$\theta_C = \frac{L}{R} \quad . \quad (2.36)$$

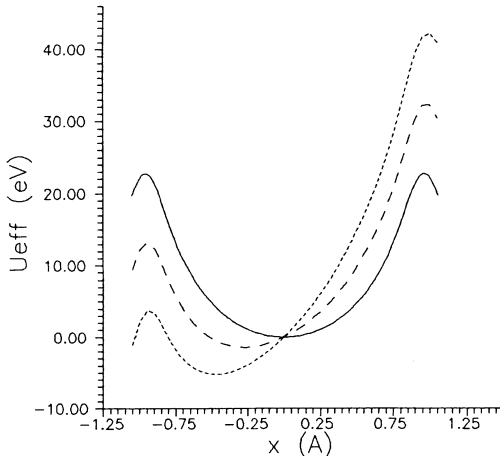


Figure 2.11: Plot of the interplanar Moliere potential for Si(110) (solid line) and of the effective potential U_{eff} for pv/R of 1 GeV/cm (dashed line) and 2 GeV/cm (dotted line). Increasing pv/R more and more, it could be reached a condition in which the well disappears and the channelling phenomenon is not possible anymore. From Ref [21].

2.3.4 Dechanneling

Although the space between crystalline planes is characterized by a reduced electronic density, a channeled particle can scatter with electrons and nuclei. The transverse energy is affected in these type of processes and the particle's E_T may become greater than the potential well depth, thus disrupting the channeling condition. This process is called *dechanneling* and it can be modelled using the formalism of diffusion theory.

Given a beam traversing the crystal longitudinally, the dechanneling process acts by decreasing the initial population N_0 of channeled particles with an exponential law that depends on the longitudinal coordinate z :

$$N(z) = N_0 \exp\left(-\frac{z}{L_D}\right) \quad (2.37)$$

where L_D is called *dechanneling length*. Using large boost approximation $\gamma \gg 1$, an explicit expression of L_D can be derived by applying diffusion theory [21]:

$$L_D = \frac{256}{9\pi^2} \frac{pv}{\ln(2m_e c^2 \gamma / I) - 1} \frac{a_{\text{TF}} d_p}{Z_i r_e m_e c^2} \quad (2.38)$$

with I the ionization potential of the material from which the crystal is made, $r_e = 2.818 \cdot 10^{-15}$ m the classical radius and $m_e = 0.511$ MeV the rest mass of the electron.

In a bent crystal, the lattice curvature influences the scattering processes, modifying the particle distribution in the channel, the diffusion factor and the critical transverse energy. Under the assumption of harmonic potential the dechanneling length can be written, in this case, as

$$L_D(pv, R) = L_{D,0} \left(1 - \frac{R_{\text{crit}}}{R}\right)^2 \quad (2.39)$$

where $L_{D,0}$ is the expression for a straight crystal described in Eq.(2.38).

It can be derived that the trapping acceptance, defined in Eq.(2.31) for a straight crystal and dependent mainly on the beam divergence and on the crystal bending angle θ_C , assumes a similar form:

$$A_S(pv, R) = A_{S,0} \left(1 - \frac{R_{\text{crit}}}{R}\right)^2 . \quad (2.40)$$

A rough estimation of the crystal efficiency F can be derived combining the trapping acceptance with the exponential decaying expression of dechanneling in Eq.(2.37). This represents the fraction of incoming particles that are effectively deflected by the crystal at the angle θ_C . Assuming harmonic approximation and L_D of Eq.(2.39), F can be written as

$$F(\Theta, \rho) = A_S \cdot (1 - \rho)^2 \exp\left(-\frac{\Theta}{\Theta_D \rho (1 - \rho)^2}\right) \quad (2.41)$$

where $\rho = \frac{R_{crit}}{R}$ and the constant Θ_D represents the ratio between the dechanneling length and the critical radius

$$\Theta_D = \frac{256}{9\pi} \frac{NZa_{TF}d_p^2}{\ln(2m_e c^2 \gamma / I) - 1} \quad . \quad (2.42)$$

It is worth noting that the efficiency of the process is primarily determined by the crystal properties, such as θ_C and R , but also depends on the energy of the incoming particles. The dependence on the particle momentum and velocity is, in fact, incorporated into the definition of R_{crit} . Furthermore, given a certain bending angle θ_C , the optimal value of the curvature pv/R can be obtained by maximizing the expression of F (Figure 2.12).

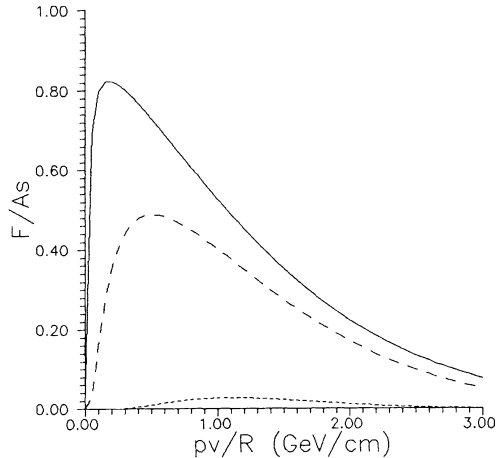


Figure 2.12: Plot of the efficiency F/A_s of deflection at angles 1 mrad (solid line), 10 mrad (dashed), and 100 mrad (dotted) by a Si(110) channel. From Ref. [21].

For a crystal made of Silicon Si(110) the constant Θ_D results to be:

$$\Theta_D = \frac{4.526}{\ln(5907.51 \cdot \frac{E}{m}) - 1} \quad . \quad (2.43)$$

2.3.5 Other crystal processes: Volume Capture and Volume Reflection

The process known as *volume capture* is an incoherent phenomenon that is, in a way, the opposite of dechanneling. It occurs when a non-channeled particle undergoes an interaction that reduces its total transverse energy to below the maximum of the potential well, causing it to become trapped within the crystal lattice. Moreover, in a bent crystal, trajectories of particles from different incident angles can become tangential to the curved crystallographic planes at some point within the crystal: a transition to the channeled state can happen more likely, provided that the necessary energy conditions are met. After trapping, these particles are considered as the standard channeled ones, so they can possibly undergo dechanneling.

Particles that are not channeled but are still affected by the crystal field are known as *quasi-channeled* particles. When particles enter the crystal with an incident angle greater than the critical angle but smaller than the bending angle ($\theta_{crit} < \theta < \theta_C$), they can undergo a coherent process called *volume reflection*. In this process, the particles are deflected in the opposite direction to that of the crystal bending (and therefore of the channeled beam) at angles of about $-\theta_{crit}$ due to the interaction with the averaged potential of the crystalline planes. In particular, it has been measured that 400 GeV protons in crystals with $R \gg R_{crit}$ have an average deflection of $\theta_{ref} \sim 1.6 \cdot \theta_{crit}$ [23]. The reflection process is expected to be very efficient, with a probability of reflection greater than 90% for particles within the suitable angular range. However, the nuclear interaction rate of a reflected particle is much higher than for a channeled particle.

A schematic representation of all the crystal processes described above is reported in Figure 2.13, from the potential and from the crystal perspective, underlying the differences between the straight and bent case. Figure 2.14 shows pictorially how these processes influence the deflection angular distribution of particles when detected after the crystal. To give an idea of how these processes manifest, Figure 2.15 shows the results of a simulation performed with a Geant4 (described later in Sections 3.1.2 and 3.1.4) involving 10 million protons at 400 GeV energy that are directed at a silicon crystal of length $L_C = 1.94$ mm and bending angle $\theta_C = 50.5 \mu\text{rad}$. The histogram, which displays the 2-dimensional distribution of incoming angle versus deflection angle, can be divided into six regions corresponding to the possible crystal phenomena. Regions (1) and (6) represent amorphous scattering by multi-Coulomb interaction, while region (3) signifies the dechanneling mode and connects the channeling (2) and volume reflection peak (4). The sparse profile of region (5) corresponds to volume capture. With more statistical data, the profiles of both regions (3) and (5) would be more pronounced [24].

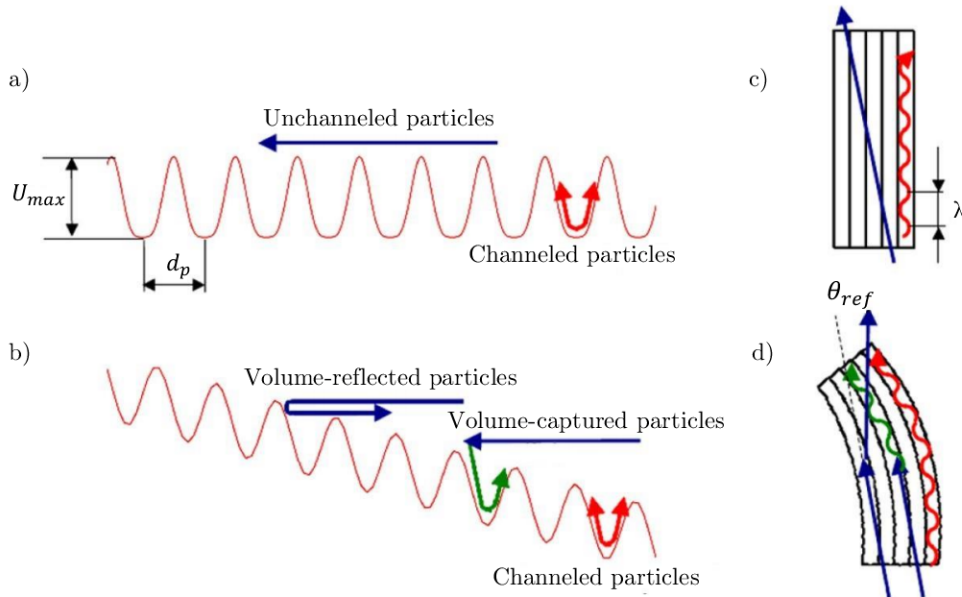


Figure 2.13: (a) Plot of the periodic planar potential in a straight crystal for positively charged particles. A channeled particle has an oscillatory motion in the potential well (red arrow), while a particle results to be unchanneled if its transverse energy is greater than the depth of the potential well U_{max} (blue arrow). (c) Sketch the particle trajectories in a straight crystal. (b) Plot of the periodic planar potential in a bent crystal for positively charged particles. The blue arrow represents volume-reflected particles, while the green one represents the volume-capture case. (d) Sketch of the particle trajectories in a bent crystal. From Ref. [25].

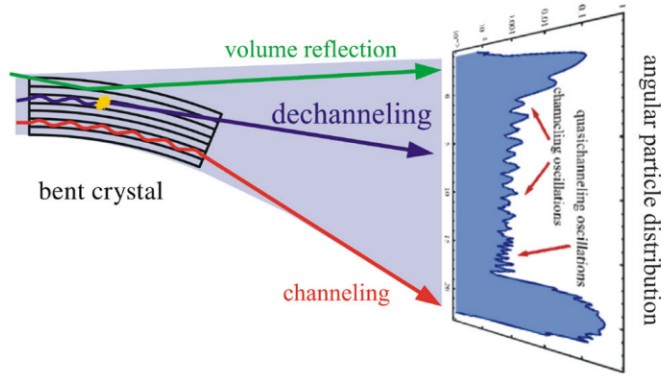


Figure 2.14: Sketch of the angular particle distribution of particles passed through a bent crystal. Usually, if the crystal is well oriented with respect to the incoming beam, a peak due to channeled particles can be spotted on one side and another peak due to volume reflected particles is observed on the opposite side. From Ref. [26].

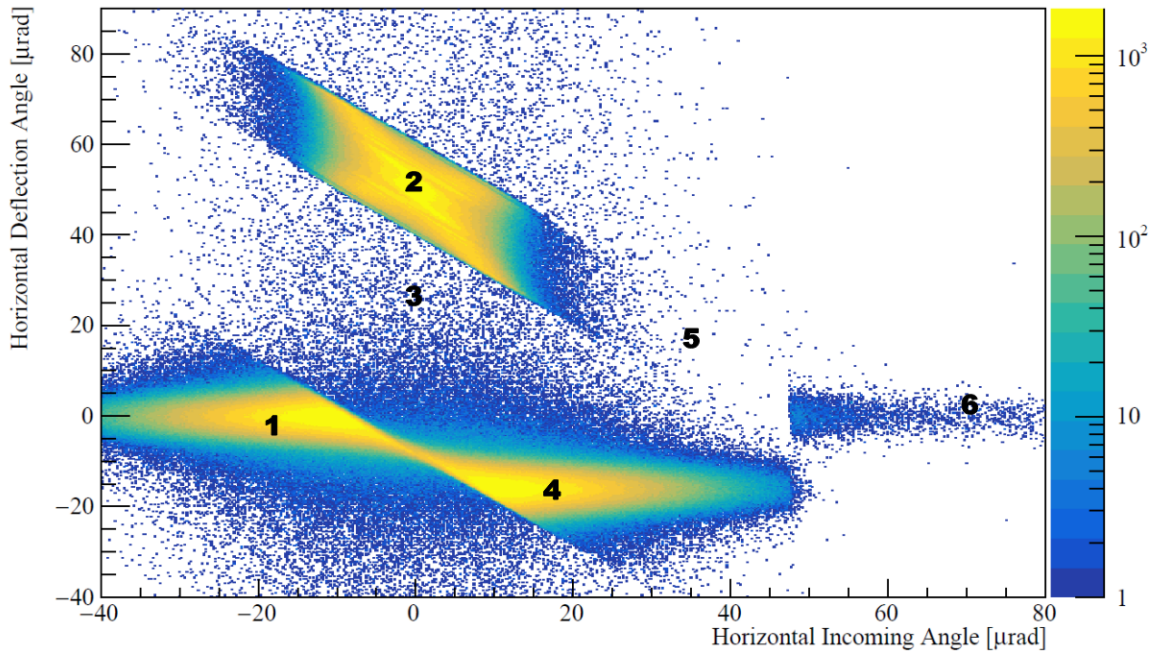


Figure 2.15: Two-dimensional histogram plot of deflection angle against incoming angle, obtained from a Geant4 simulation of 10 million protons of energy 400 GeV. The beam impacts a silicon crystal of length $L_C = 1.94$ mm and a bending angle of $\theta_C = 50.5\mu\text{rad}$. The y-axis is normalised relative to the incident angle of proton with respect to the crystal plane. (1) and (6) amorphous scattering region; (3) dechanneling region; (2) channeling region; (4) volume reflection region; (5) volume capture region.

2.4 Layout of the Experiment and of the Proof of Principle

Crystal channeling processes can have many applications in high energy physics, first and foremost in the context of beam collimation where bent crystals can replace primary collimators to efficiently direct all halo particles of an accelerator beam onto a single absorber, providing effective cleaning. Furthermore, bent crystals can also be used as beam extractors from accelerator rings for fixed-target experiments or can be used to perform physics measurement, such as the determination electromagnetic moments, as motivated in Section 2.2.1 and proved by the E761 Collaboration which, in 1992, measured the magnetic moment precession of Σ^+ with this technique using a 800 GeV/c proton beam at Fermilab [27].

The idea proposed for measuring the electromagnetic moments of Λ_c^+ consists in a fixed-target experiment directly performed within the primary vacuum of the LHC, avoiding the necessity of a dedicated extraction line. The experimental setup employs a *double-crystal* arrangement that exploits entirely the channeling properties of crystals. A first bent crystal (CRY1 or Target Collimator Crystal Splitting TCCS) is used as kicker to deflect protons from the secondary or tertiary halo of the main LHC beam onto a target made of amorphous tungsten, where charmed baryons can be produced. A second bent crystal (CRY2 or Target Collimator Crystal Precession TCCP), placed immediately after the target, is used to induce spin precession to channeled particles. In order to prompt a measurable precession, CRY2 is required to be much longer with respect to crystals usually employed in collimation. A detector is needed to reconstruct the Λ_c^+ decay products and absorbers are positioned downstream to halt the deflected proton beam and background particles that arise due to interactions with the target and crystal materials. The overall layout is outlined in Figure 2.16

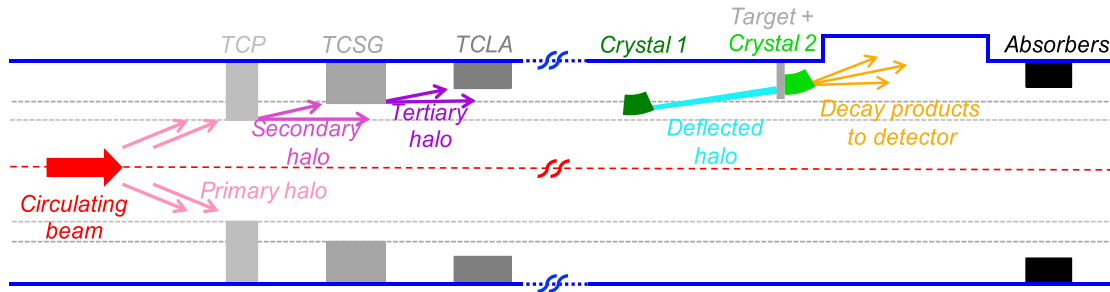


Figure 2.16: Schema of the experimental setup for Λ_c^+ electromagnetic measurement and its integration with the LHC collimation system, which general aim is to minimize the amount of beam loss and subsequent deposited energy in the superconducting magnets. The present system is composed by movable ring collimators organized in a three-stage cleaning hierarchy: TCP are the primary collimators, TCSG are the secondary collimators and TCLA are the absorbers. From Ref. [28]

The double-channeling concept has already been tested by the UA9 Collaboration [29] using a layout similar to the one proposed above (CRY1, target, CRY2). This experiment was conducted at the Super Proton Synchrotron (SPS) with a proton beam of energy 270 GeV. To produce Λ_c^+ with sufficient high rate to perform MDM and EDM measurements, a beam energy of the order of TeV is required, which is only available at the LHC. The channeling phenomenon of 6.5 TeV/c proton beams in single crystal has been already observed at LHC in the context of crystal collimation [30]. However, no experiment involving a double crystal setup has been performed there before, and this represent one of the most significant challenges.

The optimal location for inserting a double-crystal experimental setup along LHC has been studied in detail [28]. Initially, the Interaction Point 8 (IP8) was considered, due to the presence of the LHCb detector. This single-arm spectrometer is developed with an asymmetric design in the forward region, making it particularly suitable for forward physics and, therefore, also for fixed-target experiments. The original idea was to place the tungsten target in front of LHCb and exploit the optimal efficiency of its subdetectors to reconstruct Λ_c^+ decay products. However, the high risk involved, the unknown performance of both the proton on target (PoT) rate and crystal efficiency at TeV energies, the complex integration issues in front of the VELO, and overloaded resources at IP8 due to the installation

of Upgrade 2 of LHCb, proved to be serious complications. Furthermore, given the particular characteristics of this LHC region, it turned out that important constraints have to be imposed on the PoT rate in order to maintain the losses on superconducting magnets below the safety limits: an additional collimation system may need to be constructed to mitigate these effects.

On the other hand, Insertion Region 3 (IR3) results to be a more feasible location to carry out the experiment. IR3 is a beam halo collimation point specialized in momentum cleaning with the aim to remove particles with large energy offset. Installing the setup in IR3 can take advantage of existing vertical absorbers to intercept the split halo after passing through a dedicated detector, which, in this case, needs to be designed and constructed for this purpose. In this situation, CRY1 should intercept the secondary halo originating at the TCP placed at IR7, which is another collimation region located at the opposite side of LHC. The low loss pattern expected around the LHC ring in this scenario allows for measurements to be taken during standard physics operations without imposing constraints on the maximum stored intensity, in the so called *parasitic* operational mode. The detector of the IR3 final experiment is currently under study. A minimal setup able to reconstruct Λ_c^+ decay products can consist into four tracking stations upstream and four tracking stations downstream a magnet, as sketched in Figure 2.17.

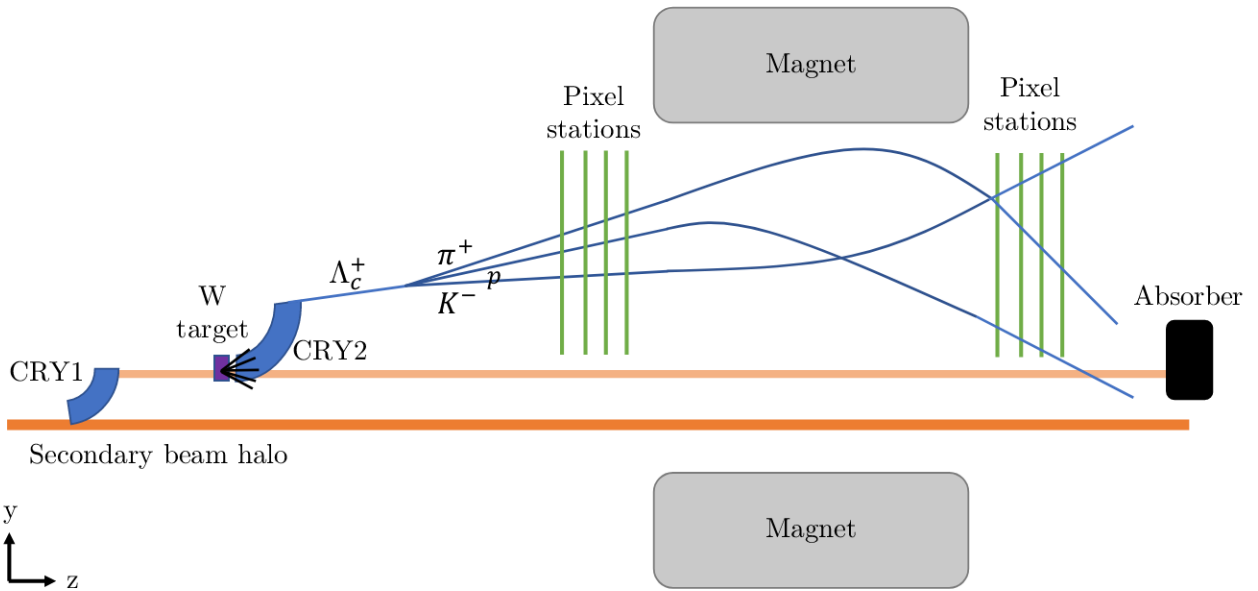


Figure 2.17: Diagram (not in scale) of the setup proposed for the Λ_c^+ electromagnetic moment measurement experiment at IR3. A simple detector, able to reconstruct the baryon's decay products, could be composed by four upstream tracking stations, a magnet and other four downstream tracking stations.

An interesting additional feature of IR3 is that the two circulating beams are separated into two different pipes, since it is not a collision point. Beam 1 is being considered to conduct the experiments but one can think of designing a mirror experiment by exploiting Beam 2 as well.

A mathematical description of the setup, showing the dependence on all the parameters that can be optimized when designing the layout and the operational settings, can be given as follows [14, 15, 28].

Given a beam circulating with intensity $I(t)$ and characterized by a lifetime τ (expected to be ~ 200 h comparing to the usual operational values of 2018), the rate of protons deviated by CRY1 that hit the target is, then, estimated with the proton on target function as

$$PoT(t) = \frac{1}{2} \frac{I(t)}{\tau} \exp\left(-\frac{t}{\tau}\right) N_{\text{hit}}^{\text{CRY1}} \varepsilon_{\text{chann}}^{\text{CRY1}} \quad (2.44)$$

where $\frac{I(t)}{\tau} \exp(-\frac{t}{\tau})$ is the total beam loss rate, the factor $\frac{1}{2}$ is introduced to take into account the sharing of the total loss rate between the horizontal and vertical planes, $N_{\text{hit}}^{\text{CRY1}}$ is the fraction of protons that hit the CRY1, and $\varepsilon_{\text{chann}}^{\text{CRY1}}$ the channeling efficiency of CRY1, i.e. fraction of impacting protons trapped between crystalline planes for the entire path in the crystal. As explained in Section 2.3.4, the channeling efficiency depends on the angular acceptance and on the dechanneling phenomenon and can be expressed as function of the incoming particle's energy and of the crystal parameters as expressed by Eq.(2.41).

The number of Λ_c^+ particles produced from the interaction of channeled protons with a tungsten target in the time Δt can be calculated as follows:

$$N_{\Lambda_c^+} = \int_{\Delta t} PoT(t)dt \cdot \sigma(pp \rightarrow \Lambda_c^+ X) N_T . \quad (2.45)$$

Here, $\int_{\Delta t} PoT(t)dt$ represents the integrated proton rate over a certain data-taking time interval (the usual fill length during LHC operations is of the order of ~ 10 h), N_T is the number of target nucleons and $\sigma(pp \rightarrow \Lambda_c^+ X)$ is the cross-section for producing Λ_c^+ particles in proton-proton interactions. The areal target thickness is $N_T = N_A \rho_T L_T / A_T$, where N_A is the Avogadro number, ρ_T is the target density, L_T is the target length along the beam, and A_T denote the atomic mass. In designing the implementation of the final experiment for dipole moments physics, the goal is to acquire data for at least a total number of 10^{15} protons on target.

The number of Λ_c^+ baryons channeled in CRY2 and reconstructed by the detector can be estimated as

$$N_{\Lambda_c^+}^{\text{reco}} = N_{\Lambda_c^+} \mathcal{B}(\Lambda_c^+ \rightarrow f) \cdot \varepsilon_{\text{chann}}^{\text{CRY2}} \cdot \varepsilon_{\text{DF}} \cdot \varepsilon_{\text{det}} \quad (2.46)$$

where $\mathcal{B}(\Lambda_c^+ \rightarrow f)$ is the branching fraction of the Λ_c^+ decay into the particular final state f that is chosen and $\varepsilon_{\text{chann}}^{\text{CRY2}}$ is the channeling efficiency of CRY2. The detector reconstruction efficiency ε_{det} for the $\Lambda_c^+ \rightarrow f$ decay can be estimated as the product of geometrical, trigger, and tracking efficiencies, $\varepsilon_{\text{det}} = \varepsilon_{\text{geo}} \cdot \varepsilon_{\text{trigger}} \cdot \varepsilon_{\text{track}}$, with the latter including combinatorics and selection efficiencies. The decay flight efficiency ε_{DF} is composed by a term representing the survival efficiency, ε_s , which accounts for the fraction of channeled baryons decaying after the target and the crystal (hence, after a total length of $L = L_T + L_C$), and the probability ε_l for baryons to decay within the detector acceptance. The former can be estimated taking into account the mean life time of Λ_c^+ (reported in Section 2.1.3):

$$\varepsilon_s = \frac{1}{L} \int_0^L \exp\left(-\frac{l}{c\gamma\tau_{\Lambda_c^+}}\right) dl . \quad (2.47)$$

Once all the parameters are set and optimized, sensitivity on measurements can be estimated through statistical uncertainties on the electric factor d and on the gyromagnetic factor g :

$$\begin{aligned} \sigma_d &\approx \frac{g - 2}{\alpha s_0 (\cos \Phi - 1)} \frac{1}{\sqrt{N_{\Lambda_c^+}^{\text{reco}}}} \\ \sigma_g &\approx \frac{2}{\alpha s_0 \gamma \theta_C} \frac{1}{\sqrt{N_{\Lambda_c^+}^{\text{reco}}}} . \end{aligned} \quad (2.48)$$

The precision expected in two years of data-taking is $7 \cdot 10^{-17}$ e cm for the EDM and $0.02 \cdot \mu_N$ for the MDM [18].

2.4.1 Proof of Principle

As pictured in Figure 2.17, in order to reconstruct Λ_c^+ decay products, a new spectrometer must be designed, constructed and installed. This setup requires the presence of a magnet with a field integral comparable to that of the LHCb spectrometer (~ 4 Tm). Its installation is not possible during Run 3 of LHC, so the final setup will be placed during Long Shutdown 3 (LS3), planned for 2026-2028, and the actual experiment will be conducted during Run 4. However, a *proof of principles* (PoP) can be carried out before LS3 with the idea of demonstrating the feasibility and exploring the LHC operations that will be required during the real experiment [31].

The main goals of the PoP are, firstly, to measure the channeling performance of CRY2 at energies in the TeV range, since it has never been done before for such a long crystal. In fact, currently its efficiency can only be estimated through simulations which inevitably introduces some uncertainties. Secondly, the test aims to gain experience and improve operational techniques for crystal alignment, optimization of the PoT rate and control of the secondary halo. Finally, the PoP aims to estimate the background environment, which is important for the new IR3 detector studies. This can be accomplished by making use of a simple detecting setup composed only by tracking planes. If possible, even the first precession measurements can be performed with the idea of using as spectrometer the existing beam orbit corrector dipole MCBWV.4R3.B1, a vertical warm magnet with a maximum field integral 1.87 Tm. CRY2 has to be placed approximately 1 m before the magnet.

For machine protection reasons, during the proof of principle, all tests have to be carried out at low proton intensity of about $I_{\text{tot}} \sim 3 \cdot 10^{11}$ protons, allowing the use of existing vertical collimator TCLA.A5R3.B1 downstream of CRY2 to safely absorb the deflected halo. In the final experiment, instead, the stored intensity is expected to be $I_{\text{tot}} > 3 \cdot 10^{14}$ protons and, in order to produce the interesting physics, the flux towards CRY2 should be at least 10^6 PoT/s. In this case, the possibility to add additional collimators in the available space in IR3 after the second crystal must be studied.

Since the experimental setup implies a challenging combination of high precision devices, the idea for the proof of principles is to proceed by steps [32]:

- (i) Firstly, both crystals have to be inserted in the main beam primary halo, with low intensity, to establish references for the alignment procedure and to measure the channeling efficiency. The concepts of alignment and efficiency are much connected: if the crystal is badly oriented with respect to the beam, channeling is not possible since the incident angle can fall out of the acceptance range, making the crystal behave as an amorphous silicon block. Hence, angular scan analysis are crucial in order to find the ideal orientation that corresponds to the maximal channeling efficiency. This implies also that the crystals have to be placed on rotatable goniometers with angular tunability of the order of μrad .
- (ii) The second step consists in establishing double channelling without the target and using protons of 1 TeV to measure channelling efficiency of CRY2 through the use of one (or more) tracking station(s). CRY1 has to be introduced into the primary halo, kept to low intensity. This scenario is sketched in Figure 2.18.
- (iii) In the third step, the tungsten target is introduced with the aim of observing charged particle rates on the detector plane and, if possible at all, channeling of the produced particles. CRY1 is still introduced into the primary halo.

The installation of the PoP setup is currently scheduled at the end of 2024, with tests planned for 2025, at the end of Run 3. Prior to installation, all design elements must be refined and validated through simulations and test beam runs. During LST3, all necessary upgrades will be carried out, and additional components of the final experiment layout will be transferred. When designing PoP elements, it's important to keep in mind that as much as possible should be retained for the final experiment. Therefore, the largest possible number of parts should be constructed to be compatible with the requests of the high-luminosity runs that will be carried out during Run 4 (HL-LHC). Regarding the tracking stations, LHCb's VeloPixel module was found to be the most suitable device

among those currently existing to meet the requirements of the experimental settings.

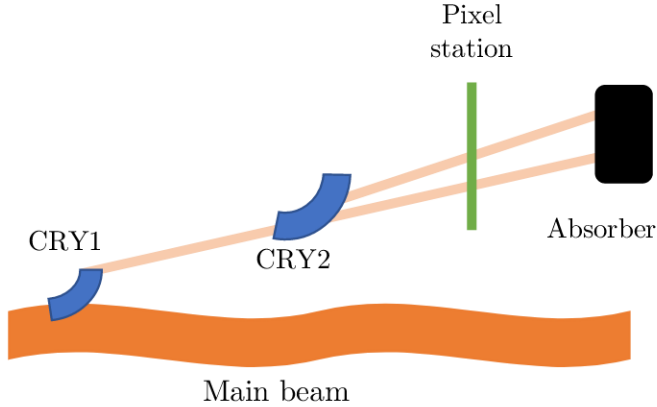


Figure 2.18: Diagram of the experimental setup of the (ii) step of the proof of principles. The splitting crystal CRY1 is inserted directly into the main beam in order to redirect protons to the precession crystal CRY2. Depending on CRY2 channelling efficiency, a certain fraction of these protons can be deflected again. The two peaks can be detected with a pixel station. The already existing TCLA absorber can be used.

2.4.2 Crystals and Target

Even if during the proof-of-principle stage the tests will be carried out at safe intensities, ideally the splitting and the precession crystals should be designed to be compatible with the ultimate proton beam intensities planned at the HL-LHC. CRY1 should be capable of intercepting the multi-turn betatron halo, and both crystals should be designed to allow also direct exposure to the primary halo of the low intensity circulating beam. This is necessary for evaluating the channelling performances of particles at the high energies accessible only at LHC. The setup should be operational at 7 TeV energy, which is the most challenging condition, as well as at all intermediate energies starting from the injection one of 450 GeV.

Table 2.3 presents the functional specifications of the first crystal (TCCS), the tungsten target, and the second crystal (TCCP), which meet all the requirements listed above. CRY1 shares similar characteristics with the crystal used in IR7 for ion beam collimation. For CRY2, the curvature radius was selected to prevent channelling of secondary protons at top energy, which could interfere with the measurement of Λ_c^+ decay products. However, double channelling of proton halos remains possible at injection energy.

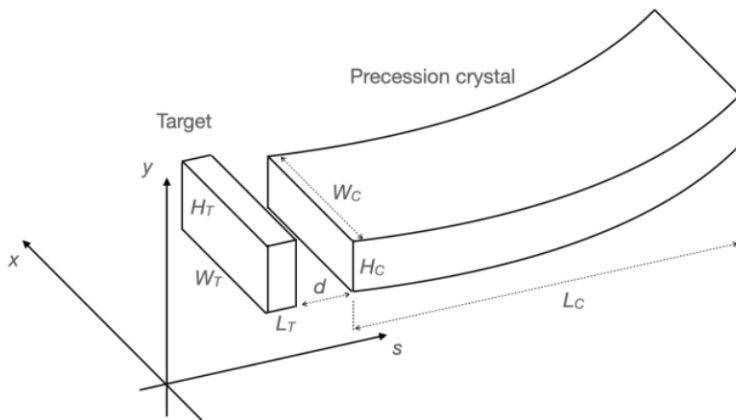


Figure 2.19: Schematic representation of the tungsten target and the precession crystal CRY2, aligned with the beam direction s . The numerical value of their relevant physical quantities are reported in Table 2.3. The distance d between the two elements should be kept to the minimum. From Ref. [32].

Property	TCCS Specification	
Material	Si	
Channeling plane	(110)	
Crystal length along the beam	L_c	4.0 ± 0.4 mm
Bending angle	θ_c	$50.0 \pm 2.5\mu\text{rad}$

Property	Target Specification	
Material	W	
Density	ρ_T	19.25 g/cm^3
Target length along the beam	L_T	5.0 ± 0.1 mm
Minimal thickness in bending (vertical) direction	H_T	4.0 ± 0.1 mm
Minimal width in horizontal direction	W_T	8.0 ± 0.1 mm

Property	TCCP Specification	
Material	Si	
Channeling plane	(110)	
Crystal length along the beam	L_C	70.0 ± 0.5 mm
Minimal thickness in bending (vertical) direction	H_C	4.0 ± 0.1 mm
Minimal width in horizontal direction	W_C	8.0 ± 0.1 mm
Nominal bending angle	θ_C	7.0 mrad
Nominal bending radius	$R_{C,nom}$	10 m

Table 2.3: List of the specifications of the Target Crystal Collimator Crystal Splitting (also known as CRY1), the tungsten target and the Target Collimator Crystal Precession (also known as CRY2). From Ref. [32].

Both crystals must be movable in the vertical direction, so that they can be safely retired to a parking position when not in use, allowing the beam to circulate freely. The assembly should include a goniometer for angular scans. For CRY1, high-precision goniometers based on interferometry, like those used in IR7, can be utilized. For CRY2, which intercepts a broad distribution of particles produced in the target, conventional mechanical goniometers will suffice. However, for the proof-of-principle setup, also the second crystal has to be tested with primary proton beams, therefore, an angular precision similar to that of CRY1 is necessary.

2.4.3 LHCb VELO Pixel Detector

The LHCb VELO [33] is the vertex locator of the LHCb experiment, placed close to the beam. It is a hybrid pixel detector and it was installed in May 2022, just before the start of Run 3. This new version replaces the previous one and was specifically designed to meet the challenges posed by the general upgrade of the LHCb experiment for Run 3. This upgrade consists, firstly in a significant increase in luminosity of a factor of 5 compared to Run 2, which corresponds to a value of $L = 2 \cdot 10^{33} \text{ cm}^{-2}\text{s}^{-1}$ and to a number of interactions per crossing equal to $\nu = 7.6$. Secondly, the LHCb hardware trigger has been removed, which means that every subdetector has to read-out at a rate of 40 MHz, corresponding to the nominal LHC bunch frequency.

The VELO's main function is to detect vertices with high precision, including the interaction and secondary vertices, specifically the decay vertices of hadrons containing b and c quarks; this is essential since the LHCb detector specializes in studying beauty and charm physics. This task requires the resolution on the impact parameter to be high. Since the detector must operate in high luminosity conditions, issues can arise due to irradiation: the maximum integrated flux that the detector must withstand is approximately $\sim 8 \cdot 10^{15} n_{\text{eq}}/\text{cm}^2$, and it can experience leakage currents of $\sim 200\mu\text{A}/\text{cm}^2$ at 20°C with a bias voltage of 1000 V at the pixel placed closest to the beam. Therefore, on the one hand the silicon must be protected from thermal runaway by proper cooling, trying, on the other hand, not to add too much material. In addition, the electronics must be sufficiently radiation-hard to cope with this. In addition, Run 3's high luminosity and operational frequency have data-rate implications. At the highest luminosity, the number of hits per event is expected to be approximately $\sim 5.2 \text{ cm}^{-2} \cdot R^{-1.9}$, where R is the distance from the beam. An output rate of 15.1 Gbit/s is required to the ASICs, indicating the need to design fast and efficient electronic circuits.

The upgraded VELO fulfils all the requirements listed above. The detector is made of 52 L-shaped silicon modules arranged in two retractable halves. It is a hybrid pixel detector, which means that the detecting element (a silicon pixel sensor) and the readout chip (a pixel ASIC, called VeloPix) are two physically distinct objects that are placed one above the other. A module contains 4 *tiles*, each being made of three VeloPix ASICs bump-bonded to one rectangular Si sensor. The key element of the module is a microchannel cooling substrate to which the tiles are glued, as well as two readout printed circuits and one control printed circuit. A pair of modules, one from the left and one from the right side, compose a *station*, which can be in an open position during beam injection, or in a closed position during LHC stable beam operation, as reported in Figure 2.20. The whole detector is enclosed into an aluminum RF foil box to separate the detector's secondary vacuum from the machine vacuum.

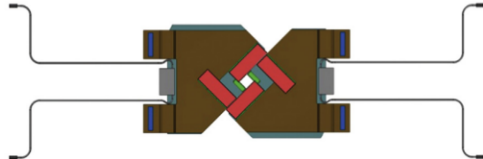


Figure 2.20: Schema of a VELO station in the closed configuration. The main beam passes through the small squared hole left between the right and left modules. The innermost pixel is expected to be at a distance $x, y = 5.1$ mm from the beam. From Ref. [34].

A picture of a module is shown in Figure 2.21. It is composed by 4 silicon sensors (two per side) of $200\ \mu\text{m}$ thickness and $42.46 \times 14.08\ \text{mm}^2$ active area and 12 VeloPix ASICs (three per sensor) of $200\ \mu\text{m}$ thickness and dimensions $14.08 \times 14.08\ \text{mm}^2$, both arranged in a L-shape. The silicon sensor exploit the CMOS technology and are characterized by a n-side readout, which means the electrons are collected. The minimum threshold to generate a signal is the collection of $500e^-$, that corresponds to a deposited energy threshold of 1.8 keV. Noise occupancy is estimated to be low, of the order of $\leq 10^{-5}$. The hybrids are made of copper and kapton and include a GBTx chip. Everything is glued on a microchannels silicon substrate of $200\ \mu\text{m}$ thickness to cool the ASICs and the sensors. As explained later, the cooling system is designed in order to be so efficient that the most inner tiles protrude by 5 mm the substrate, reducing a lot the material budget in the region near the primary collision point.

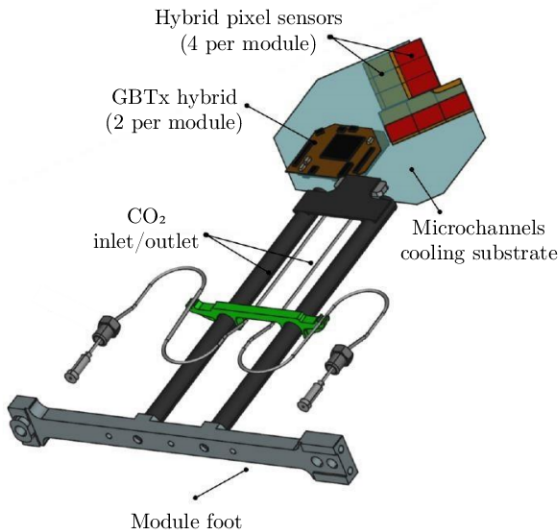


Figure 2.21: Graphical representation of a VELO module, including the cooling system and the mechanical support. From Ref. [34].

The VeloPix ASICs consists into a matrix of 256×256 pixels of $55 \times 55\ \mu\text{m}^2$ pitch with binary readout. No time information are, therefore, recorded. It is designed in order to collect data at each bunch crossing at 40 MHz, which corresponds to a time stamp resolution of 25 ns. The mean number of

tracks per module per event is estimated to be 32.8, which corresponds to ~ 600 Mhits/s, and the mean output rate per ASICS is expected to be 10.2 Gbit/s, averaged over the total active area. Since pixel size is small and the incoming particles have non zero angle, it is estimated that the 55% of tracks will yield a cluster with size greater than 1 pixel. Therefore, the idea is to gather groups of 2×4 pixels into the so called *Super Pixel*: multiple hits are included in the same packet of information and transmitted together, resulting in a reduction in bandwidth of 30%. The data-gathering happens column wise in End of Column logic and, at the end, information is sent away through 4 high speed output serializers, called *Gigabit Wireline Transmitter* (GWT), characterized by a bandwidth of 4.8 Gbit/s. A schema of the electronic architecture is shown in Figure 2.22.

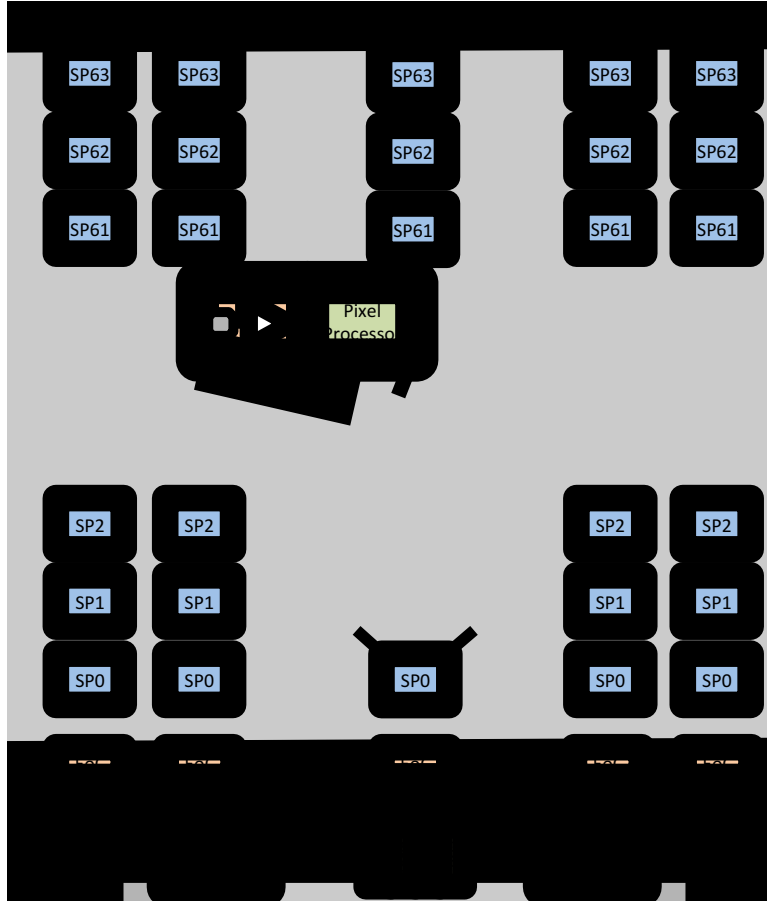


Figure 2.22: Diagram of the VeloPix chip architecture. As it can be observed in the middle, groups of 8 pixels are combined in Super Pixels, which are the basic readout units. Grey arrows represent the flow of data, which is always directed in the opposite direction with respect to the beam region. The four serializers are shown in green. From Ref. [33].

The cooling system [35] is designed in order to cool down the VeloPix ASICs, the sensors and the GBTx hybrids for a total VELO power budget 1.56 kW. The main requirement consists in keeping an operational temperature of $T = -20^\circ$ C in order to reduce reverse currents and reverse annealing. The innovative solution designed for VELO consists into the introduction of a 2-phase CO₂ cooling system, which loops through microchannels that are integrated directly into a silicon wafer. The use of such a silicon wafer has many advantages. Firstly, silicon has a high thermal conductivity (of the order of ~ 190 W/m K at -25° C), secondly the use of a wafer introduces a homogeneous material distribution and finally microchannels can be exploited to precisely route the cooling where it is needed. Also CO₂ results to be an optimal coolant choice, thanks to its high latent heat capacity, low viscosity and radiation hardness. The functional principle is the following: CO₂ enters the microchannel wafer as subcooled liquid from the pipes, passes through a 40 mm long restriction and then starts boiling in the main channel, just before going under the first ASICs. The 19 channels have dimension 120×200 μ m in main channels. The cooling performances are measured through the Thermal Figure of Merit,

defined as the ratio of temperature difference between coolant and power dissipating element and power density. At maximum module power (26 W) each tile consumes ~ 5.7 W, which corresponds to ~ 0.88 W/cm² of power density. From tests, the Thermal Figure of Merit is measured to be TFM = 3 – 4 K cm²W⁻¹, resulting to be much better compared to the ATLAS IBL integrated steel pipe cooling system, which is the best in LHC and has TFM = 13 K cm²W⁻¹. Thanks to this high efficiency, it is possible to withdraw the wafer of 5 mm from the innermost sensors, reducing the material budget without occurring the risk of thermal runaway.

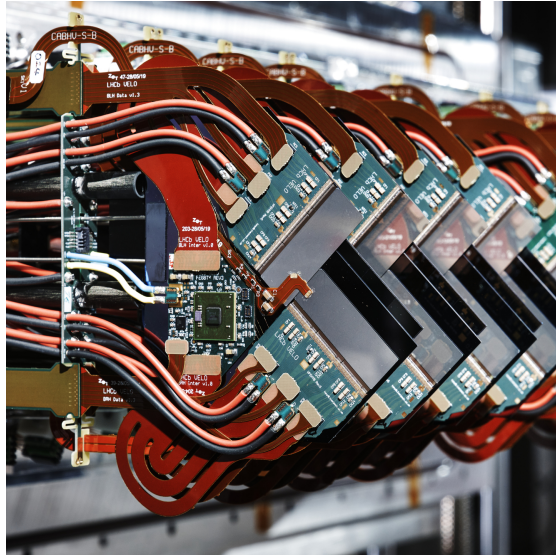


Figure 2.23: Photo of some VELO modules in a row taken during the assembly of the two halves. It can be observed that the innermost tiles are protruding of 5 mm from the support. From Ref. [36].

From simulation studies, the hit resolution is estimated to be $\sigma_{\text{hit}} = 12 \mu\text{m}$. This high level of precision, combined with their ability to read out data at a high frequency, makes VeloPix tiles an ideal choice for proof-of-principle tracking stations. To insert the detectors into the pipe vacuum, Roman Pots [37] could be used. These devices allow detectors to be positioned close to the beam without entering the machine vacuum, by connecting them to the accelerator vacuum via bellows. These designs are currently under study.

Simulation Framework

3.1 Simulation Software Description

3.1.1 DD4hep

DD4hep (*Detector Description for high energy physics*) [38, 39] is an open source toolkit created in 2012 and developed based on the experience on detector description systems gained from the LHCb experiment and from the developments proposed by the Linear Collider Community. The purpose of the software is to provide a complete description of detector models that includes not only the geometry and materials used in the device, but also parameters describing detection techniques, constants needed for alignment and calibration, descriptions of readout facilities and environment, and attributes needed for visualization. Each piece of information comes from a single source, which contains all the information needed for data interpretation at all stages, from simulation to reconstruction and analysis. This makes the framework consistent at every stage of the experiment life cycle.

DD4hep is built on the basis of existing widely used software packages. In particular, the geometric representation of the detector is implemented using the ROOT geometry package [40], a tool for building, browsing and visualizing geometries that also provides 3D visualization capabilities. On the other hand, the Geant4 toolkit [41] is used as a simulation engine to model the response of the detector to particle collisions. DD4hep interfaces directly with Geant4 through the use of specialized classes, providing for the conversion of all the information needed for the simulation and managing the run-time communication between the two software.



Figure 3.1: DD4hep and Geant4

Figure 3.2 depicts a diagram of all the main components of DD4hep and the interactions with each other and with end-user applications (simulation, reconstruction, alignment, and visualization). The user defines as input the *Compact Description* of the detector in XML format, an open format that offers the flexibility of introducing new elements and attributes. The detector is parameterized in minimalistic terms and the parameters are parsed by specific DD4hep classes. Given the high level of flexibility, these kinds of descriptions cannot be interpreted in a general way, so it is necessary to provide specialized code fragments, the so-called *Detector Constructors*. These pieces of code, written in C++ or alternatively in Python, contextualize the XML input and create a single instance of the detector, which can be combined with others to build complex configurations. Detector constructors are invoked by DD4hep using name conventions in the initialization phase, either from a set of pre-implemented basic geometric concepts or from those provided by the user. All the information provided at this stage is sufficient to build the detector model and visualize it.

The *Generic Detector Description Model* (GDDM) is the core element of DD4hep. It is based on ROOT’s TGeo geometry package, which is extended by including structural and functional features such as material properties, alignment constants, visualization, in order to build an in-memory model of the detector. Each part of a subdetector, which is organized in a hierarchy of components, is described as a *Detector Element* by specific classes that serve as a data container and provide easy access to desired subdetector information from external applications. Users can create extensions by overloading that classes. Each Detector Element instance is created by the Detector Constructors and from the GDDM model is possible to transform the detector, for example, into its Geant4 geometry representation. All the core functionalities are implemented in the DDCore package.

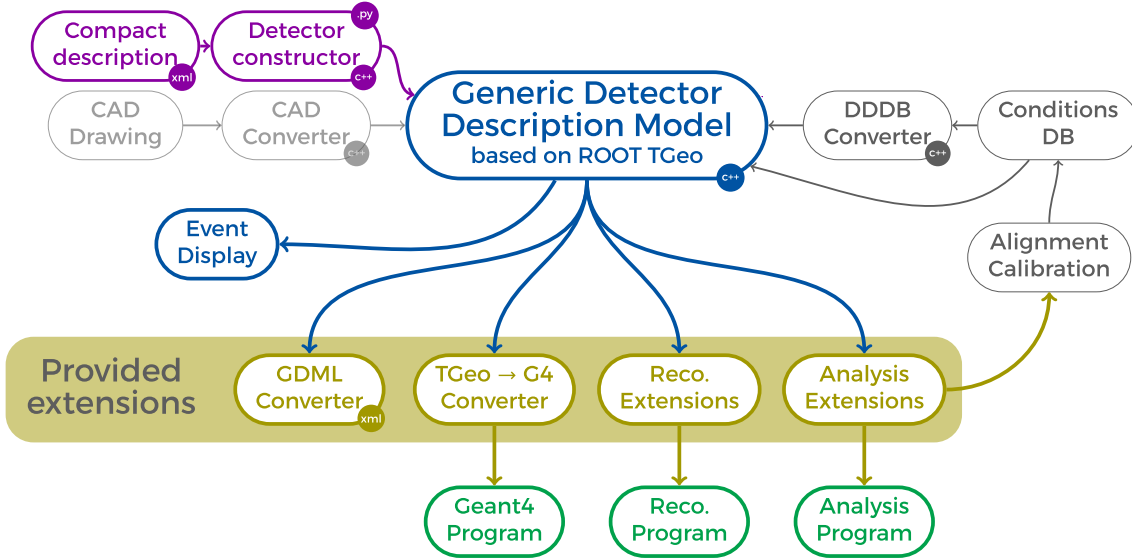


Figure 3.2: Diagram of the main components of the DD4hep detector geometry toolkit and its interactions with external software. Light gray components represent developments planned for the future. From Ref. [42].

3.1.2 Geant4

Geant4 is an object-oriented C++ toolkit for simulating the passage of particles through matter. It is a very comprehensive simulation software capable of describing every relevant step in the design process, including the geometry and material with which the system is made, the fundamental particles and their interaction processes, the generation and tracking of particles through materials and the external electromagnetic fields, the response of sensitive detector components and the storage of event and track data, and the visualization of the detector and particle trajectories. Geant4 also acts as a kind of repository of physical models of particle interactions, which is continuously updated and expanded.

Geometric structures are defined in steps. The so-called *Solids* describe shapes, e.g., boxes, spheres, tubes or others. The *Logical Volume* represents a detector element of a certain shape and material that may have other attributes that define its behavior, such as sensible properties. The *Physical Volume* represents the positioning and spatial orientation of the logical volume with respect to the surrounding mother-volume. The outermost volume that encloses everything else is usually called *World*. *Materials* can be composed of a single element or a mixture of elements, and the classes representing them contain all the information on intrinsic quantity like density, temperature, pressure and other physical characteristics such as radiation and interaction length, excitation energy loss, Bethe-Bloch formula coefficients, etc. *Particles* such as leptons, bosons, mesons, baryons, etc. are implemented in concrete classes instantiated as singletons to ensure that all physical processes, registered at the beginning of the simulation execution, refer to the same particle properties. Particles like quark and gauge bosons cannot be treated by Geant4.

The main unit of a simulation is the *Event*, described by a specific class. Before processing, an event object contains the primary vertices and primary particles as it interfaces with external physical event

generators, while, after processing, it contains generated hits and digitization and other information from the *Monte Carlo truth*. It also keeps in memory the mother-daughter relationships between the primary particles, so that a specific decay chain can be reconstructed from the physics generator.

It is called *Tracking* the procedure of moving a particle step by step according to its interaction with the material traversed and the external electromagnetic field. Throughout the simulation, each particle is described by a *Track* object, which contains particular information for each step of a particle, e.g., current position, momentum and energy, elapsed time since the start of the step, identification of the geometric volume in which the particle is located, etc. Based on their interaction lengths, all physical processes associated with the particle propose a *Step* and the smallest one is chosen by the step manager. Then, depending on the type of process (continuous or discrete), it may take an *at rest* action, if the particle is at rest (e.g., decay at rest) or an *along step* action, if the effects of the interaction process occur continuously along a step (e.g., energy loss in Cherenkov radiation or production of secondary particles), or a *post step* action, if it is invoked at the end of the step (e.g., production of secondary particles from a decay or interaction). This selection also takes into account geometric boundaries and user parameters. Each process implements these actions in a method of the type *Do It*, within which the equation of motion of the particle is solved, usually numerically by exploiting the fourth-order Runge-Kutta method if the field is nonuniform. Then, the particle moves one step following the calculated trajectory. Usually, this is the most critical aspect from the perspective of CPU time affecting simulation performances.

All the physics *Processes* have the same interface and are characterized by the definition of a particular initial and final state with an associated cross section or mean life. There are many categories of processes, characterized by different nature (discrete, continuous or other types); the most used in this application are decay, electromagnetic and hadronic. For example, in the decay case, the step length is calculated from the mean life, then, if this process is selected, the products are generated according to the branching ratios and the mother particle is killed. Furthermore, the electromagnetic physics category, which describes the interactions of leptons, photons, hadrons and ions, is itself divided into subcategories. The *standard electromagnetic* category consists into the processes of ionisation (including the δ -ray production), bremsstrahlung, multiple scattering, Compton and Rayleigh scattering, photo-electric effect, pair conversion, annihilation, synchrotron and transition radiation, scintillation, refraction, reflection, absorption and Cherenkov effect. Hadronic processes such as inelastic scattering are treated in a dedicated fashion.

Some parts of the detector can be instantiated as *Sensitive Detectors*. These types of logical volumes can create *Hit* objects, which collect information from a physical interaction at a particular instant, using the information provided by the track in the current step. Information about the hit is stored in an event object. Users must define the response of the sensitive detector: for example, a hit in a tracker is defined by the energy deposited within the volume by the transiting particle.

The class in which the user must describe the geometries, materials and sensitive properties of the detector is called *Users Detector Construction*. There are two other classes that the user must provide compulsorily and five others that are optional. The first two are *User Physics List*, which contains the definition of all the particles and physics processes involved, and *User Primary Generator Action*, which is responsible for generating the particles and primary vertices. The other five are *User Run Action*, *User Event Action*, and *User Tracking Action*, which act, respectively, at the beginning and end of each run, event, and tracking procedure (creation and completion); then *User Stepping Action*, to change the behavior at each step; and finally *User Stacking Action*, which handles the stacks of tracks. These are first-in-last-out type containers, in which particles are classified as “urgent”, “waiting” or “postpone to the next event” and, so, treated differently.

3.1.3 DDG4: the DD4hep interface to Geant4

DDG4 [43] is the DD4hep package that manages the simulation by interacting directly with Geant4. It is designed to follow the sequential steps of Geant4 that can be configured by exploiting specific classes called *Action Sequences*, which are responsible for building complete Geant4 execution blocks and objects. These components, which in particular consist of the classes *Run*, *Event*, *Tracking*, *Stepping*, *Stacking*, and *Generator Action Sequence*, feature a callback mechanism that provides continuous communication between them and the corresponding Geant4 classes explained in Section 3.1.2. The translation from the GDDM representation of the detector to the Geant4 representation is handled automatically, including geometry, material, volumes, and placement conversion, while the instantiation of the objects and plugin components is based on a *factory* mechanism. All plugins, that manage the details of the simulation, are implemented by inheriting from a common base class, the *Action*, in order to simplify its use, manage all the common functionalities, such as configuring component properties through the *Property Manager*, and provide access to all the objects needed to run the simulation, thanks to the so-called *Geant4 Context*. With this common structure, specific sequences of actions such as those mentioned above can be constructed. It is also important to note that through this mechanism, DDG4 supports the possibility for the user to add extended plugins according to specific needs.

The particles that constitute the simulation input can be generated by Geant4 (for example, by exploiting a *Particle Gun*) or can be read from external files created by generators in the LCIO, StdHEP or HepMC [44] format. The primary interactions are then manipulated by specific modules that can introduce, for example, smearing or boosting of primary vertices. The *Physics List* must be provided by the user via an XML format file, from which particle constructors, physics processes and physics constructors are instantiated by a specific set of factories. The detector response is handled by the *Sensitive Detector Action*, which calculates the energy deposition of a given step in a sensitive volume and creates the hits. Information about the energy deposition and the position of the hits created during the simulation in each sensitive detector is stored in a ROOT output file. In addition, this output file also contains the *Monte Carlo truth* information, i.e., the general characteristics and initial and final kinematic properties of all particles treated in the simulation (not only those passing through a sensitive volume).

Simulation configuration must be provided via an XML file (but this is a fairly deprecated method nowadays) or via a Python script. It should contain all the information needed to read and convert geometry from GDDM format to Geant4, to configure action sequences, and to start Geant4 execution.

3.1.4 Crystal Channeling routine in Geant4

A Geant4 routine capable of simulating all the phenomena described in Section 2.3 is available from Geant4.10.1. The complete description of the model developed to simulate the orientational effects of charged particles interacting with bent crystals under conditions of planar channeling and volume reflection is given in [45].

The Geant4 Channeling routine includes a framework for handling solid-state crystal structures [46]. A specialized logical volume called *Logical Crystal Volume* handles the orientation of the crystal axes, defined by Miller indices, with respect to the solid to which the crystal is attached. This type of volume can only be realized by an *Extended Material*, which is derived from the base class *Material* and can offer the possibility of registering some extensions to define additional material information. The extension that contains information about the physical properties of a perfect crystal is called *Crystal Extension*. It can define and store all properties describing the base of the atom, atomic bonds and unit cell of the crystal, including the dimensions and angles of the base cell and lattice system. Methods for calculating volume in direct and reciprocal space, distance and angle between two planes, and other properties are also provided.

Another important extension is the *Channeling Material Data*, which collects information on the electric field, potential, nuclei, and electron density of the crystal under the continuous potential

approximation. These density and field maps are calculated with external software that makes use of a method called ECHARM [47] based on the equations of classical physics and on the Fourier expansion of periodic functions in a periodic structure. Data files containing the results of the calculations are loaded into the simulation framework by means of the *Channeling ECHARM* class. The Channeling Material Data extension also manages the curvature properties of the crystal lattice, providing the possibility to set the bending radius. Until the current version, it is only possible to define curvature in the xz plane so particles can only be deflected horizontally.

The core element of the simulation routine is the Channling process. It is defined as a discrete process, so only a method of the type “post step do it” is provided: after each step, the function checks whether the volume in which the particle is located has a lattice, the channeling condition is evaluated, and if it is satisfied the channeling equation of motion is integrated with the Runge-Kutta algorithm by updating the position and momentum of the particle as well as the electron and nuclei density experienced by the particle during its motion. In this way, the trajectory of the particle is aligned with the direction of the channeling plane. In the first step inside the crystal, the position in the channel is randomly generated using a uniform distribution, and this value is used to calculate the initial potential energy. If the particle has dechanneled or exited the crystal, the outgoing angle is evaluated.

Since at each step the momentum of the particle can be changed by any of the Geant4 processes that modify the transverse energy of a particle, possibly causing dechanneling, it is also possible to apply biasing techniques to scale the cross section of such processes proportional to the average nuclei and electron density experienced by a channeled particle. This can be done through the class *Channeling Operator Change Cross Section*.

The current version, Geant4.11.1, provides an example of usage of this channeling routine¹. The code is meant to reproduce the setup and the measurements of the experiment performed at SPS in 2009 [48].

The geometry of the setup, defined in the Detector Construction, consists of a world of vacuum of type *Galactic* within which a silicon crystal and three silicon scoring planes are placed in order to measure the incoming and outgoing angle of particles after interaction with the crystal. The crystal is defined by a box shape of size $1.00 \times 70.00 \times 1.94$ mm³ made of extended material constructed from silicon, to which the crystal extension (defining, for example, the unit cell of the crystal of size $d_{\text{cell}} = 5.43$ Å as given in Table 2.2) and the channeling material data extension are registered. The default value of the bending radius, defined horizontally in the xz plane, is $R = 38.416$ m, which corresponds to an bending angle of $\theta_C = 50.5$ μ rads. It is important to note that in Geant4 the shapes and materials are treated independently, therefore the bent crystal can be defined in first approximation as a box made of a material that is, instead, curved: in fact, the bending is a property of the lattice and not of the volume. The curvature of the crystal occurs at its barycenter stretching the extremity of the shape, so in the placement phase it is necessary to rotate the volume with respect to the y axis by half the angle of curvature $\theta_{\text{rot},y} = -25.25$ μ rads to align the lattice planes at the crystal entrance with the z axis, since the beam is also aligned in that direction. Without this rotation, the particles cannot be channeled and undergo volume reflection. The crystal is placed in the world volume with its barycenter in the origin. The silicon detectors have dimensions $38.00 \times 38.00 \times 0.64$ mm³ and are placed at positions $z = -9.998, -0.320, +10.756$ m, one immediately after the particle source, one before the crystal and one far after the crystal. They are defined as sensitive detectors and particle hits management is handled by a specialized class.

Primary events are generated by a *General Particle Source*, defined in the primary generator action, which consists of a proton gun of energy 400 GeV launched from $z = -10.5$ m. Geant4 also offers the possibility of sampling the position and initial angle at which the particle is shot from a certain

¹In `examples/extended/exoticphysics/channeling`.

distribution chosen by the user, thanks to the classes *Single Particle Source Angular* and *Position Distribution*. By choosing the two-dimensional beam shape, the initial angles and positions are sampled from Gaussian distributions, where the standard deviations are provided by the user. In this example, the beam is selected to have just a two-dimensional angular divergence with $\sigma_{\theta_x} = 13.36 \mu\text{rad}$ and $\sigma_{\theta_y} = 11.25 \mu\text{rad}$.

In addition to the standard electromagnetic physics list , an additional one loops over all particles and registers the channeling process to all of them. When defining physics lists, the biasing mechanism can also be invoked. A run action and an event action are also defined to handle the simulation. The former creates at the beginning of the execution a ROOT file and a tuple to record the physical information of interest and saves the file at the end of the execution, while the latter stores this information in the tuple at the end of each event by retrieving the data from the sensitive detector hit. The physical quantities stored are the angle in x and y of the particle arriving at the crystal, the position x and y of the particle hit at the crystal entrance, and the angle in x and y of the particle leaving the crystal. All these angles are calculated assuming the small-angle approximation, and the outgoing ones are obtained by considering the barycentre of the crystal as initial reference.

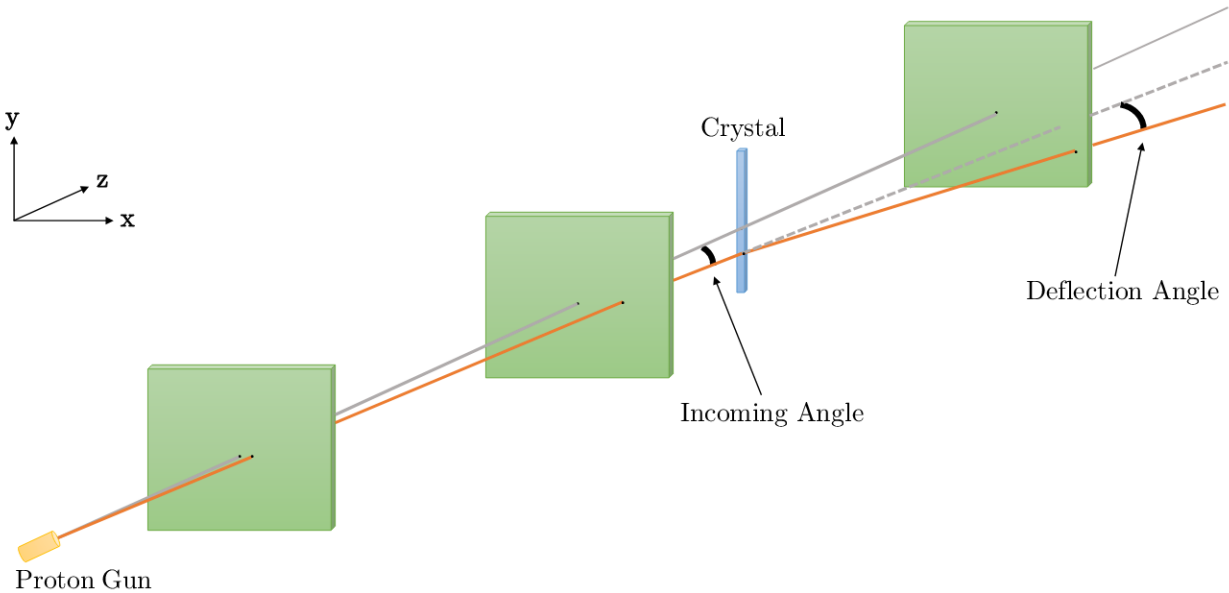


Figure 3.3: Diagram (not to scale) of the Geant4 example setup implemented to illustrate the channeling routine. The incoming angle is calculated by taking as reference the position of the gun and the position of the particle at the entrance of the crystal. The deflection angle is calculated by taking as reference the barycentre of the crystal and the position of the hit in the third tracker. Both are calculated using the small-angle approximation.

This Geant4 channeling routine is continuously maintained and updated; in fact, several tests are performed to validate it through comparison with real experiments [45,49]. The results of a 10000-event simulation with all default options was already shown in the two-dimensional histogram of Fig. 2.15, which reports the incoming and outgoing horizontal angular distributions. Figure 3.4 illustrates the distribution of the horizontal deflection angle, i.e., the projection on the y -axis of the plot in Figure 2.15, from which the two peaks of channeled and unchanneled particles are clearly visible, while Figure 3.5 shows the channeling efficiency as a function of the horizontal incoming angle, calculated on the results of that simulation. The efficiency is defined as in [50] by considering the number of particles within the peak of the deflection angle θ_{defl} . The two-dimensional distribution of Figure 2.15 is projected onto the vertical axis over 20 fixed-size bins, between $[-10; 10] \mu\text{rad}$, then the peak is fit with a Gaussian curve between $35 \mu\text{rad}$ and $50 \mu\text{rad}$, and the resulting Gaussian mean and standard deviation parameters, $\mu_{\theta_{\text{defl}}}$ and $\sigma_{\theta_{\text{defl}}}$, are used to calculate the channeling efficiency

$$\varepsilon_{chann} = \frac{N_{\text{chann}}}{N_{\text{tot}} \cdot c} \quad (3.1)$$

where N_{chann} is the number of particles in the range $[\mu_{\theta_{\text{defl}}} - 3\sigma_{\theta_{\text{defl}}}, \mu_{\theta_{\text{defl}}} + 3\sigma_{\theta_{\text{defl}}}]$, N_{tot} is the total number of particles and c a scaling factor that takes into account normalization with respect to the amorphous case. The results of this efficiency analysis are compared with those of one of the SPS experiments [48] (blue curve in Figure 3.5). From the graph, it can be seen that the Geant4 channeling routine turns out to overestimate the efficiency compared with the real case.

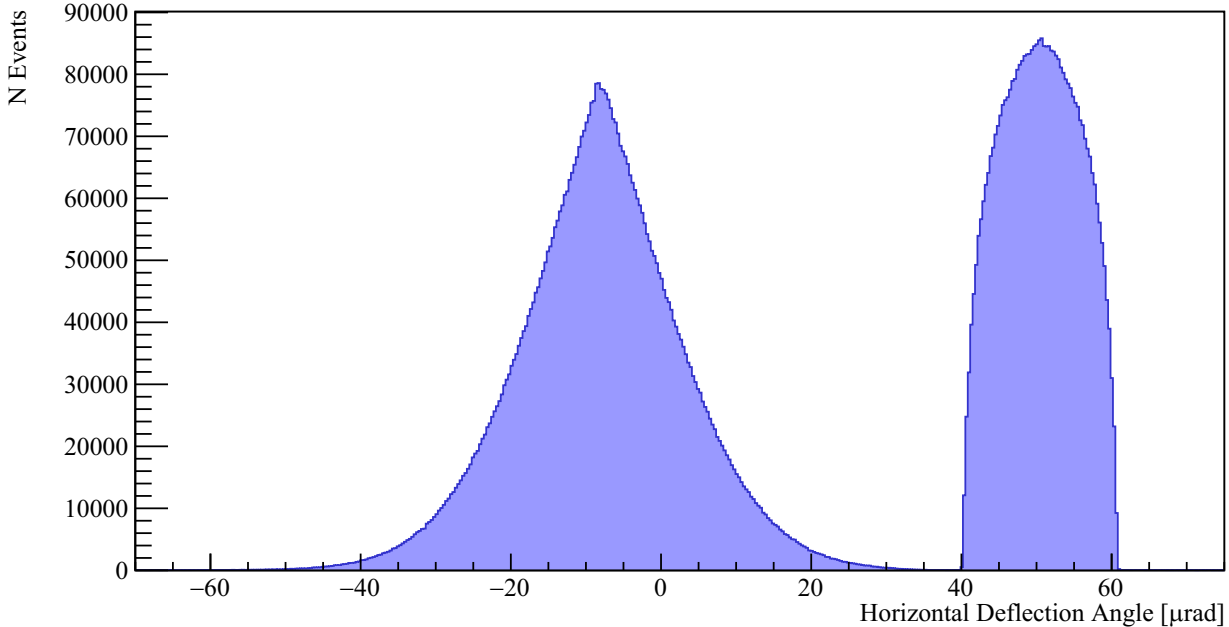


Figure 3.4: Distribution of the crystal deflection angle obtained from a 10000-events Geant4 simulation performed with all the default options (i.e. projection on the y -axis of the 2-dimensional plot in Figure 2.15). The channeling peak centered in $50.5 \mu\text{rad}$ is clearly visible.

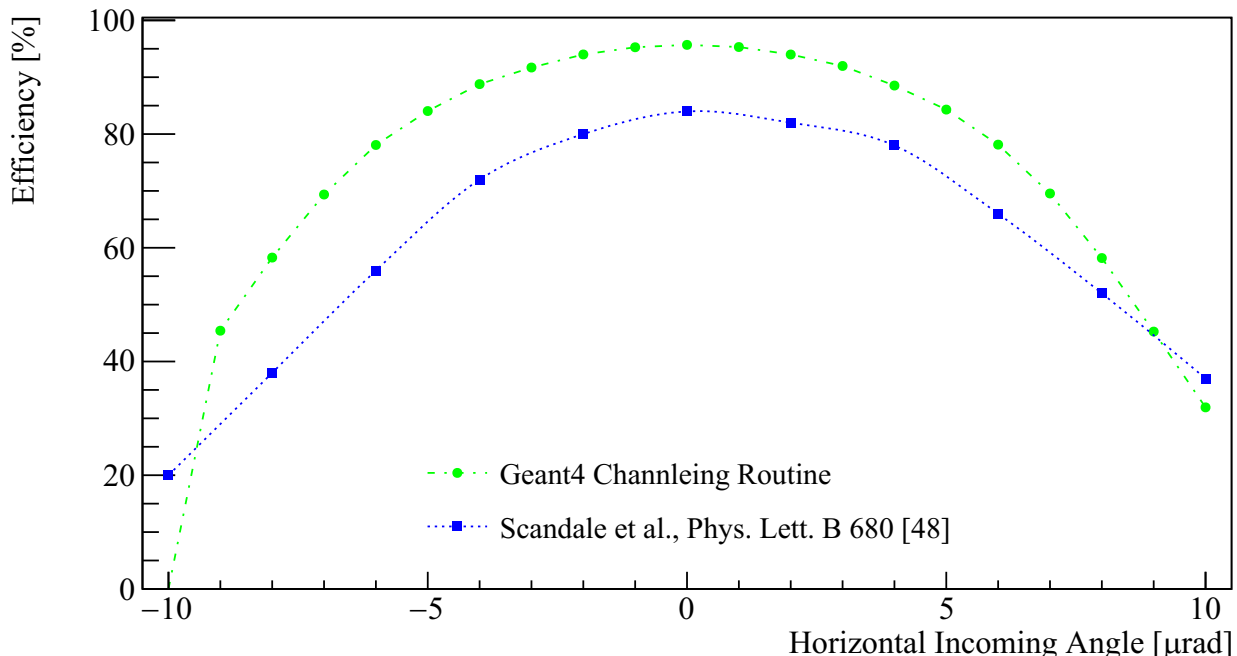


Figure 3.5: Comparison of the experimental channeling efficiency (blue squares) [48] and the simulated channeling efficiency (green dots). The Geant4 channeling routine turns out to overestimate it with respect to the real case.

3.2 IR3 Detector implementation in DD4hep

The IR3 setup sketched in Figure 2.17 is implemented in DD4hep. A compact description of all materials involved and of the target, precession crystal, beam pipe, magnet, and trackers is provided. The crystal and the target are implemented as boxes with nominal dimensions reported in Table 2.3. In DD4hep the rotations are defined with the opposite sign convention from Geant4, hence, when the crystal position is defined, it must be rotated by half the bending angle in the opposite direction with respect to the implementation in Geant4. The first 4 of the 8 scoring planes are denoted as Tracker 1_1, Tracker 1_2, Tracker 1_3, Tracker 1_4 while the last 4, placed downstream the magnet, are denoted as Tracker 2_1, Tracker 2_2, Tracker 2_3, Tracker 2_4. They are implemented as thin boxes of dimension $150 \times 150 \times 0.2 \text{ mm}^3$ made of sensitive silicon. The four planes of each group are placed equidistantly in a region of 40 cm length in z . Tracker 1_4 is placed 1.04 m away from the centre of the crystal. The beam pipe is made of two pieces, one that contains the crystal and the target and ends just in front of the first tracking plane and one that extends through the full length of the magnet. It is made of aluminium with a thickness of 2 mm and has an elliptical shape with $r_{\min} = 2.94 \text{ cm}$ and $r_{\max} = 3.14 \text{ cm}$. A specific Detector Constructor written in C++ must be provided to instantiate such component. The magnet is an iron box of dimension $49.4 \times 67.6 \times 170 \text{ cm}^3$ with a central bore of size $5.2 \times 14.4 \times 170 \text{ cm}^3$, inside which the second piece of the pipe is placed. To perform such a solids subtraction, another Detector Construction code is required. The magnetic field map in the bore is still being studied; for the time being, a constant field of magnetic flux density $B = 1.1 \text{ T}$ is implemented in the core gap. It is important to note that, apart from the crystal and the target specifications, all other parameters are not final and are under study in these simulations to be optimized. The ROOT TGeo visualization of the IR3 Detector is shown in Figure 3.6.

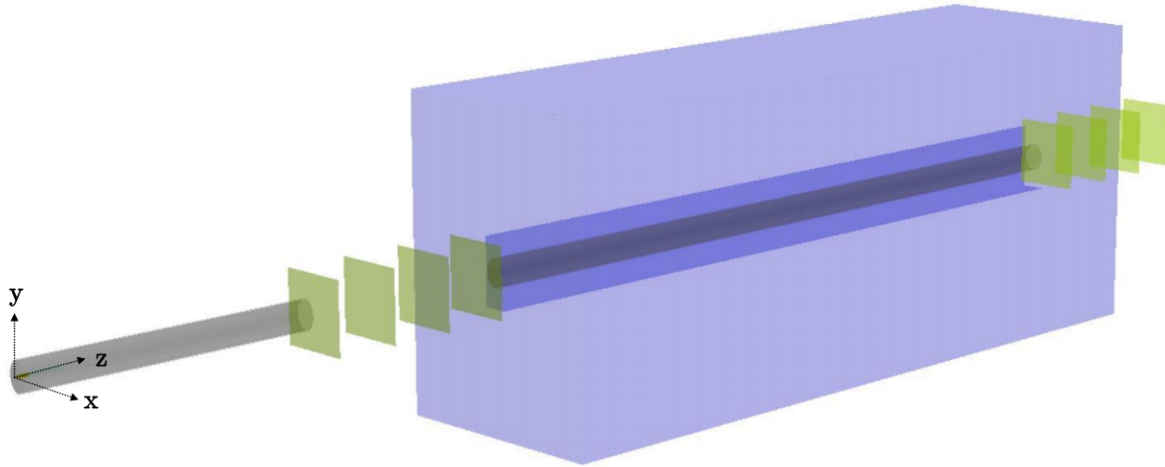


Figure 3.6: Visualization via ROOT TGeo of the IR3 detector implementation in DD4hep. The 8 trackers are shown in green, the magnet in blue, and the beam pipe in gray. Starting from the origin, the target and CRY2 are also visible.

As for simulation, a set of basic options are defined by making use of a Python script. To reproduce the conditions described in (ii) of Section 2.4.1, the generator can be chosen as a 1 TeV gun placed just in front of the crystal entrance face. To reproduce, instead, the conditions described in (iii), the input interactions must be read from a HepMC-format file containing the results of the simulation of minimum biased proton-tungsten collisions, performed with the Pythia 8 Angantyr [51] software². The basic physics list is the so-called FTFP-BERT-EMX list. This physics list combines the Bertini cascade process for hadron–nucleus interactions from 0 to 5 GeV incident hadron energy, and the FTF parton string model for hadron–nucleus interactions from 4 GeV upwards. It is also possible to select electromagnetic physics constructor on top of a particular hadronic physics; in particular with the EMX extension, the standard electromagnetic physics list “option 2” is selected, which is a simplified version used in LHCb simulation applications. However, in order to avoid the occurrence of infrared

²Thanks to Patrick Robbe, IJC-lab.

divergence in some electromagnetic processes characterizing gammas, electrons and positrons, it is necessary to introduce a production threshold, determined by a range cut-off distance. This distance is, then, internally converted into a specific energy value for the material used. For this simulation, the cut-off distance is set to a value of 0.7 mm.

3.2.1 Introduction of the Channeling routine in DD4hep

As explained in Section 3.1.4, the channeling properties of crystals in Geant4 are contained within the physics list, in which the channeling process is registered for each particle, within the volume definition, since the derived logical volume class of crystals contains information about the crystal lattice, and within the material definition, due to the possibility of extending its properties.

As of the August 10, 2022 release of DD4hep, channeling physics is supported by the software, enabling the transparent creation of extended materials and derived logical volume instances. DD4hep provides a *Converter* class responsible for creating materials and volumes from DD4hep to Geant4. The general idea of the update is that material and volume extensions are handled by this class making use of new plugins that call new specialized factories³. The information for activating the correct plugin mechanism and about the parameters needed to create the instances can be passed through an XML `<property>` node in the case of volumes, or through an XML `<constant>` node in the case of materials, via the compact input file. The converter class reads this command from the XML file and calls the channeling volume factory and the channeling material factory. Within these classes the Geant4 code provided in the detector construction class of the example explained in Section 3.1.4 is adapted to the DD4hep framework. In the current implementation, only the location of the ECHARM data file and the bending radius⁴ can be chosen at the configuration step of the compact description; all other parameters, e.g., the choice of silicon unit cell usage, are hardcoded.

A material supporting channeling must be defined by the user in the material list from which elements can be selected to describe the detector components. This new material has to be included in the compact description of CRY2. In addition, the volume property must be provided at this stage. In order to handle this modification and create a silicon crystal box that supports channeling, a code for the C++ Detector Constructor must also be added⁵.

Regarding simulation, thanks to the updates in this new software release, it is possible to include channeling physics by taking advantage of a new DD4hep *Physics Constructor*, which reproduces the behavior of the Geant4 physics list by recording the channeling process at all particles. It can simply be included in the simulation python script⁶.

3.2.2 Development of new plugins for the IR3 detector simulation

DD4hep offers the user the ability to create new plugin classes to overload and expand existing ones to add extra functionality. A factory macro must be invoked for each new class introduced, and the path to the new file must be included in the Cmake list containing information for the application compiler.

For the IR3 detector simulation, 4 new plugins were needed and introduced to provide a more realistic description of the beam and primary interactions and to handle the huge number of particles created during execution.

A Stacking Action is developed to introduce the possibility of killing all the secondary particles, as in the Geant4 example, or to kill just the electrons if necessary to speed up the simulation. This deactivation of particles occurs before they are physically placed in the volume in which the simulation takes place and thus before they can perform the first step. A Stepping Action is introduced to kill

³In DD4hep/examples/DDG4/src/

⁴which is mistakenly called “orientation”

⁵https://gitlab.cern.ch/elspadar/ir3detector/-/blob/temp.Chiara/src/Crystal_box.cpp

⁶https://gitlab.cern.ch/elspadar/ir3detector/-/blob/temp.Chiara/sim/ddg4_ir3.py

particles that verify specific conditions, as explained and motivated in Section 4.1. These filtering conditions are checked at each step along the particle's path in the simulation.

Unlike Geant4, the default version of DD4hep does not offer the possibility to define through the particle gun a 2-dimensional Gaussian beam that samples angles and initial positions from a Gaussian distribution. An extension is implemented to include this feature in the simulating framework, allowing the user to set the standard deviations σ_x , σ_y , σ_{θ_x} , σ_{θ_y} . The initial position of the gun and thus of the track vertex is shifted by the deviations Δx , Δy sampled from a distribution $\mathcal{N}(0, \sigma_{x,y}^2)$. The angular aperture of the beam is also sampled from a Gaussian distribution $\Delta\theta_x, \Delta\theta_y \sim \mathcal{N}(0, \sigma_{\theta_x,\theta_y}^2)$ and the polar and azimuthal angle are calculated as $\theta = \sqrt{\Delta\theta_x^2 + \Delta\theta_y^2}$ and $\phi = \arccos(\frac{\Delta\theta_x}{\theta})$ to set the new track direction $d = (\sin\theta \cos\phi, \sin\theta \sin\phi, \cos\theta)$. Note that if $\Delta\theta_y < 0$ the azimuthal angle must be corrected and set to $-\phi$, while if $\theta = 0$ the angle must be set to $\phi = 0$. In the context of the IR3 detector simulation, the standard deviations of the 1 TeV beam distribution at CRY2 entrance are obtained from a Gaussian fit⁷ performed on data simulated with SixTrack [52], which is a simulation software used mainly at LHC for studies of dynamic aperture, tuning optimization and collimation. The results of the fit are given in Table 3.1 and the histogram showing the spot of channelled particles arriving at CRY2 is shown in Figure 3.7.

	μ	σ	3σ
x	0.096 mm	0.583 mm	1.75 mm
θ_x	0.852 μ rad	10.5 μ rad	31.4 μ rad
y	8.42 mm	0.525 mm	1.58 mm
θ_y	63.0 μ rad	5.25 μ rad	15.8 μ rad

Table 3.1: Results of a Gaussian fit performed on the positions and angular distributions of a 1 TeV proton beam at the level of CRY2 entrance. The analyzed data are the outcome of a SixTrack simulation in the setup conditions (ii) explained in Section 2.4.1. From Ref. [53].

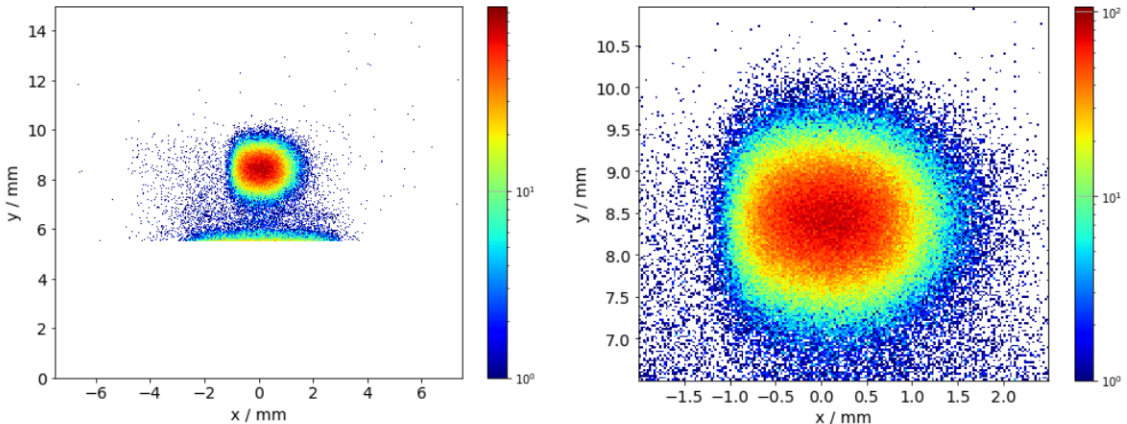


Figure 3.7: Position distribution of a 1 TeV proton beam at the level of CRY2 entrance obtained with a SixTrack simulation in the setup conditions (ii) explained in Section 2.4.1. The plot on the right is a zoom of the plot on the left. From Ref. [53].

When the target is introduced, it must be taken into account that the incident proton interacts with the protons of the tungsten nuclei with a certain probability throughout its traversal along the extension L_T of the target along z . Secondary particles are produced from these collisions through nuclear interaction, including Λ_c^+ . The physical quantity that describes the average distance traveled by a particle between nuclear collisions is the mean free path λ_{int} which is defined as

$$\lambda_{\text{int}} = \frac{1}{\sigma_{pA} \cdot N} \approx \frac{A}{\sigma_{pp} A^{2/3} \cdot N_A \rho_T} \propto A^{1/3}, \quad (3.2)$$

⁷Thanks to Kay Dewhurst, BE-ABP-NDC

where σ_{pA} is the proton-nucleus cross section, which can be deduced as a rule of thumb from the proton-proton inelastic cross-section to be $\sigma_{pA} \approx \sigma_{pp} A^{2/3}$ with $A \approx 183.8$ g/mol the tungsten molar mass, $N = N_A \rho_T / A$ the atom density, $\rho_T \approx 19.3$ g/cm³ the tungsten material density and N_A the Avogadro number. Applied to the case of a tungsten target, the mean free path turns out to be $\lambda_{\text{int}} \approx 9.946$ cm. Given a beam initially composed of N_0 protons, the number of particles N that survive nuclear interactions decreases exponentially with the traversed thickness z

$$N(z) = N_0 \exp(-z/\lambda_{\text{int}}) . \quad (3.3)$$

Therefore, the probability that a particle has an interaction between z and dz is expressed by an exponential density function with rate parameter $\lambda = \lambda_{\text{int}}$.

A plugin has been developed for DD4hep that allows the primary interactions read from a HepMC file to be smeared by sampling the initial positions of the x and y beam vertices and the angular directions θ_x and θ_y from a Gaussian distribution and shifting the z position sampling of from an exponential distribution. The user can provide the standard deviations of the Gaussians and the interaction length. As for the IR3 detector simulation, σ_x , σ_y , σ_{θ_x} , σ_{θ_y} are again obtained from Gaussian fits on the result of a SixTrack simulation of a 6.8 TeV beam, the results of which are given in Table 3.2. After defining the initial conditions and being launched, these primary particles are processed by Geant4 producing other interactions and particles (including Λ_c^+) through cascade effects. Note that Geant4 does not produce charms unless it is specifically configured for that.

	μ	σ	3σ
x	0.019 mm	0.229 mm	0.686 mm
θ_x	0.579 μ rad	4.65 μ rad	13.9 μ rad
y	8.45 mm	0.166 mm	0.497 mm
θ_y	77.4 μ rad	1.66 μ rad	4.97 μ rad

Table 3.2: Results of a Gaussian fit performed on the positions and angular distributions of a 6.8 TeV proton beam at the level of CRY2 entrance. The analyzed data are the outcome of a SixTrack simulation in the setup conditions (iii) explained in Section 2.4.1. From Ref. [53].

Tests are conducted to ensure that the Geant4 routine and the newly introduced plugins behave the same in the DD4hep framework. A simulation is run with the same parameters first in Geant4 and then in DD4hep and the results are compared. The setup consisting of trackers and crystal is identical to that in the Geant4 example explained in Section 3.1.4 and pictured in Figure 3.3. The FTFP-BERT physical list is taken as a baseline reference and no bias was applied. To test the new DD4hep plugin and recreate the same condition in both cases, the Stacking Action which kills all secondary particles is activated. The particle source is set up as a 400 GeV proton beam with angles and initial positions sampled from Gaussians whose standard deviations are as given in Table 3.1, so that the proton beam gun plugin is also tested. A ROOT macro was developed to analyze the result of the DD4hep simulation and calculate the same physical quantities calculated in the Geant4 event action. A 10000 events simulation is run, but only particles that hit all 3 trackers are considered valid for analysis. Figure 3.8 shows the outgoing horizontal angle of particles deflected by the crystal obtained from the Geant4 simulation (9942 valid events) while Figure 3.9 shows the same distribution obtained from the DD4hep simulation (9094 valid events). It can be seen that the two graphs are similar in shape, and it can be concluded that the channeling routine works correctly in DD4hep. Figures 3.10 and 3.11 show the position distributions x and y detected by the first tracker (the one placed at 50.2 cm from the particle source), while Figures 3.12 and 3.13 show the input angular distribution of θ_x and θ_y calculated assuming the small-angle approximation by taking the position of the particle gun and the position of the particle at the entrance face of the crystal as reference. Also shown on the plots

are the standard deviations obtained from Gaussian fits on the results. It can be seen that they are all compatible with those set by the user, when compared with Table 3.1.

A problem in the Geant4 implementation was found when trying to implement a crystal with bending radius lying in the yz plane, as planned in the experiment. A simple rotation of the crystal box produces erroneous results. This issue is currently still under expert study. For the time being, a workaround has been adopted whereby the entire geometry of the simulation framework is rotated 90° around the z axis.

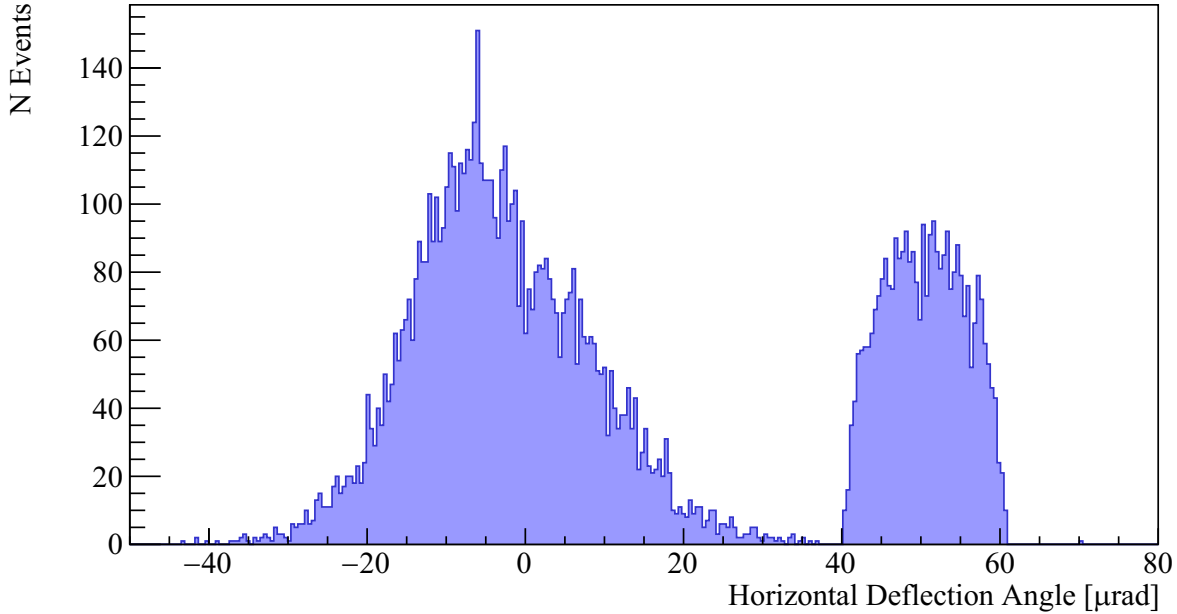


Figure 3.8: Distribution of the crystal deflection angle obtained from a 10000-events Geant4 simulation. The number of valid tracks (i.e. the number of entries) is 9942.

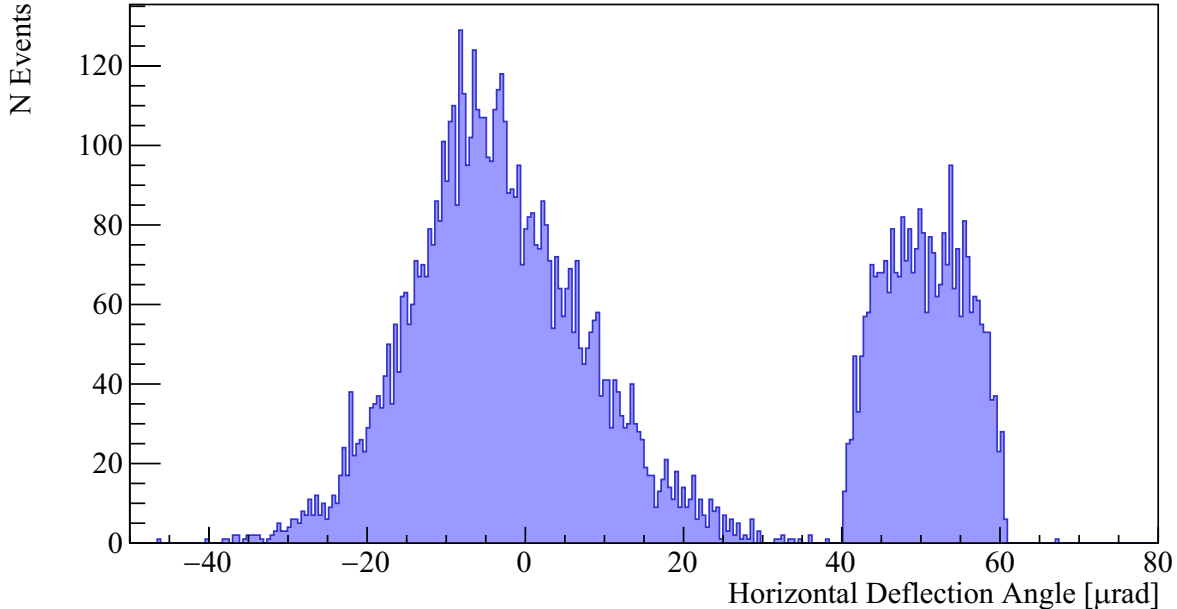


Figure 3.9: Distribution of the crystal deflection angle obtained from a 10000-events DD4hep simulation. The number of valid tracks (i.e. the number of entries) is 9094.

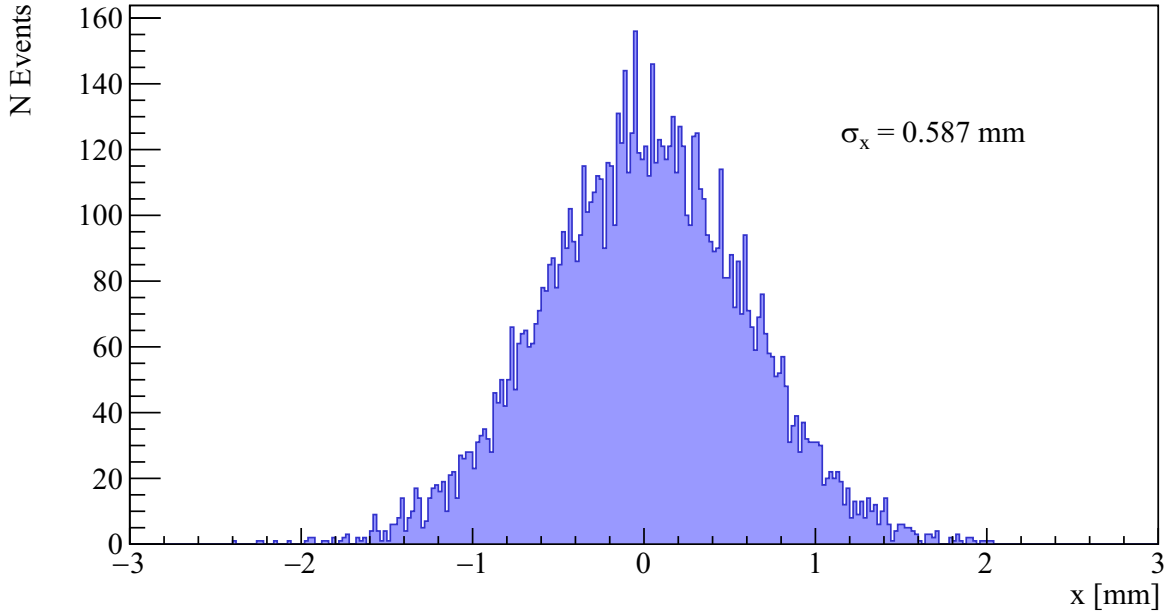


Figure 3.10: Distribution of the x hit position in the first tracker placed at distance 50.2 cm from the particle source obtained from a 10000-event DD4hep simulation. The number of valid tracks (i.e., the number of entries) is 9094. The standard deviation obtained from the fit is comparable to the nominal one set as the simulation parameter $\sigma_{x,\text{nom}} = 0.583$ mm.

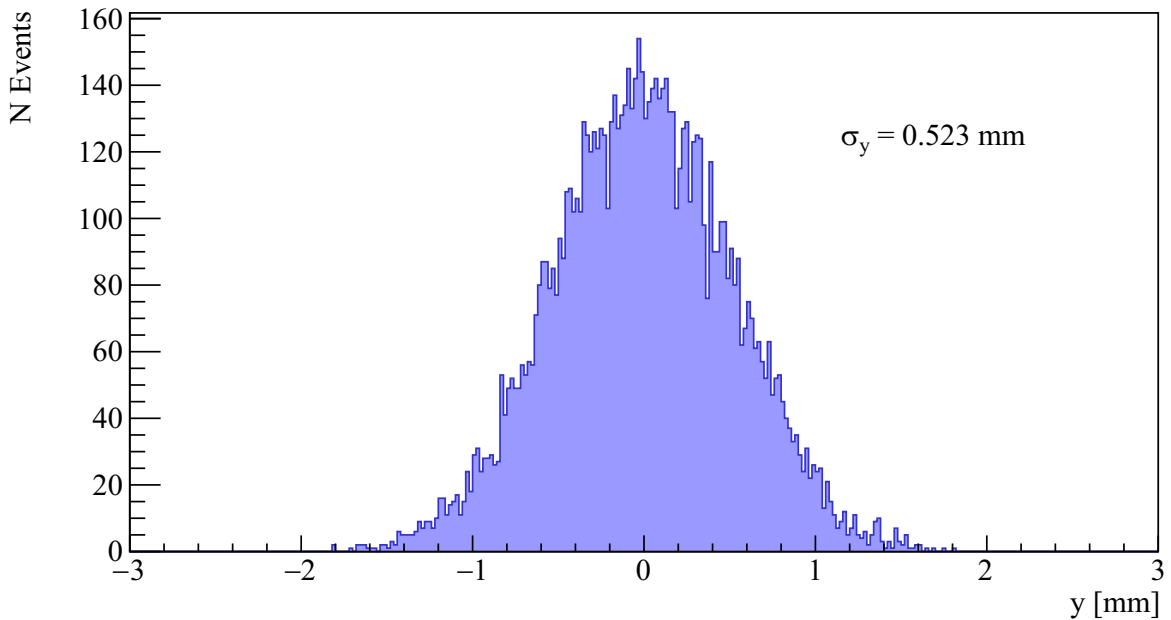


Figure 3.11: Distribution of the y hit position in the first tracker placed at distance 50.2 cm from the particle source obtained from a 10000-event DD4hep simulation. The number of valid tracks (i.e., the number of entries) is 9094. The standard deviation obtained from the fit is comparable to the nominal one set as the simulation parameter $\sigma_{y,\text{nom}} = 0.525$ mm.

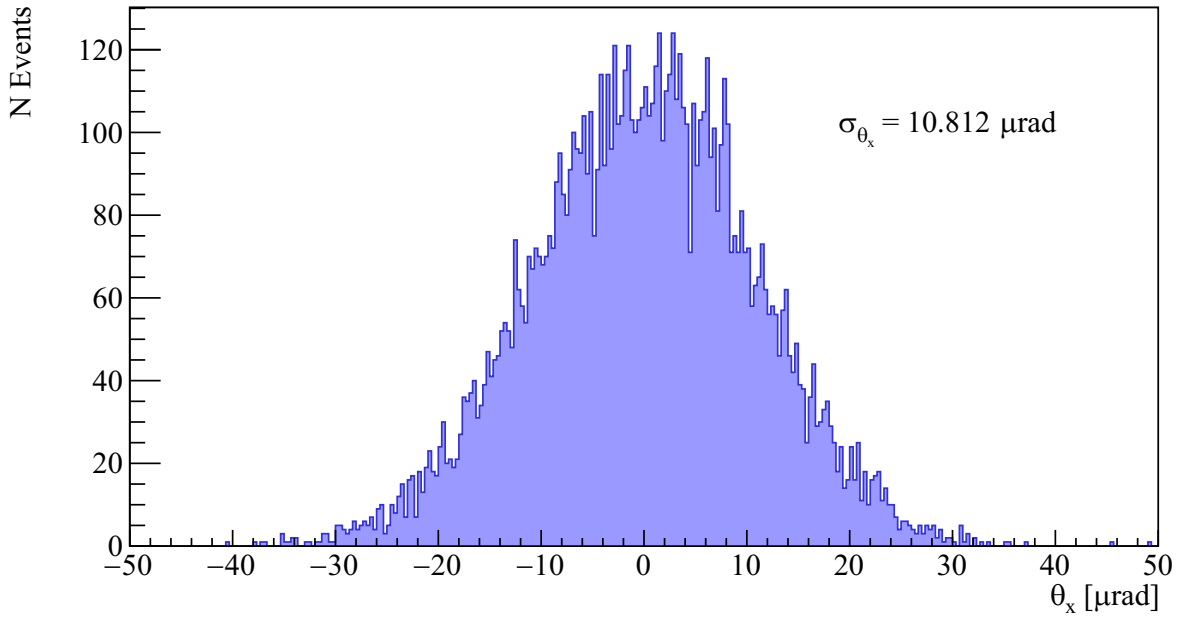


Figure 3.12: Distribution of the crystal incoming angle θ_x obtained from a 10000-event DD4hep simulation. The number of valid tracks (i.e., the number of entries) is 9094. The standard deviation obtained from the fit is comparable to the nominal one set as the simulation parameter $\sigma_{\theta_x,\text{nom}} = 10.50 \mu\text{rad}$.

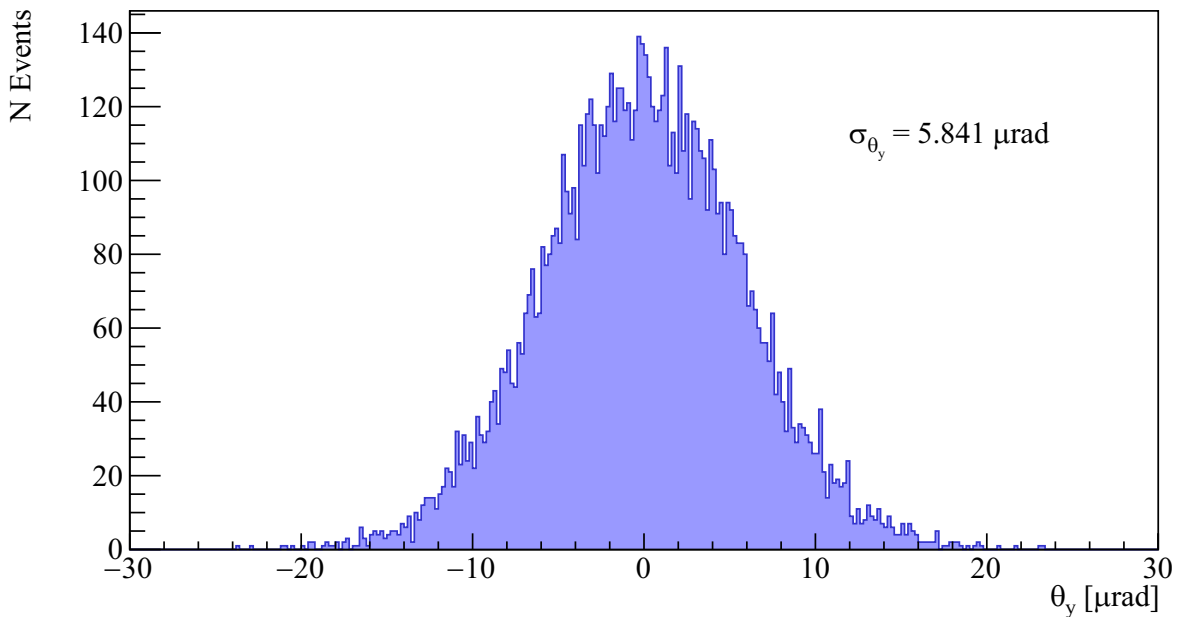


Figure 3.13: Distribution of the crystal incoming angle θ_y obtained from a 10000-event DD4hep simulation. The number of valid tracks (i.e., the number of entries) is 9094. The standard deviation obtained from the fit is comparable to the nominal one set as the simulation parameter $\sigma_{\theta_y,\text{nom}} = 5.25 \mu\text{rad}$.

Proof of Principle tests

The purpose of the following preliminary tests is to provide a rough estimate of the amount of background and signal particles that can be observed in a scoring plane positioned after CRY2 in the conditions of the proof of principles. Background means all particles created in the interactions of the primary particles with the crystal (and, if introduced, with the target) and thus represents the set of all particles for which we are not interested in studying the channeling phenomenon in CRY2. On the other hand, signal means the particles whose channelling behaviour is to be observed. In the case where only CRY2 is introduced (step (ii) of the Section 2.4.1), the signal thus consists of the protons deflected by CRY1 and incident on CRY2, which may or may not undergo channelling.

4.1 CPU time analysis

A first DD4hep simulation run is performed with the following minimal setup:

- CRY2 positioned with the vertical entry face at $z = 2$ cm
- A proton gun of energy $E_p = 1$ TeV placed just before the entry face of the crystal that samples initial x , y , θ_x and θ_y of the primary particles from a Gaussian distribution defined with the parameters given in Table 3.1
- A silicon scoring plane of dimensions $150 \times 150 \times 0.2$ mm³ placed at a distance $d = 1.04$ m from the centre of crystal (Tracker1_4 described in Section 3.2).

Running a simple 500 event run, it is immediately evident that the introduction of the Geant4 channeling routine has a very significant impact on the execution time: the simulation lasted 178 hours during which 16300 particles were processed, of which 7166 have a CPU tracking time greater than one second. Analysing these results in more detail, it can be seen that most of the slow particles are electrons created in the interaction of protons with silicon, many of which do not even leave the crystal. The first intervention that needs to be made to the simulation framework is therefore to introduce ways to speed up the runtime.

A simple workaround could be to apply cuts to certain parameters of the processed particles and stop processing those that do not fit these criteria. Since the goal is to have an estimate of the signal-to-background ratio that can be detected in a scoring plan after CRY2, it is important not to eliminate all secondary particles a priori. Instead, it would be useful for the purpose of this study to kill particles that have characteristics such that they do not hit the scoring plane and simply slow down the simulation. To understand the characteristics of such particles and optimise the cuts, a detailed study of the CPU simulation time is carried out.

The preliminary consideration that needs to be stressed is that in order to approach the problem of speeding up the simulation, it is only possible to intervene by modifying the source code of DD4hep. The Geant4 software, and consequently also its channeling routine, are assumed to be non-modifiable.

Since the standard DD4hep output file does not contain any Monte Carlo Truth information about what happens during the tracking, but only contains information about the start and end conditions, the following workaround is used. Taking advantage of the fact that the `begin()` and `end()` functions of the DD4hep classes *Run Action Sequence* and *Tracking Action Sequence* are always called at the

beginning and end of the entire run or tracking of each particle, respectively, a few lines of code have been inserted within these functions to save an output file of type `.root` to know some additional information about the particles.

In particular, a few lines of code were added within the `begin()` function of the Run Action Sequence to open a Geant4 root output file via the *G4 Analysis Manager* class. All variables to be stored must also be initialised in that function. Some additions are, also, made within the `end()` function of the *Tracking Action Sequence* to store information on the nature and characteristics of each track that is analysed by Geant. Attention must be paid to the fact that Geant and DD4hep handle particles differently (i.e. the ID is different). Then the `operator()` function of the *Stepping Action Sequence* class was also intervened in. This function is called at each step of the particle analysis, so, some if conditions are added to check which Volume the particle is in at that step. When or if the particle is within the analysed Volume, certain properties (such as momentum etc.) of the particle at that time are stored in new private variables of the class. The value of these variables is then retrieved and stored within the `end()` function of the *Tracking Action Sequence* class due to the fact that in DD4hep each class of type *Action* has access to all tracking, event, stepping, run and stacking action functions via the *Geant4 Context*. Finally, a few lines of code are added within the `process()` function of the Sensitive Action plugin relative to Trackers to store information on hits in scoring planes. A compiled version of DD4hep with these modifications can produce an output file containing the desired information on all particles processed by Geant4 that can be analysed separately.

Based on the results of the 500-event simulation, the first trivial check is to verify that each particle with a CPU tracking time $t_{CPU} \geq 1$ sec (i.e. the time between the execution of the `begin()` and `end()` function of the Tracking Action Sequence) is a particle that has been passed through the crystal. It can be concluded that it is precisely the introduction of the Geant4 channeling routine that has caused the slowdown, due to the high calculation time that is required to integrate the particle trajectory under channeling, dechanneling or volume reflection conditions.

Investigating the nature of these slow particles, it can be seen that most of the computationally problematic particles are electrons or positrons that are created by the interaction of primary protons with the electron cloud in the channel. Figure 4.1 shows the tracking time of slow particles distinguished by particle type, and a histogram of the tracking time is also shown separating the cases in which a particle under consideration is created or stopped within the crystal. Note that tracking primary protons is not a major computational problem.

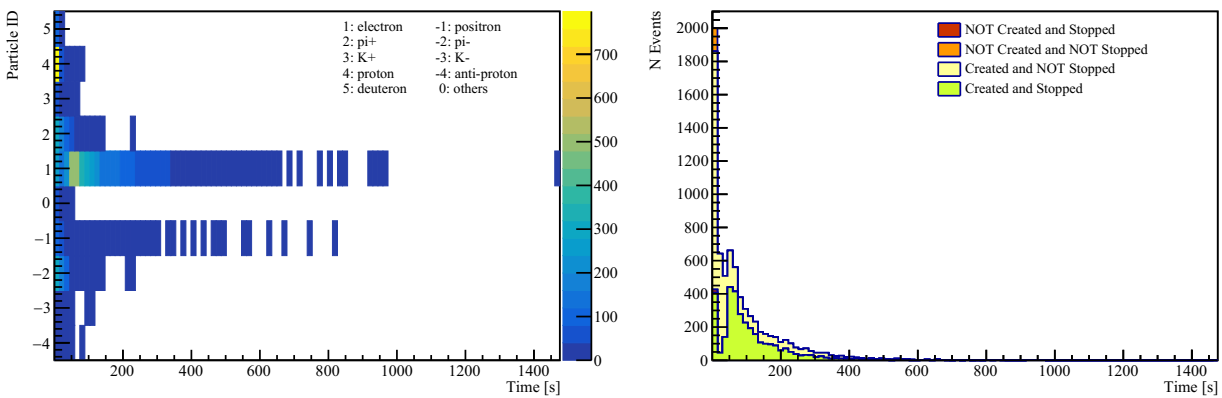


Figure 4.1: CPU tracking time of slow particles ($t_{CPU} \geq 1$ s) divided by particle ID and by creation status of a 500 event simulation performed with a 1 TeV proton gun and by using the Geant4 Channeling routine in CRY2.

It can be observed that a large number of particles with high tracking times have been created and stopped within the crystal, so they certainly do not contribute to the amount of background that can be observed in a scoring plane positioned after the crystal as it is not even possible for them to reach it. It would, therefore, be useful to find a way to block their tracking at the start to save time.

4.1. CPU time analysis

As can be seen in Figure 4.2, most of the particles created and stopped in the crystal were produced with low kinetic energy in the vertex compared to the entire energy range under consideration (up to 100 GeV). The same figure also shows the polar angle that the particles present at the vertex if created in the crystal, or that they present at the first step in the crystal if they come from outside.

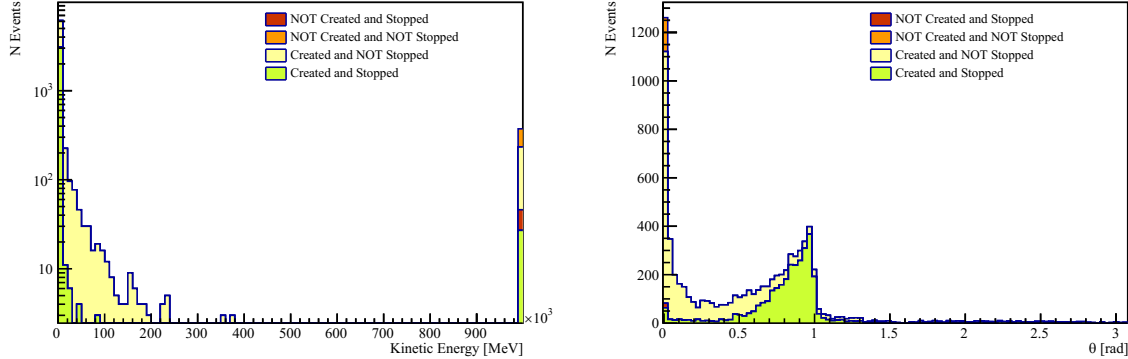


Figure 4.2: Kinetic energy and polar angle at the creation vertex of slow particles ($t_{\text{CPU}} \geq 1$ s) divided by creation status of a 500 event simulation performed with a 1 TeV proton gun and by using the Geant4 Channeling routine in CRY2

All subsequent discussion therefore focuses only on the analysis of charged particles created in the crystal (note that neutral particles are not subject to channeling). One possible approach to reduce the computational time of the simulation by eliminating the problematic particles described above is to apply cuts to the kinetic energy and polar angle that the particles present at the creation vertex. If these particles assume values that are above or below a preset threshold, their tracking is interrupted immediately at the first step. The thresholds for these two quantities must be set in such a way that they do not kill particles that can hit the scoring plane, since the objective is to estimate the signal-to-noise ratio. The histograms in Figure 4.3 show the values of kinetic energy and polar angle at the creation vertex by distinguishing particles according to whether they are fast or slow and according to whether they hit the scoring plane. The optimum situation would occur if the number of particles represented in yellow could be reduced without eliminating those represented in green. Based on the results of the 500-event simulation, the reduction in computing time is predicted if the charged particles created in the crystal, and all their daughter particles, which satisfy a variable cutoff were killed at the start. The cutoff value is represented by the vertical line in the histograms. The number of hits lost in each scenario is then calculated to study the impact of this suppression in a scoring plane having the dimensions of a VeloPix ASICs.

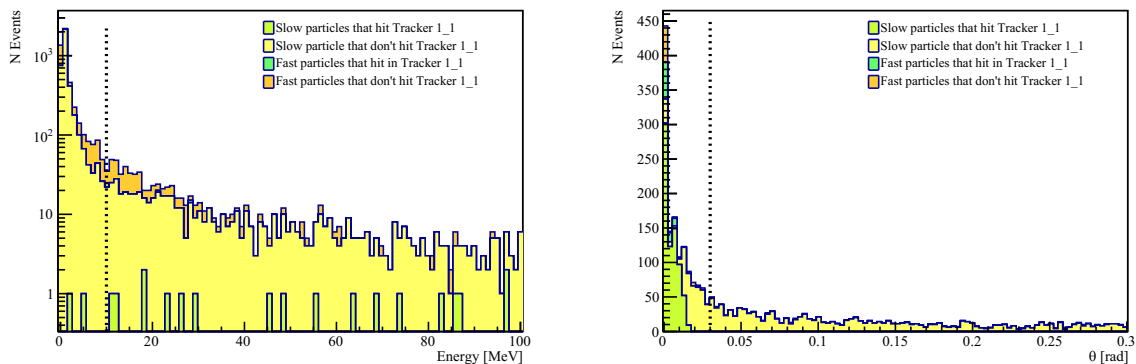


Figure 4.3: Kinetic energy and polar angle at the creation vertex of charged particles created in crystal divided by CPU speed and hit status in a tracker placed at $d = 1040$ mm from the centre of the crystal with the dimensions of a VeloPix of a 500 event simulation performed with a 1 TeV proton gun and by using the Geant4 Channeling routine in CRY2. Thresholds (dashed lines) are placed at $E_k > 10$ MeV and at $\theta < 0.03$ rad.

The results of optimising the tradeoff between reducing time and preventing the elimination of hitting particles are as follows: a cut-off is chosen on the kinetic energy at $E_k > 10$ MeV and on the polar angle at $\theta < 0.03$ rad. In the first case, the number of particles analysed is reduced from 16300 to 11513, losing 2 hits in VeloPix ($n_{\text{hits}} = 1018/1020$) and gaining an expected time reduction factor of 4.8. In the second case, the particles are reduced to a number of 1018, again losing 2 hits, but gaining an expected time reduction factor of 22.5. The two-dimensional histogram in Figure 4.4 shows the kinetic energy and polar angle at the vertex of the slow charged particles created in the crystal and their relative CPU tracking time. From these one can get an idea of the reduction in computation time by not considering particles below the energy threshold and above the angle threshold.

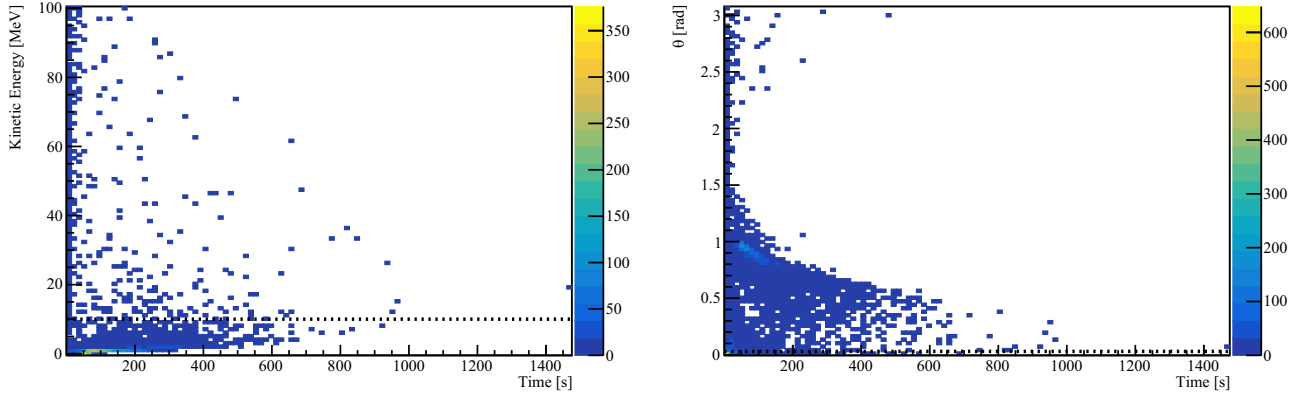


Figure 4.4: Kinetic energy and polar angle at the creation vertex of slow charged particles created in crystal as a function of the CPU tracking time of a 500 event simulation performed with a 1 TeV proton gun and by using the Geant4 Channeling routine in CRY2. Thresholds (dashed lines) are placed at $E_k > 10$ MeV and at $\theta < 0.03$ rad.

Note that there is a certain correlation between the two variables energy and angle. Looking at the Figure 4.5, it can be seen that the application of a cut on θ is, in the case of this choice of thresholds, more efficient in eliminating problematic particles.

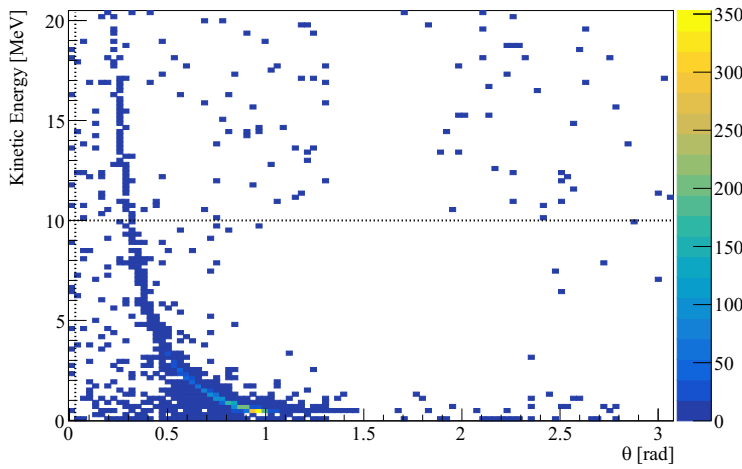


Figure 4.5: Kinetic energy versus polar angle at the creation vertex of slow charged particles created in crystal of a 500 event simulation performed with a 1 TeV proton gun and by using the Geant4 Channeling routine in CRY2. Thresholds (dashed lines) are placed at $E_k > 10$ MeV and at $\theta < 0.03$ rad.

New tests are conducted by introducing these cuts. In order to include in the simulation framework the possibility to stop the tracking of out-of-threshold particles, it is necessary to make use of a new plugin of type Stepping Action described in Section 3.2.2 that verifies the threshold conditions in the first step after the creation in the crystal.

4.1. CPU time analysis

In addition, the potential of parallel computation can be exploited to obtain a larger sample of events by making use of HTCondor [54], a software system that automates and manages High Throughput Computing workloads by effectively utilizing the computing power of network-connected machines, including clusters, cloud resources, and international grids.

A run consisting of 20 jobs of 100 events is performed by applying the cutoff on kinetic energy. it takes a total time of 96 hours by adding up the time of all the jobs. In proportion to the previous reference run of 500 events, in this case a reduction in computation time by a factor of 7.3 is obtained. On the other hand, in the case of applying the cut on the polar angle, a run of 17 jobs of 100 was performed, which takes a total of 49 hours and corresponds to a real reduction factor of 12.22, which is proportional to the reference run, i.e., less than the expected one. Note that these workarounds improve the execution speed but the computation time problem remains a major problem.

4.2 Simulations without the target

In this section, the analyses of a simulation reproducing the experimental characteristics of step (ii) of the proof of principles are presented. The reference run is performed with the following characteristics:

- CRY2 positioned with the vertical entry face at $z = 2$ cm.
- A proton gun of energy $E_p = 1$ TeV placed just before the entry face of the crystal that samples initial x , y , θ_x and θ_y of the primary particles from a Gaussian distribution defined with the parameters given in Table 3.1.
- A silicon scoring plane of dimensions $150 \times 150 \times 0.2$ mm³ placed at a distance $d = 1.04$ m from the centre of the crystal (Tracker1_4 described in Section 3.2).
- The application of a cutoff on the kinetic energy the particles have at the creation vertex $E_k > 10$ MeV.
- 2000 events in total, which constitute the results of 20 simulation jobs of 100 events run in parallel using HTCondor (simulation time of the parallel run $t_{\text{CPU}} \sim 7$ hours).

4.2.1 Signal and background analysis of 2000 events simulation

The distribution of hits in x , y and x vs y in the scoring plane is depicted in Figure 4.6. The distribution of the energy deposited in the silicon tracker by the incident particles in a restricted range of $[0; 50]$ keV is also shown (note that the total range is usually approximately $[0; 350]$ keV).

Note that for all subsequent graphs, an approximate digitisation of the hits in the scoring plane is performed. For each particle, a filter is applied to the energy deposited in the silicon, where the threshold is set at 1.8 keV corresponding to the VeloPix characteristic (see Section 2.4.3). Particles that hit the tracker but release less energy than the threshold (which is represented with a vertical line in the fourth plot in Figure 4.6) are not considered. Actually, to be more accurate, one would have to divide the tracker into regions corresponding to the size of a pixel and for each event calculate the total value of energy deposited; if the sum of the particle contributions is greater than the threshold then it is considered that there is a hit for that event in that pixel. One should also investigate the eventuality that a particle impacting at a large angle to the perpendicular to the tracker hits two or more adjacent pixels.

For these plots, a number of bins in x and y of $n_{\text{bins}} = 273$ is chosen. This corresponds to grouping 10 pixels in a bin, and is equivalent to considering the scoring plane divided into sensitive regions of size $550 \times 550 \mu\text{m}^2$.

Primary protons arriving from CRY1, impinging on CRY2 and hitting the tracker are shown in orange and represent what is considered as signal. Since, from the point of view of simulation, these protons are shot from the gun, they are identified by the fact of having `trackID = 0`. In contrast, particles that hit the scoring plane and possess `trackID ≠ 0` are not fired from the gun and thus constitute particles that are created in later stages of the simulation by the interaction of the primary protons with the crystal. They therefore constitute the background and are shown in yellow.

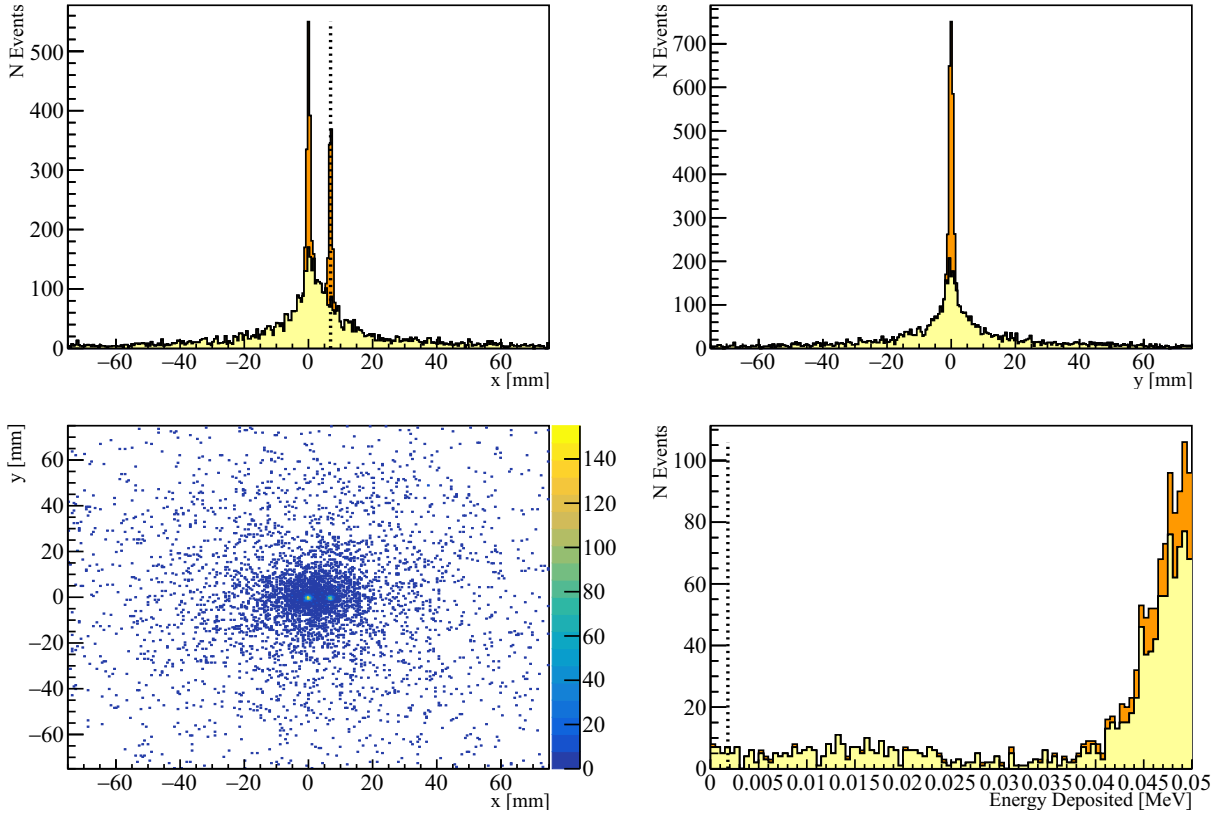


Figure 4.6: Hit distribution in x , y and xy per $550\text{ }\mu\text{m}$ of a tracker of dimensions $150 \times 150 \times 0.2\text{ mm}^3$ placed at a distance $d = 1.04\text{ m}$ from the centre of crystal of 2000 event simulation performed with a 1 TeV proton gun, by using the Geant4 Channeling routine in CRY2 and applying a cut on the kinetic energy of charged particles created in the crystal at $E_k > 10\text{ MeV}$. In orange are represented the primary protons coming from CRY1 and channeled or not by CRY2 (the dashed vertical line is where the peak of channeled particles is expected) and in yellow are represented the background particles created in the secondary interactions. The bottom right graph shows the energy deposit distribution of particles that hit the tracker. The vertical dotted line is at 1.8 keV .

Recall that in this simulation the crystal is positioned such that the bending plane corresponds to the xz plane. Thus, observing the distribution of hits in x one can clearly see, above the background, the peak of primary protons that have been deflected due to the crystal channeling phenomenon and the peak of those that have not been channeled. It is also observed that the cut on deposited energy affects only a small number of incident particles.

The two proton peaks exhibit a certain dispersion in both x and y . One can calculate the root mean square of the scattering angle due to the phenomenon of multiple scattering of a particle within a material with the experimental relation in Eq.(4.1),

$$\theta_{\text{rms}} = \frac{13.6\text{ MeV}}{\beta cp} z \sqrt{\frac{x}{X_0}} \left[1 + 0.038 \ln \left(\frac{xz^2}{X_0 \beta^2} \right) \right] . \quad (4.1)$$

Here z is the charge of incoming particle, x the traversed length in the material and X_0 is the radiation length of the material, that in the case of silicon corresponds to $X_{0,\text{Si}} = 9.37\text{ cm}$. Given the parameters in Table 2.2 and Table 2.3, knowing that in this case $cp = 1\text{ TeV}$ and that the length traversed by the particle corresponds to the z -dimension of the crystal, so $x = 70\text{ mm}$, and assuming $\beta \sim 1$, the value of the multiple scattering angle is found to be $\theta_{\text{rms},\text{Si}} = 8.33\text{ }\mu\text{rad}$. This value is small compared with the intrinsic dispersion due to the shape of the beam distribution, the parameters of which are given in Table 3.1. In particular, it is the contribution of the incoming beam's dispersion in position that dominates the spread in x and y in this case.

Histograms representing signal multiplicity and background multiplicity expected in a VeloPix ASIC are shown in Figure 4.7. Signal multiplicity refers to the number of particles hitting the tracker in

an event where the proton shot from the gun (i.e. which has `trackID = 0`) hits the detector. In this case, this occurs mainly when the primary proton is channeled and thus interacts little with the atoms of the crystal. Therefore, a low multiplicity composed mainly of electrons from the electron cloud in the channel is expected. Instead, background multiplicity means the number of particles hitting the detector in an event where the proton shot by the gun does not hit the detector. In such cases, it is probable that the primary proton has interacted by collision with a silicon nucleus and causes a shower of hadronic particles by strong interaction. A high multiplicity value is therefore expected in events such as this.

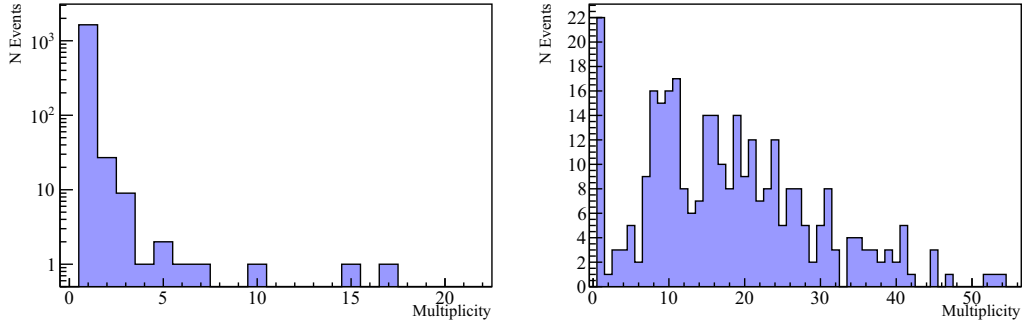


Figure 4.7: Multiplicity of the hits in a tracker of dimensions $14.08 \times 14.08 \times 0.2 \text{ mm}^3$ placed at a distance $d = 1.04 \text{ m}$ from the centre of crystal of a 2000 event simulation performed with a 1 TeV proton gun, by using the Geant4 Channeling routine in CRY2 and applying a cut on the kinetic energy of charged particles created in the crystal at $E_k > 10 \text{ MeV}$. The multiplicity in the case of a signal event, i.e., when there is a hit due to a primary proton, is shown on the left; that of the background is shown on the right. A hit threshold deposit of 1.8 keV is applied.

If, instead of considering the entire scoring plane, one restricts only to a tracker of size of a VeloPix, i.e., size $14.08 \times 14.08 \text{ mm}^2$, the expected x , y , x vs y and $E_{\text{deposited}}$ distributions are shown in Figure 4.8. In this case, the histogram bins are $n_{\text{bins}} = 256$ and each one corresponds exactly to one pixel of size $55 \times 55 \mu\text{m}^2$.

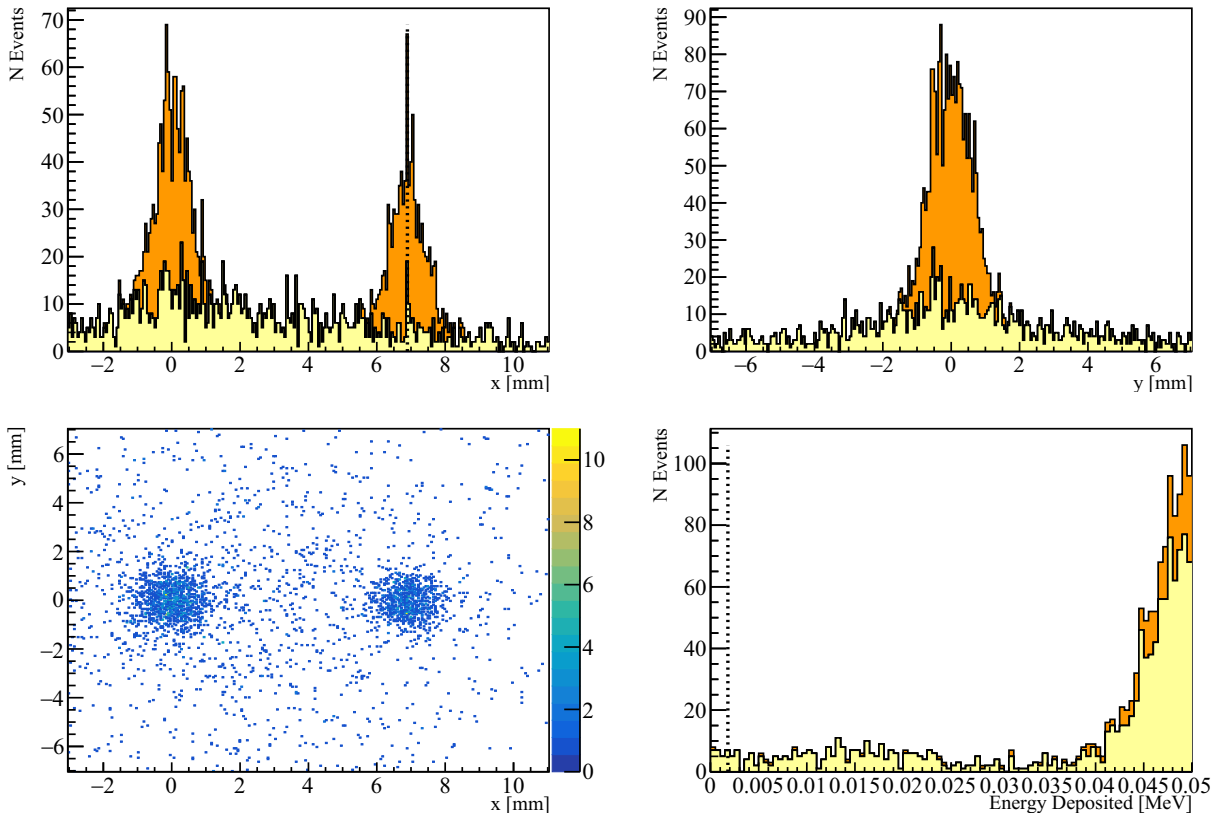


Figure 4.8: Hit distribution in x , y and xy per $55\text{ }\mu\text{m}$ of a tracker of dimensions $14.08 \times 14.08 \times 0.2\text{ mm}^3$ placed at a distance $d = 1.04\text{ m}$ from the centre of crystal of 2000 event simulation performed with a 1 TeV proton gun, by using the Geant4 Channeling routine in CRY2 and applying a cut on the kinetic energy of charged particles created in the crystal at $E_k > 10\text{ MeV}$. In orange are represented the primary protons coming from CRY1 and channeled or not by CRY2 (the dashed vertical line is where the peak of channeled particles is expected) and in yellow are represented the background particles created in the secondary interactions. The bottom right graph shows the energy deposit distribution of particles that hit the tracker. The vertical dotted line is at 1.8 keV .

Based on the results of this 2000-event simulation, it is possible to study conditions under which simple techniques can be applied to reduce the amount of background as early as the data acquisition stage. The idea is to consider only particles that fall within a certain symmetric interval around zero in the y dimension, since the signal proton beam has a very high peak in the origin. Another simple technique is to discard all events in which the total multiplicity of hits in the tracker is above a certain threshold, so that events in which the proton performs inelastic scattering with silicon nuclei destroying itself and producing background are not considered. To determine these thresholds, a varying cutoff is applied on the y position or total multiplicity of hits, and the Signal Efficiency, defined as the number of signal events remaining after the cutoff over the total number of signal events, and the Background Retention, defined as the number of background events remaining after the cutoff over the total number of background events, are studied as a function of the cutoff value. In Figure 4.9 are reported these quantities as function of the cutoff and one versus the other. In the first column of graphs is considered the case of cuts on $|y|$ in a range $[0.2; 2.0]\text{ mm}$ while in the second column is considered the case of cuts on multiplicity in a range $[2; 20]$.

Thresholds are chosen for a cutoff $|y| < 1.8\text{ mm}$ so as to maintain about 100% signal efficiency and a cutoff at $n_{\text{bkg}} \leq 11$, which corresponds to about 98% signal efficiency.

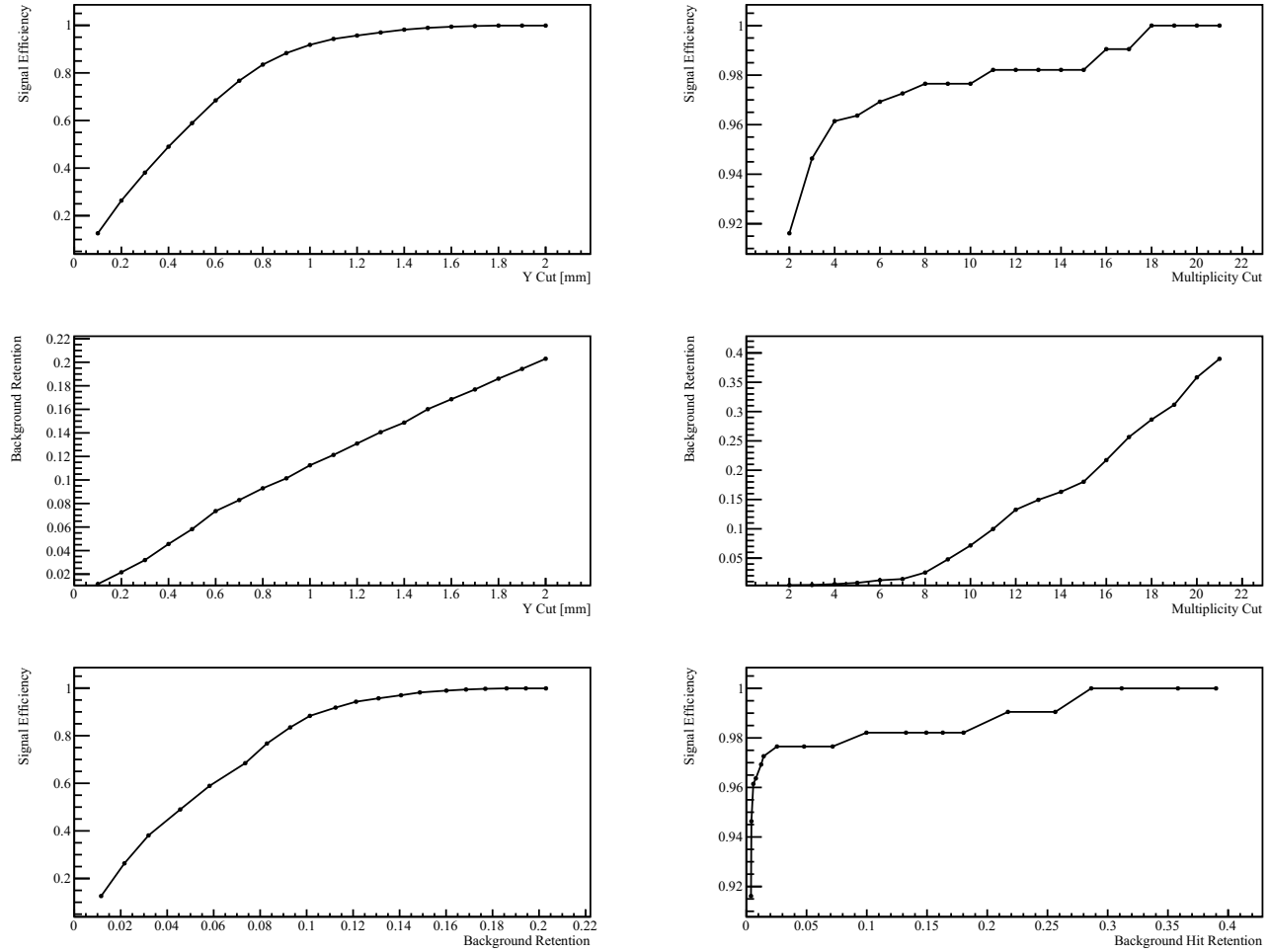


Figure 4.9: Study of signal efficiency and background retention under varying application of cutoff on Y position or total hit multiplicity per event basing on hits distributions in a tracker of dimensions $14.08 \times 14.08 \times 0.2 \text{ mm}^3$ placed at a distance $d = 1.04 \text{ m}$ from the centre of crystal of a 2000 event simulation performed with a 1 TeV proton gun, by using the Geant4 Channeling routine in CRY2 and applying a cut on the kinetic energy of charged particles created in the crystal at $E_k > 10 \text{ MeV}$.

4.2. Simulations without the target

Figure 4.10 shows what can be observed in the scoring plane after the simultaneous application of these two filters. This is to be compared with Figure 4.6.

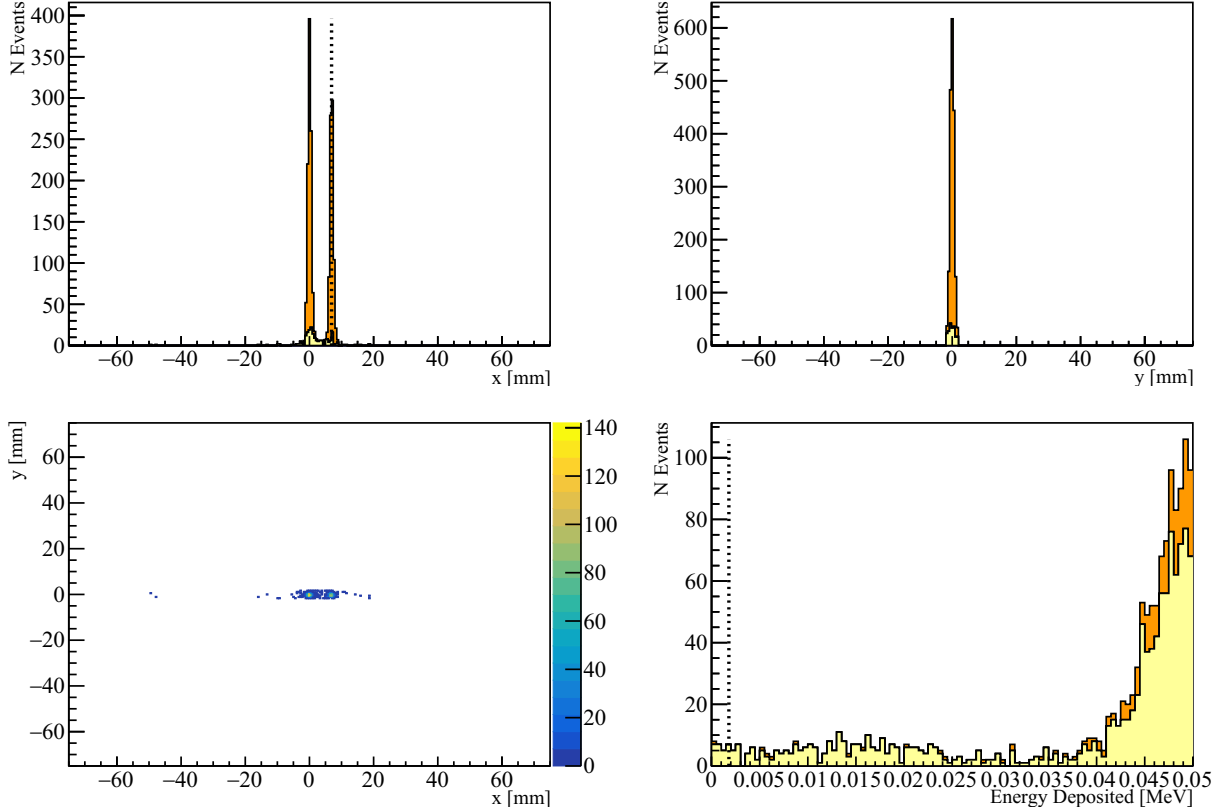


Figure 4.10: Hit distribution in x , y and xy per $550\text{ }\mu\text{m}$ of a tracker of dimensions $150 \times 150 \times 0.2\text{ mm}^3$ placed at a distance $d = 1.04\text{ m}$ from the centre of crystal of a 2000 event simulation performed with a 1 TeV proton gun, by using the Geant4 Channeling routine in CRY2 and applying a cut on the kinetic energy of charged particles created in the crystal at $E_k > 10\text{ MeV}$. In orange are represented the primary protons coming from CRY1 and channeled or not by CRY2 (the dashed vertical line is where the peak of channeled particles is expected) and in yellow are represented the background particles created in the secondary interactions. Cutoff are applied at $|y| < 1.8\text{ mm}$ and $n_{\text{bkg}} \leq 11$. The bottom right graph shows the energy deposit distribution of particles that hit the tracker. The vertical dotted line is at 1.8 keV .

It can be seen that the amount of background is dramatically reduced and the signal proton peaks are well defined. Figure 4.11 shows the histograms represented the multiplicity of signal and background in this case.

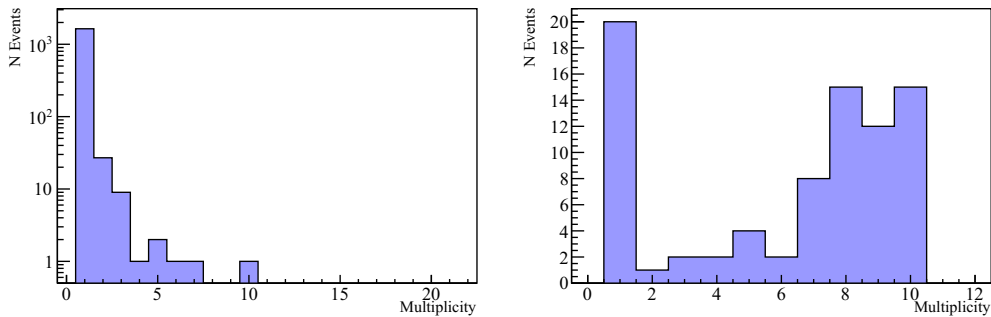


Figure 4.11: Multiplicity of the hits in a tracker of dimensions $150.0 \times 150.0 \times 0.2\text{ mm}^3$ placed at a distance $d = 1.04\text{ m}$ from the centre of crystal of a 2000 event simulation performed with a 1 TeV proton gun, by using the Geant4 Channeling routine in CRY2 and applying a cut on the kinetic energy of charged particles created in the crystal at $E_k > 10\text{ MeV}$. Cutoff are applied at $|y| < 1.8\text{ mm}$ and $n_{\text{bkg}} \leq 11$. The multiplicity in the case of a signal event, i.e., when there is a hit due to a primary proton, is shown on the left; that of the background is shown on the right. A hit threshold deposit of 1.8 keV is applied.

When considering a tracker the size of a VeloPix, what can be observed after the cuts $|y| < 1.8$ mm and $n_{\text{bkg}} \leq 11$ are applied can be seen in the histograms in Figure 4.12, in which each bin corresponds to one pixel.

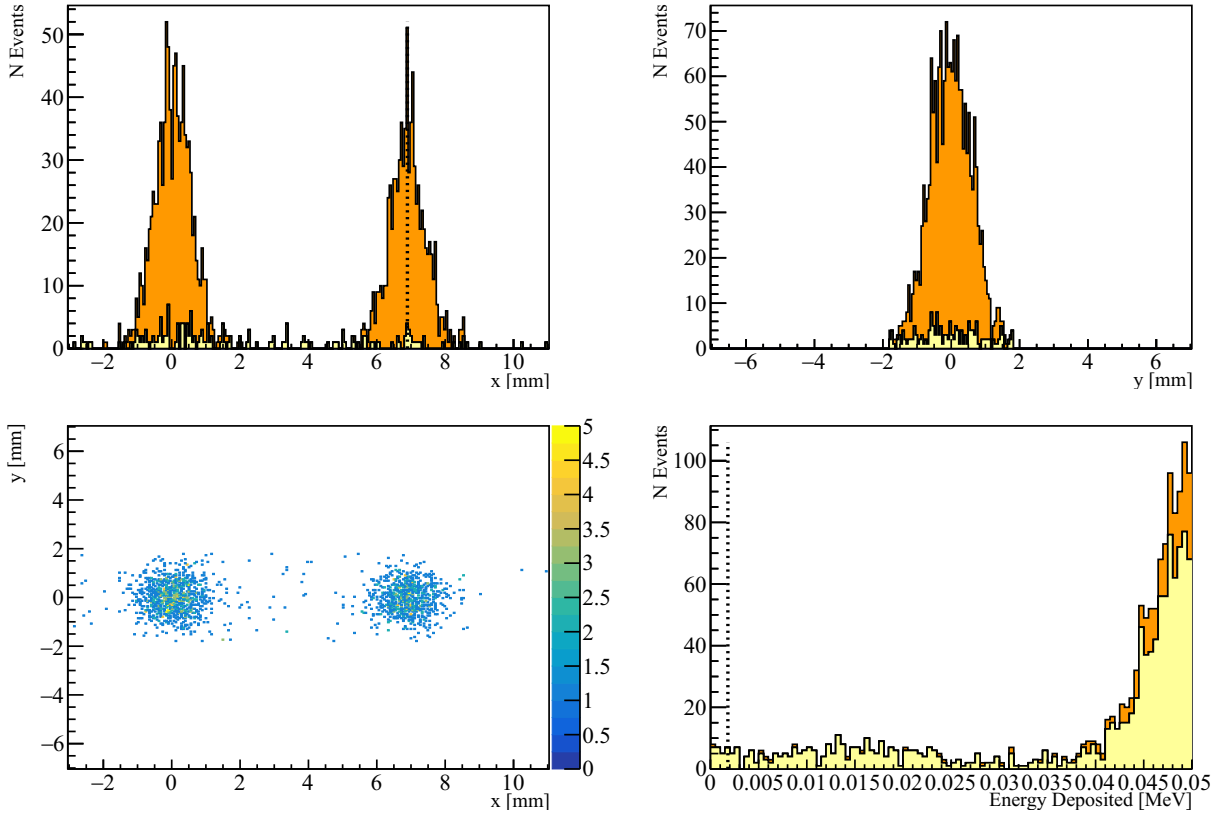


Figure 4.12: Hit distribution in x , y and xy per $55\mu\text{m}$ of a tracker of dimensions $14.08 \times 14.08 \times 0.2\text{ mm}^3$ placed at a distance $d = 1.04$ m from the centre of crystal of a 2000 event simulation performed with a 1 TeV proton gun, by using the Geant4 Channeling routine in CRY2 and applying a cut on the kinetic energy of charged particles created in the crystal at $E_k > 10$ MeV. In orange are represented the primary protons coming from CRY1 and channeled or not by CRY2 (the dashed vertical line is where the peak of channeled particles is expected) and in yellow are represented the background particles created in the secondary interactions. Cutoff are applied at $|y| < 1.8$ mm and $n_{\text{bkg}} \leq 11$. The bottom right graph shows the energy deposit distribution of particles that hit the tracker. The vertical dotted line is at 1.8 keV.

Figure 4.13 shows the histograms represented the multiplicity of signal and background in this case.

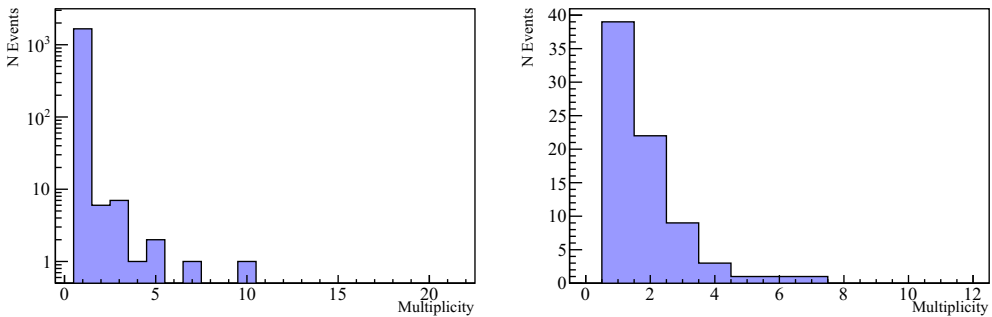


Figure 4.13: Multiplicity of the hits in a tracker of dimensions $14.08 \times 14.08 \times 0.2\text{ mm}^3$ placed at a distance $d = 1.04$ m from the centre of crystal of a 2000 event simulation performed with a 1 TeV proton gun, by using the Geant4 Channeling routine in CRY2 and applying a cut on the kinetic energy of charged particles created in the crystal at $E_k > 10$ MeV. Cutoff are applied at $|y| < 1.8$ mm and $n_{\text{bkg}} \leq 11$. The multiplicity in the case of a signal event, i.e., when there is a hit due to a primary proton, is shown on the left; that of the background is shown on the right. A hit threshold deposit of 1.8 keV is applied.

From the distribution of hits in x depicted in Figure 4.12, it is possible to provide an approximate estimate of the channeling efficiency of the crystal. The number of non-channelled particles is counted to be 924, while the number of channeled particles is 766, so we obtain an efficiency $\varepsilon_{\text{CRY2}} \sim 45\%$. This result appears to be overestimated compared to the predictions of [18], which presents values around $\sim 10\%$, although the simulation conditions differ in some aspects.

4.2.2 VELO Noise

This section discusses some analysis of VeloPix noise to see if it could affect a possible measurement in IR3 with a Velopix sensor. A root file of a *noise run* without beams, made in the winter of 2022 with the current full VELO in IP8 is provided¹. This file contains $5 \cdot 10^7$ events, where each event corresponds to a measurement taken for each clock cycle, random or successive, it does not matter for this case. Recall that one clock cycle of the LHC corresponds to 25 ns and that the LHCb VELO consists of 52 modules, each containing 4 sensors, of which 1 sensor is a tile with 3 VeloPix ASICs (see Section 2.4.3). The dataset is then composed of the hit number of each pixel (defined by row and column from 1 to 256), of each chip, of each sensor in each module.

An example of hit distribution of the total run in a random VeloPix ASICs is shown in Figure 4.14. These hits can be caused by noise in electronics, fluctuations in sensors, malfunctioning pixels, or other local effects.

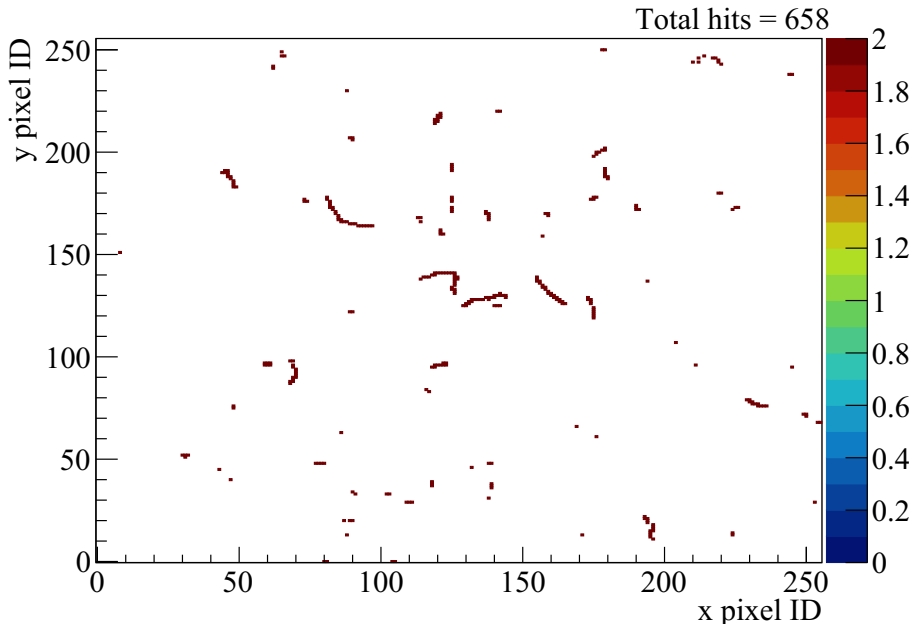


Figure 4.14: Hit distribution of module-25, sensor-3, ASICs-2 in $5 \cdot 10^7$ clock cycles run.

The expected number of hits per VeloPix chip per clock cycle is determined by blindly considering noise from all sources. A plot of the sum of all hits in the run divided by module per sensor and per ASICs is shown in Figure 4.15. It can be seen that some chips are particularly defect or sensitive to fluctuations, while most ASICs have a number of hits on the order of $10^2 - 10^3$. Averaging all modules, the mean number of noise hits per VeloPix per clock cycle results to be 0.0002. It can be concluded that this contribution is negligible.

¹Thanks to Victor Coco CERN-EP/LHCb/VELO

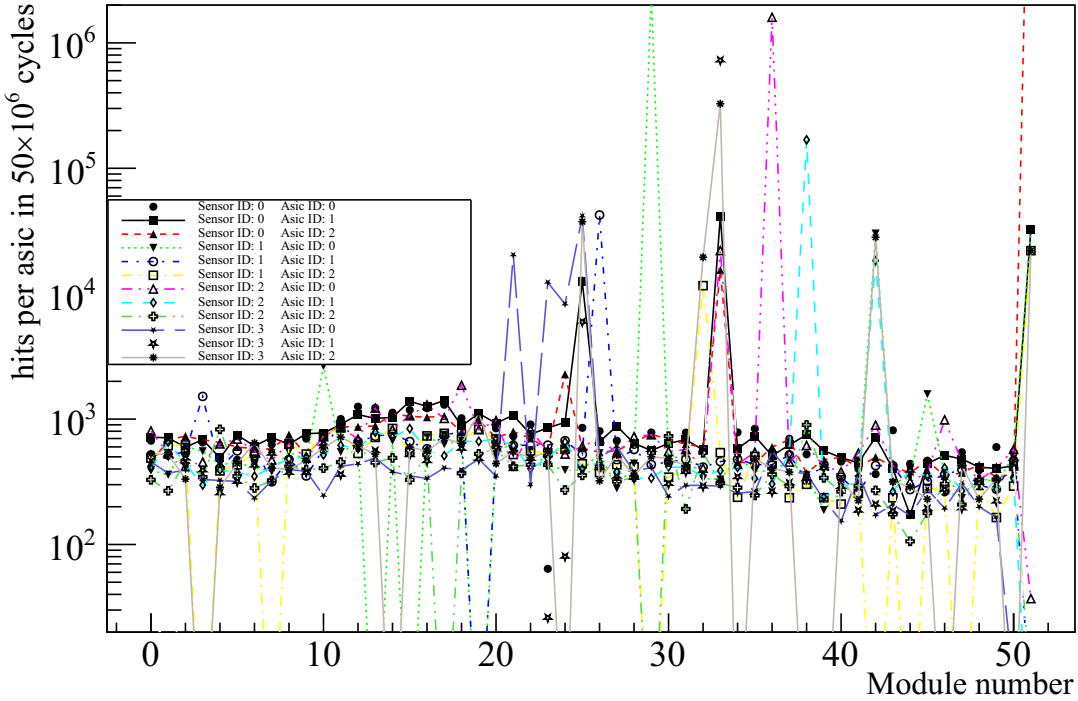


Figure 4.15: Total number of hits in a $5 \cdot 10^7$ clock cycles run, divided by module, sensor and ASICS ID.

4.3 Preliminary simulations with the target

Preliminary simulations are also carried out by introducing the target. In this case, the input interactions are to be read from a HepMC-format file containing the results of the simulation of proton-tungsten collisions at 7 TeV with the target at rest, performed with Pythia 8 Angantyr [51]. This particular file contains 1000. Each time the file is read, the primary interactions are merged into a single record and the primary particles and vertices created are passed to Geant4. To reproduce the conditions of a proton beam with Gaussian distribution in position and angles as given in Table 3.2 and to smear the interactions over the entire length L_T of the target, we made use of the new plugin described in Section 3.2.2.

Two baseline DD4hep simulation run are performed, set as follows:

- the tungsten target placed with the vertical entry face at $z = 0$ cm
- CRY2 positioned with the vertical entrance face at $z = 2$ cm, just after the target, with the Geant4 channeling routine enabled
- Primary vertices and particles read from the Pythia Argantyr file, where the reference proton energy is set to $E_p = 7$ TeV and the initial x, y, θ_x and θ_y of the primary interaction points are sampled from a Gaussian distribution defined with the parameters given in Table 3.2, while the initial z positions are according to Eq. (3.3)
- A silicon scoring plane of dimensions $150 \times 150 \times 0.2$ mm³ placed at a distance $d = 1.04$ m from the centre of crystal (Tracker1_4 described in Section 3.2).
- The application of a cutoff on the kinetic energy or o the polar angle that the charged particles created in the crystal have at the creation vertex at the threshold $E_k > 10$ MeV or threshold $\theta > 0.02$ rad.
- 103 events in the case of energy cutoff and 82 events in the case of polar angle cutoff, run in parallel using HTCondor, one event per job.

4.3. Preliminary simulations with the target

The resulting distribution of hits that can be observed in the tracker are shown in Figure 4.16 and Figure 4.17. Barplots representing the CPU total computing time of each event is also shown.

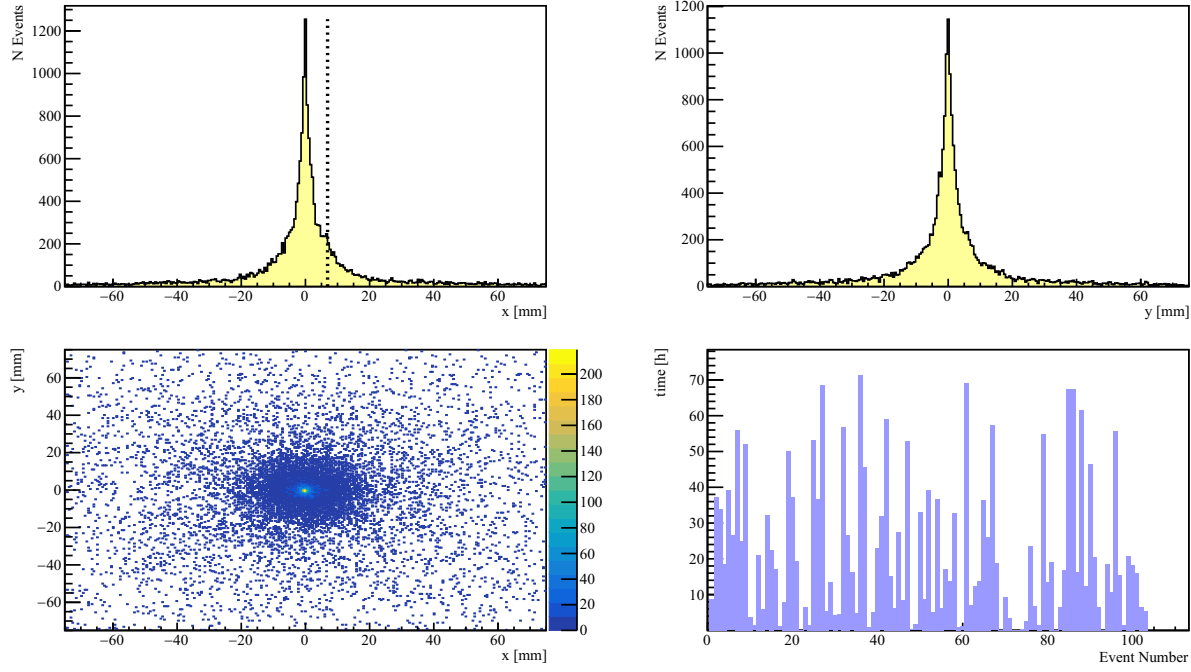


Figure 4.16: Hit distribution in x , y and xy per $550\text{ }\mu\text{m}$ of a tracker of dimensions $150.0 \times 150.0 \times 0.2\text{ mm}^3$ placed at a distance $d = 1.04\text{ m}$ from the centre of crystal of a 103 event simulation performed by reading primary events from a Pythia Argantyr file, by introducing the target and by using the Geant4 Channeling routine in CRY2. A cut on the kinetic energy of charged particles created in the crystal at $E_k > 10\text{ MeV}$ is applied. Barplot of CPU computation time in hours of processing each event.

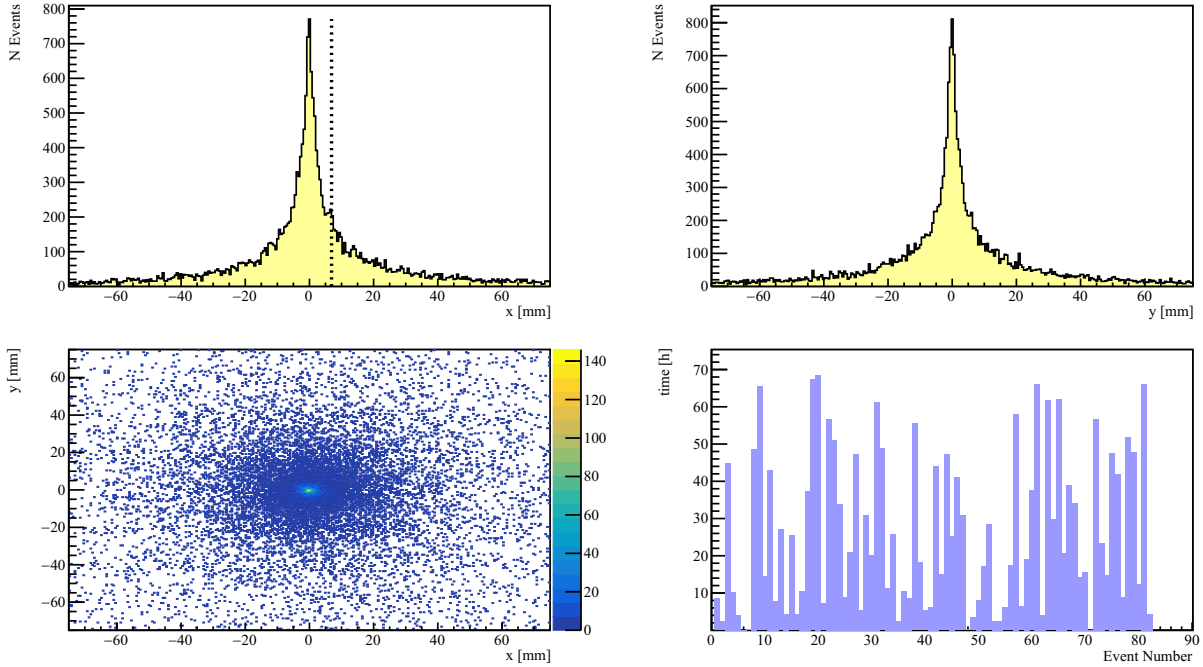


Figure 4.17: Hit distribution in x , y and xy per $550\text{ }\mu\text{m}$ of a tracker of dimensions $150.0 \times 150.0 \times 0.2\text{ mm}^3$ placed at a distance $d = 1.04\text{ m}$ from the centre of crystal of a 82 event simulation performed by reading primary events from a Pythia Argantyr file, by introducing the target and by using the Geant4 Channeling routine in CRY2. A cut on the polar angle of charged particles created in the crystal at $\theta > 0.02\text{ rad}$ is applied. Barplot of CPU computation time in hours of processing each event.

It turns out to be immediately obvious at a glance that the total number of hits is much greater in proportion to the previous case of the simulation run without a target. Furthermore, it can be concluded that there is no clear particle overdensity present above the statistical bin fluctuations where one would expect a peak in x . Despite the application of the cuts on computationally slow particles, the CPU time of the simulation is still extremely long with peaks reaching 70 hours per event. The Geant4 channeling routine is therefore not very practical to use in this way.

To investigate other methods of approach, the first step is to study the characteristics of the particles at the crystal entrance. To do this, a thin tracker² of the size of the crystal entrance face is inserted at the target exit. It is filled with vacuum so that it interacts as little as possible with the particles created in the target and entering the crystal. This tracker, in practice, simply represents a Geant4 volume that can be recognized within a modified Geant4 *Stepping Action Sequence* class, through which information about particles passing through the volume itself can be saved.

Two baseline DD4hep simulation run are performed, set as follows:

- the tungsten target placed with the vertical entry face at $z = 0$ cm
- CRY2 positioned with the vertical entrance face at $z = 2$ cm, just after the target, *without* the Geant4 channeling routine enabled as not to be slowed down by Geant4's channeling routine. In this case the crystal consists only in an amorphous block of silicon
- Primary vertices and particles read from the Pythia Argantyr file, where the reference proton energy is set to $E_p = 7$ TeV and the initial x, y, θ_x and θ_y of the primary interaction points are sampled from a Gaussian distribution defined with the parameters given in Table 3.2, while the initial z positions are according to Eq. (3.3)
- A silicon scoring plane of dimensions $150 \times 150 \times 0.2$ mm³ placed at a distance $d = 1.04$ m from the centre of crystal (Tracker1_4 described in Section 3.2).
- A vacuum tracker of dimensions $20 \times 40 \times 0.2$ mm³ just between the target and the crystal
- 500 events

²https://gitlab.cern.ch/elspadar/ir3detector/-/blob/temp_Chiara/sim/ddg4_ir3_crytrack.py.

4.3. Preliminary simulations with the target

The spatial distribution in the xy plane at the entrance of CRY2 of the interacting particles is shown in Figure 4.18.

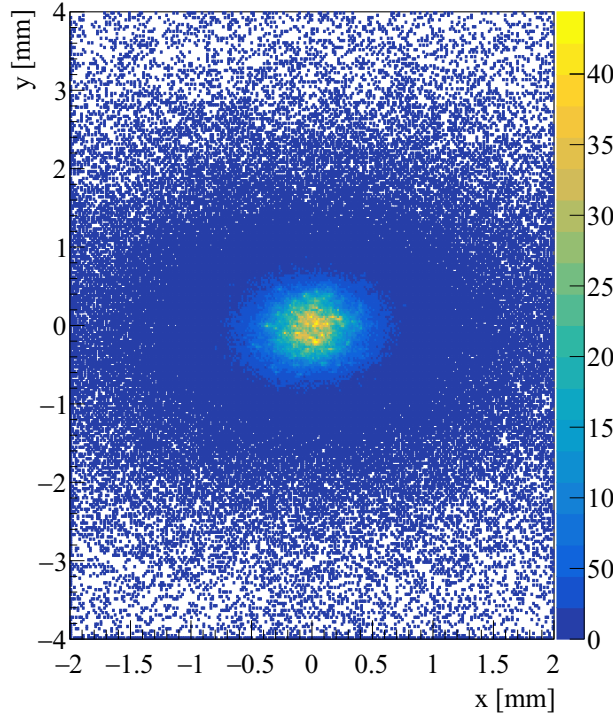


Figure 4.18: Distribution of hits in the xy plane of particles created by the interaction of primary particles read from the Pythia Argantyr file with the tungsten atoms at the crystal entrance in a 500-event simulation.

It can be seen from the Figure 4.19 that the number of particles created in the tungsten each event can reach very high values up to a maximum multiplicity of more than 6000 particles. Furthermore, it is observed that the majority of such particles are electrons and positrons created in shower interactions with tungsten.

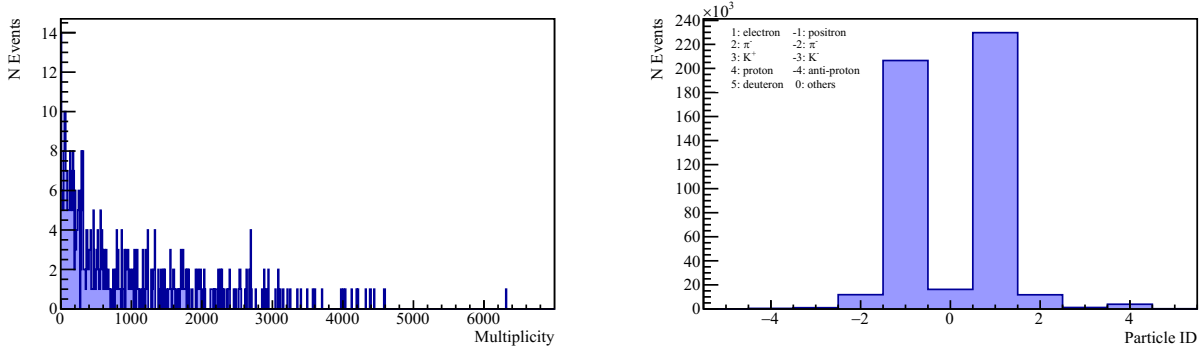


Figure 4.19: Distributions of multiplicity particle ID of particles created by the interaction of primary particles read from the Pythia Argantyr file with the tungsten atoms at the crystal entrance in a 500-event simulation.

The effect of the particle shower can also be seen in Figure 4.20, which shows the distributions of the positions in z , x , y and xy of the creation vertices of particles passing through the vacuum tracker. An exponential trend of the z position of the vertices due to the development of the hadronic shower is clearly visible from the first histogram. The two-dimensional histogram, on the other hand, shows that the majority of the particles are created in the central area of the target.

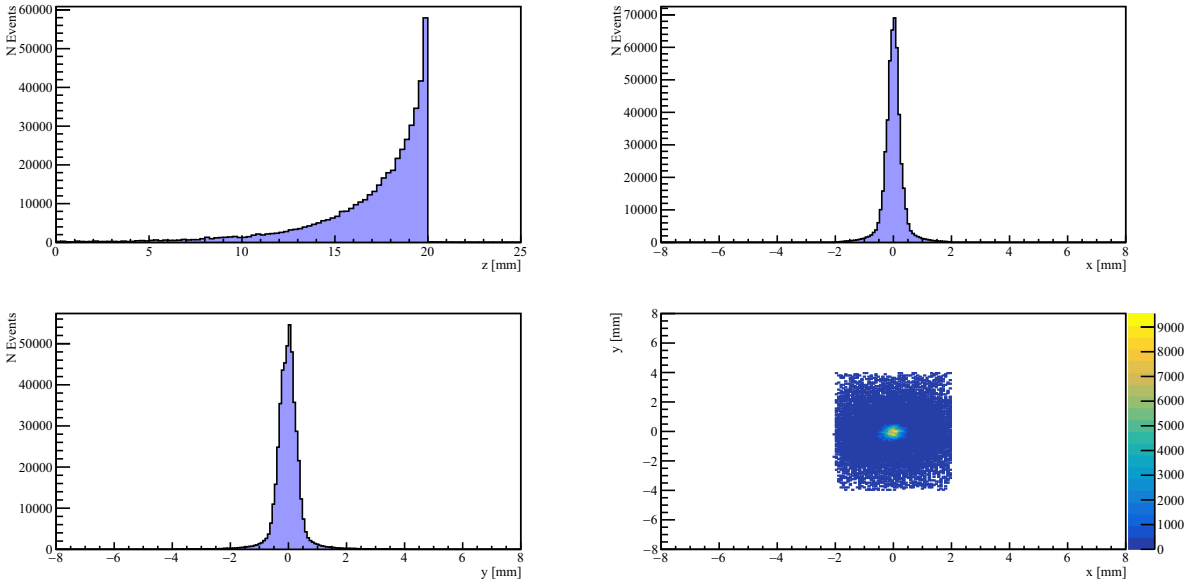


Figure 4.20: Distributions of the z , x , y and xy positions of the creation vertices of particles created by the interaction of primary particles read from the Pythia Argantyr file with the tungsten atoms that enter in CRY2 in a 500-event simulation.

The majority of particles pass through the vacuum tracker with total momentum less than 1 TeV, but a small number retain the initial energy of 7 TeV. The pseudorapidity trend follows what we expect under these kinematic conditions (Figure 4.21).

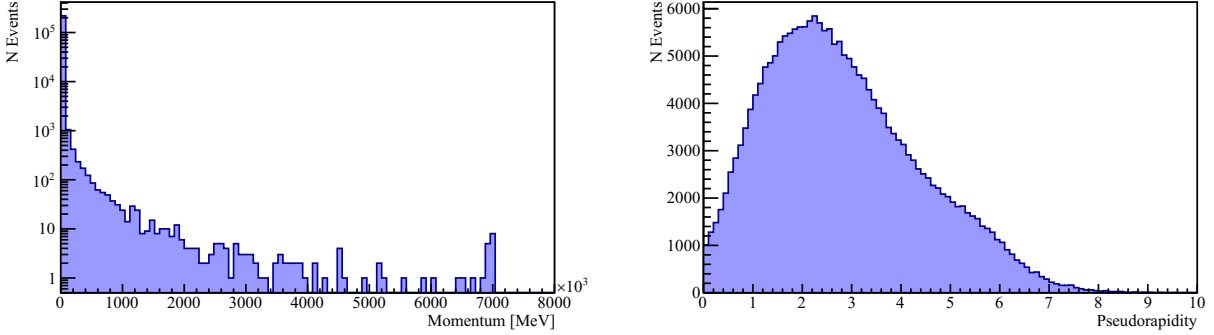


Figure 4.21: Distributions of momentum and pseudorapidity of interacting particles created by the interaction of primary particles read from the Pythia Argantyr file with the tungsten atoms at the crystal entrance in a 500-event simulation.

4.3.1 Channeling studies with an analytical approach

One possible method of studying the channeling phenomenon while avoiding using Geant's slow routine is to use an analytical approach based on the physical model of channeling described in Section 2.3.

The two key variables for assessing channeling conditions are the momentum and slope $\theta_x = p_x/p_{tot}$ of the particles as they enter the crystal. With the information obtained through the vacuum tracker, it is possible to study the number of particles in the channeling boundaries in the case of the simulation described in the previous paragraph: Figure 4.22 showing the two-dimensional moment-slope distribution over the whole possible range of assumed values and the same graph zoomed into a certain confined region.

The channeling condition is represented by the red curve, and its expression is obtained by combining the relationships describing the critical angle Eq.(2.35) in bent crystals and the critical radius Eq.(2.34):

$$\theta_c(pv) = \sqrt{\frac{2U(x_c)}{pv}} \left(1 - \frac{pv}{U'(x_c)} \cdot \frac{1}{R} \right) . \quad (4.2)$$

Entering the properties of silicon (Table 2.2) and the characteristics of CRY2 (Table 2.3) and assuming $v = c$, we obtain

$$\theta_c(p) = \sqrt{\frac{2 \cdot 1.6 \cdot 10^{-5} \text{ MeV}}{p}} \left(1 - \frac{p}{5.7 \cdot 10^3 \text{ MeV/cm}} \cdot \frac{1}{1 \cdot 10^3 \text{ cm}} \right) , \quad (4.3)$$

which is the expression of the red curve in Figure 4.22. Note that, in this case, the particle critical momentum is $p_c = 5.7 \text{ TeV}$ since $R > R_c$.

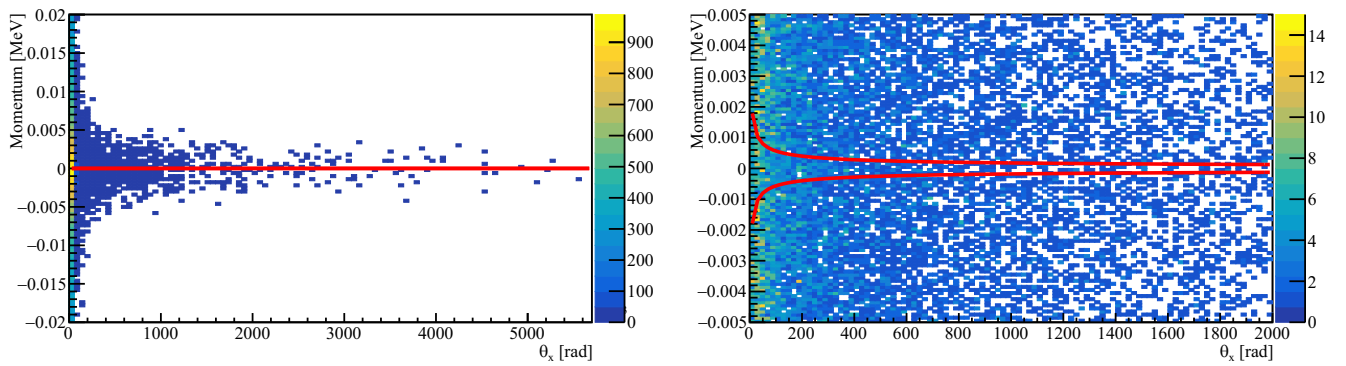


Figure 4.22: Distribution of momentum as function of slope in x of particles created by the interaction of primary particles read from the Pythia Argantyr file with the tungsten atoms at the crystal entrance in a 500-event simulation. The red curve represents the channeling condition of Eq.(4.3).

Among the positively charged particles, the number of those that fall within the channeling limits (are “channelable”), i.e., possess momentum and slope values within the red curve, is then calculated, named $\mathbf{N}_{\text{channelable}}$. Figure 4.23 compares the particle ID distribution at the crystal entrance of positively charged particles (right in Figure 4.23) versus that of the entire set of particles passing through the crystal (left in Figure 4.23).

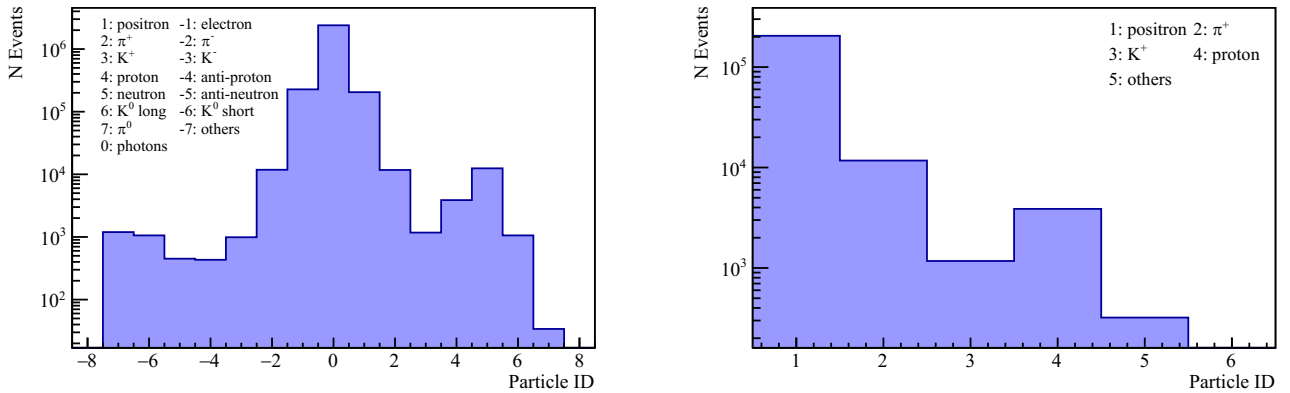


Figure 4.23: ID numbers of particles created by the interaction of primary particles read from the Pythia Argantyr file with the tungsten atoms at the crystal entrance in a 500-event simulation. On the left: all particles. On the right: only the positively charged.

For each of the channelable particles, it is possible to calculate the efficiency probability of Eq.(2.41), where we recall that the constant Θ_D for a Si(110) turns out to be

$$\Theta_D = \frac{4.526}{\ln(5907.51 \cdot \frac{E}{m}) - 1} . \quad (4.4)$$

At this point one can simulate the actual chance to be channeled of each channelable particle by throwing a random number between 0 and 1 and comparing it with the efficiency probability. The number of channelable particles called $N_{\text{channeled}}$ is then obtained.

By varying the offset of the channeling condition curve, which physically corresponds to tilting the input face of the crystal by an angle equal to the offset, one can replicate this simulation in different configurations. The results are shown in Table 4.1

offset [rad]	$N_{\text{channelable}}$	$N_{\text{channeled}}$
0	1270	8
0.0002	1308	7
0.0004	1298	3
0.0006	1283	5
0.0008	1272	3
0.001	1295	2
0.0012	1275	2
0.0014	1270	4
0.0016	1301	5
0.0018	1291	2
0.002	1237	1
0.0022	1229	1
0.0024	1248	4
0.0026	1265	1
0.0028	1276	0
0.003	1239	2
0.0032	1222	4
0.0034	1190	1
0.0036	1193	1
0.0038	1238	0
0.004	1180	2

Table 4.1: Results of channeling simulations by using the analytical approach varying the entrance angle offset. The total number of positively charged particles is 221914.

Note how, despite the elevated number of particles processed $N_{\text{tot}} = 221914$, only $\sim 0.6\%$ turn out to have the characteristics to be considered channelable. Furthermore, most of the channelable particles exhibit an efficiency probability very close to 0 so that only a small number of particles are expected to be actually channeled. The distribution of the efficiency probability of channelable particles in the case of the simulation with 0 rad offset, which expression is defined in Eq.(2.41), is shown in Figure 4.24.

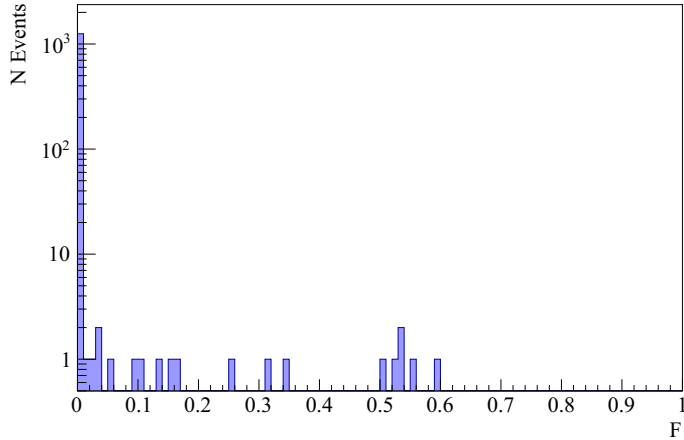


Figure 4.24: Efficiency probability F of channelable particles created by the interaction of primary particles read from the Pythia Argantyr file with the tungsten atoms at the crystal entrance in a 500-event simulation in the case of offset 0 rad.

The last step is to identify the hits in the scoring plane located at $d = 1040$ mm from the center of the crystal that correspond to the channeled particles and move them from their initial position by adding 7 mrad to the initial slope in the bending plane and manually shifting their position at the tracker.

The distribution of hits in the entire scoring plane before any shift is shown in Figure 4.25.

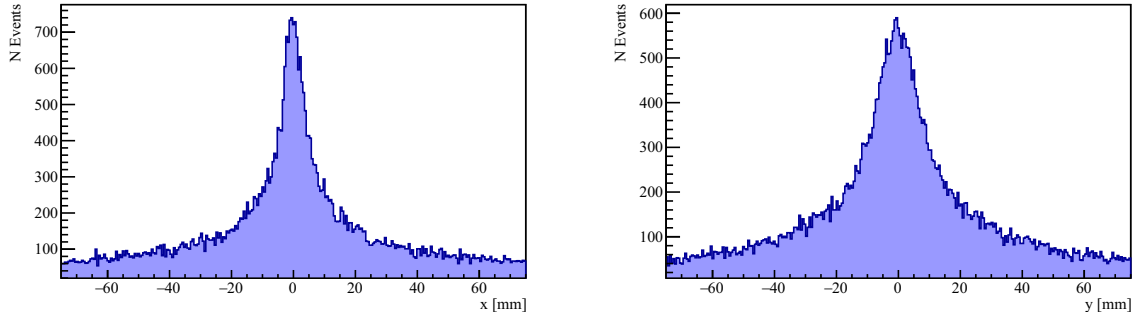


Figure 4.25: Hit distribution in x and y per $550\text{ }\mu\text{m}$ of a tracker of dimensions $150.0 \times 150.0 \times 0.2\text{ mm}^3$ placed at a distance $d = 1.04$ m from the centre of crystal of a 500 event simulation performed by reading primary events from a Pythia Argantyr file, by introducing the target and by considering CRY2 as an amorphous block of silicon.

Figure 4.26 and Figure 4.27 shows the x and y distributions of the hits in a scoring plane the size of a VeloPix (in which a bin corresponds to a pixel), in which the channeled particles (shown in orange) were shifted in the case of the simulation with offset 0 rad. The number of channeled particles is 8, which, compared with the total, is a very low value. As a consequence, in this case, one does not expect to see a significant bump in the distribution of hit position due to the channeling phenomenon. The signal-to-background ratio is unfavorable. One would have to acquire at least ~ 42000 events to produce a statistically significant bump around $x = 7$ mm.

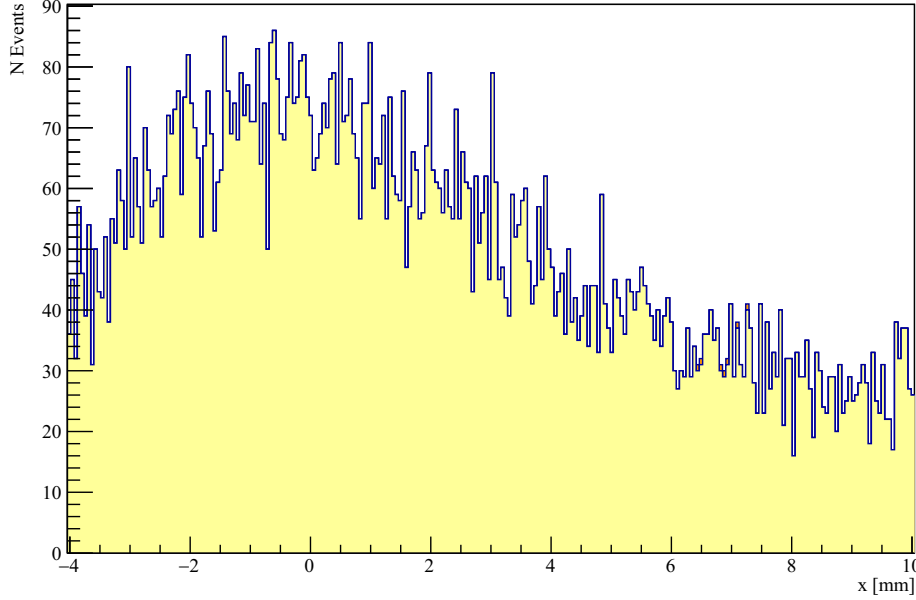


Figure 4.26: Hit distribution in x per $55\text{ }\mu\text{m}$ of a tracker of dimensions $14.08 \times 14.08 \times 0.2\text{ mm}^3$ placed at a distance $d = 1.04\text{ m}$ from the centre of crystal of a 500 event simulation performed by reading primary events from a Pythia Argantyr file, by introducing the target and by treating CRY2 in Geant4 as an amorphous block of silicon. The hit position distribution due to the unchanneled particles is shown in yellow. The one of the channeled particles (manually shifted in x) is shown in orange as increment.

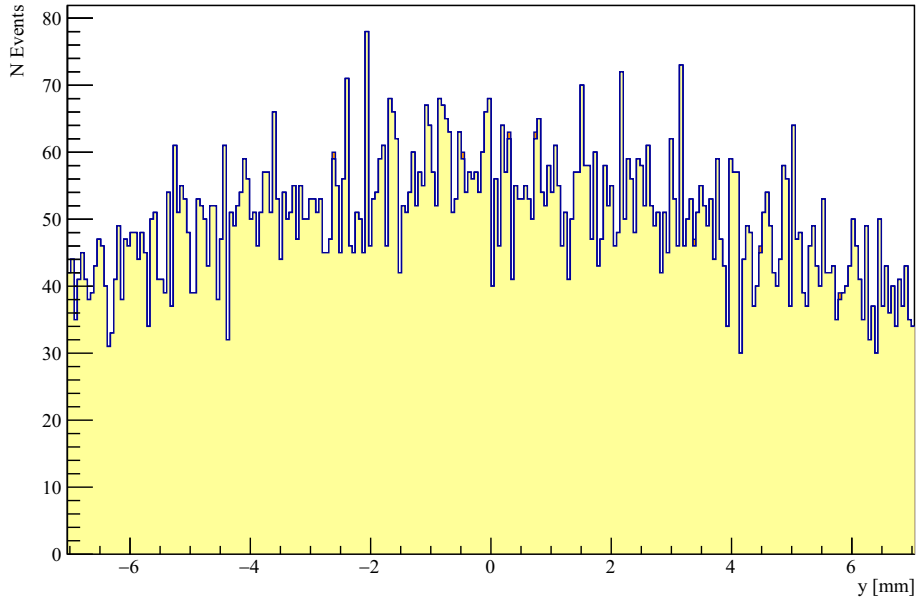


Figure 4.27: Hit distribution in y per $55\text{ }\mu\text{m}$ of a tracker of dimensions $14.08 \times 14.08 \times 0.2\text{ mm}^3$ placed at a distance $d = 1.04\text{ m}$ from the centre of crystal of a 500 event simulation performed by reading primary events from a Pythia Argantyr file, by introducing the target and by treating CRY2 in Geant4 as an amorphous block of silicon. The hit position distribution due to the unchanneled particles is shown in yellow. The one of the channeled particles (manually shifted in x) is shown in orange as increment.

Conclusions

An existing Geant4 crystal channeling physics routine was interfaced to DD4hep and can now be used. Simple examples were tested in DD4hep and results of the Geant4 routine reproduced.

However, the CPU computation time is very limiting, especially the use case where one needs to simulate background particles to study detector environment, even after applying cuts to the charged particles created in the crystal. A possible future work could be to study other types of cut to speed up the execution time even more. Another approach, which was not addressed in this work, could be to try to directly optimize the Geant4 Channeling Routine for the objectives of interest to the IR3 experiment simulation. For example, the number of steps in the integration of the trajectory oscillations that a particle has under channeling conditions can be optimized: at the moment the step length is hardcoded but could be put as an input parameter and optimized with respect to the goals. Alternatively, the use of this particular Geant4 channeling routine could be circumvented by implementing a model of the channeling phenomenon based on parametrization (see for example in Ref [5, 15]).

Regarding the proof of principle simulation of the IR3 experiment, it can be concluded that the presence of channeled protons should be clearly visible above the background in a VeloPix tracker when performing the first tests without the target. Noise due to fluctuations in the electronics should not afflict the measurements.

When introducing the target, the presence of channeled particles in events with a p-W interaction is much more hidden in the background due to the huge amount of secondary particles produced in the target and crystal. This also increases dramatically the CPU simulation time. It could be interesting to study how many tracking planes would be required to be able to identify clearly channeled particles (perhaps decaying particles) from a p-W interaction.

Bibliography

- [1] A. D. Sakharov, “Violation of CP Invariance, C asymmetry, and baryon asymmetry of the universe,” *Pisma Zh. Eksp. Teor. Fiz.*, vol. 5, 1967.
- [2] I. Khriplovich and A. Zhitnitsky, “What is the value of the neutron electric dipole moment in the Kobayashi-Maskawa model?,” *Physics Letters B*, vol. 109, Mar 1982.
- [3] J. Beacham *et al.*, “Physics Beyond Bolliders at CERN: Beyond the Standard Model Working Group Report,” *Journal of Physics G: Nuclear and Particle Physics*, vol. 47, Dec 2019.
- [4] J. M. Pendlebury *et al.*, “Revised experimental upper limit on the electric dipole moment of the neutron,” *Phys. Rev. D*, vol. 92, Nov 2015.
- [5] A. Merli, *Search for CP violation in the angular distribution $\Lambda_b^0 \rightarrow p\pi^-\pi^+\pi^-$ of baryon decays and a proposal for the search of heavy baryon EDM with bent crystal at LHCb*. PhD thesis, Università degli Studi di Milano - CERN, 2019.
- [6] E. G. Cazzoli, A. M. Cnops, P. L. Connolly, R. I. Louttit, M. J. Murtagh, R. B. Palmer, N. P. Samios, T. T. Tso, and H. H. Williams, “Evidence for $\Delta s = -\Delta q$ currents or charmed-baryon production by neutrinos,” *Phys. Rev. Lett.*, vol. 34, Apr 1975.
- [7] R. L. Workman *et al.*, “Review of Particle Physics,” *PTEP*, vol. 2022, 2022.
- [8] The BABAR Collaboration, “Precision measurement of the Λ_c^+ baryon mass,” *Phys. Rev. D*, vol. 72, Sep 2005.
- [9] V. Crede and W. Roberts, “Progress towards understanding baryon resonances,” *Rep. Prog. in Phys.*, vol. 76, June 2013.
- [10] A. S. Fomin, S. Barsuk, A. Y. Korchin, E. Kou, V. A. Kovalchuk, M. Liul, A. Natochii, E. Niel, P. Robbe, and A. Stocchi, “The prospect of charm quark magnetic moment determination,” *The European Physical Journal C*, vol. 80, May 2020.
- [11] The BESII Collaboration, “Measurement of higher-order multipole amplitudes in $\psi(3686) \rightarrow \gamma\chi_{c1,2}$ with $\chi_{c1,2} \rightarrow \gamma J/\psi$ and search for the transition $\eta_c(2s) \rightarrow \gamma J/\psi$,” *Physical Review D*, vol. 95, Apr 2017.
- [12] F. Sala, “A bound on the charm chromo-EDM and its implications.,” *J. High Energ. Phys.*, vol. 2014, Mar 2014.
- [13] S. Zhao, T. Feng, Z. Yang, *et al.*, “The one-loop contributions to c(t) electric dipole moment in the CP-violating BLMSSM,” *Eur. Phys. J. C*, vol. 77, Feb 2017.
- [14] F. J. Botella, L. M. G. Martin, D. Marangotto, F. M. Vidal, A. Merli, N. Neri, A. Oyanguren, and J. R. Vidal, “On the search for the electric dipole moment of strange and charm baryons at LHC,” *The European Physical Journal C*, vol. 77, Mar 2017.
- [15] E. Bagli, L. Bandiera, G. Cavoto, V. Guidi, L. Henry, D. Marangotto, F. Martinez Vidal, A. Mazzolari, A. Merli, N. Neri, and J. Ruiz Vidal, “Electromagnetic dipole moments of charged baryons with bent crystals at the LHC,” *Eur. Phys. J. C*, vol. 77, Dec 2017.

- [16] A. S. Fomin, A. Y. Korchin, A. Stocchi, O. A. Bezshyyko, L. Burmistrov, S. P. Fomin, I. V. Kirillin, L. Massacrier, A. Natochii, P. Robbe, W. Scandale, and N. F. Shul'ga, “Feasibility of measuring the magnetic dipole moments of the charm baryons at the LHC using bent crystals,” *Journal of High Energy Physics*, vol. 2017, Aug 2017.
- [17] The E791 Collaboration, “Multidimensional resonance analysis of $\Lambda_c^+ \rightarrow pK^-\pi^+$,” *Physics Letters B*, vol. 471, Jan 2000.
- [18] S. Aiola, L. Bandiera, G. Cavoto, F. De Benedetti, J. Fu, V. Guidi, L. Henry, D. Marangotto, F. Martinez Vidal, V. Mascagna, J. Mazorra de Cos, A. Mazzolari, A. Merli, N. Neri, M. Prest, M. Romagnoni, J. Ruiz Vidal, M. Soldani, A. Sytov, V. Tikhomirov, and E. Vallazza, “Progress towards the first measurement of charm baryon dipole moments,” *Phys. Rev. D*, vol. 103, Apr 2021.
- [19] The LHCb Collaboration, “LHCb SMOG Upgrade,” tech. rep., CERN, Geneva, 2019.
- [20] J. Lindhard, “Influence of Crystal Lattice on Motion of Energetic Charged Particles.,” *K. Dan. Viddensk. Selsk. Mat. Phys. Medd.*, vol. 34, no. 1, 1965.
- [21] V. M. Biryukov, Y. A. Chesnokov, and V. I. Kotov, *Crystal channeling and its application at high energy accelerators*. Springer, 1996.
- [22] D. Mirarchi, *Crystal collimation for LHC*. PhD thesis, Imperial College London - CERN, 2015.
- [23] W. Scandale, A. Vomiero, S. Baricordi, P. Dalpiaz, M. Fiorini, V. Guidi, A. Mazzolari, R. Milan, G. Della Mea, *et al.*, “Volume reflection dependence of 400 GeV/c protons on the bent crystal curvature,” *Phys. Rev. Lett.*, vol. 101, Dec 2008.
- [24] G. M. Wong, “Geant4 Crystal Channeling Study for Two Crystal Experiment at LHC IR3,” Aug 2022.
- [25] W. Scandale, D. A. Still, A. Carnera, *et al.*, “High-efficiency volume reflection of an ultrarelativistic proton beam with a bent silicon crystal,” *Phys. Rev. Lett.*, vol. 98, Apr 2007.
- [26] A. I. Sytov, V. Guidi, V. V. Tikhomirov, E. Bagli, L. Bandiera, G. Germogli, and A. Mazzolari, “Planar channeling and quasichanneling oscillations in a bent crystal,” *The European Physical Journal C*, vol. 76, Feb 2016.
- [27] The E761 Collaboration, “First observation of magnetic moment precession of channeled particles in bent crystals,” *Phys. Rev. Lett.*, vol. 69, Dec 1992.
- [28] D. Mirarchi, A. Fomin, S. Redaelli, and W. Scandale, “Layouts for fixed-target experiments and dipole moment measurements of short-living baryons using bent crystals at LHC,” *Eur. Phys. J. C*, vol. 80, Sept 2020.
- [29] W. Scandale, F. Cerutti, L. Esposito, M. Garattini, S. Gilardoni, D. Mirarchi, S. Montesano, S. Redaelli, R. Rossi, *et al.*, “The UA9 setup for the double-crystal experiment in CERN-SPS,” *Nuclear Instruments and Methods in Physics Research Section A: Accelerators, Spectrometers, Detectors and Associated Equipment*, vol. 975, Sept 2020.
- [30] W. Scandale, G. Arduini, M. Butcher, F. Cerutti, M. Garattini, S. Gilardoni, A. Lechner, R. Losito, A. Masi, D. Mirarchi, S. Montesano, S. Redaelli, R. Rossi, P. Schoofs, G. Smirnov, G. Valentino, *et al.*, “Observation of channeling for 6500 GeV/c protons in the crystal assisted collimation setup for LHC,” *Physics Letters B*, vol. 758, July 2016.
- [31] P. D. Hermes, K. Dewhurst, A. Fomin, D. Mirarchi, and S. Redaelli, “Layouts For Feasability Studies of Fixed-Target Experiments at the LHC,” in *Proc. IPAC’22*, no. 13 in Proceedings of the International Particle Accelerator Conference, JACoW, July 2022.

- [32] Q. Demassieux, K. Dewhurst, A. Fomin, P. D. Hermes, D. Mirarchi, and S. Redaelli, “[TCC-S/TCCP] Functional and operational conditions for the double-crystal setup in the LHC IR3,” 2022.
- [33] The LHCb Collaboration, “LHCb VELO Upgrade Technical Design Report,” tech. rep., 2013.
- [34] K. Hennessy, “LHCb VELO Upgrade,” *Nuclear Instruments and Methods in Physics Research Section A: Accelerators, Spectrometers, Detectors and Associated Equipment*, vol. 845, Feb 2017.
- [35] O. A. de Aguiar Francisco, W. Byczynski, *et al.*, “Microchannel cooling for the LHCb VELO Upgrade I,” *Nuclear Instruments and Methods in Physics Research Section A: Accelerators, Spectrometers, Detectors and Associated Equipment*, vol. 1039, May 2022.
- [36] M. Brice, “LHCb’s VELO metrology,” Feb 2022. General Photo.
- [37] A. Khalek *et al.*, “The ALFA Roman Pot detectors of ATLAS,” *Journal of Instrumentation*, vol. 11, Nov 2016.
- [38] M. Frank, F. Gaede, C. Grefe, and P. Mato, “DD4hep: A Detector Description Toolkit for High Energy Physics Experiments,” *Journal of Physics: Conference Series*, vol. 513, June 2014.
- [39] M. Frank, F. Gaede, M. Petric, and A. Sailer, “Aidasoft/dd4hep,” Oct 2018. Webpage: <http://dd4hep.cern.ch/>.
- [40] R. Brun, A. Gheata, and M. Gheata, “The ROOT geometry package,” *Nucl. Instrum. Meth. A*, vol. 502, Apr 2003.
- [41] The Geant4 Collaboration, “Geant4 — A simulation toolkit,” *Nuclear Instruments and Methods in Physics Research Section A: Accelerators, Spectrometers, Detectors and Associated Equipment*, vol. 506, July 2003.
- [42] M. Petrič, M. Frank, F. Gaede, S. Lu, N. Nikiforou, and A. Sailer, “Detector Simulations with DD4hep,” *Journal of Physics: Conference Series*, vol. 898, Oct 2017.
- [43] M. Frank, F. Gaede, N. Nikiforou, M. Petric, and A. Sailer, “DDG4 A Simulation Framework based on the DD4hep Detector Description Toolkit,” *Journal of Physics: Conference Series*, vol. 664, Dec 2015.
- [44] M. Dobbs and J. Hansen, “The HepMC C++ Monte Carlo event record for High Energy Physics,” *Computer Physics Communications*, vol. 134, Feb 2001.
- [45] E. Bagli, M. Asai, D. Brandt, A. Dotti, V. Guidi, and D. H. Wright, “A model for the interaction of high-energy particles in straight and bent crystals implemented in Geant4,” *The European Physical Journal C*, vol. 74, Aug 2014.
- [46] E. Bagli, M. Asai, A. Dotti, L. Pandola, and M. Verderi, “Allowing for crystalline structure effects in Geant4,” *Nuclear Instruments and Methods in Physics Research Section B: Beam Interactions with Materials and Atoms*, vol. 402, July 2017. Proceedings of the 7th International Conference Channeling 2016: Charged and Neutral Particles Channeling Phenomena.
- [47] E. Bagli, V. Guidi, and V. A. Maisheev, “Calculation of the potential for interaction of particles with complex atomic structures,” *Phys. Rev. E*, vol. 81, Feb 2010.
- [48] W. Scandale, A. Vomiero, S. Baricordi, P. Dalpiaz, M. Fiorini, V. Guidi, A. Mazzolari, R. Milan, G. D. Mea, *et al.*, “Observation of nuclear dechanneling for high-energy protons in crystals,” *Physics Letters B*, vol. 680, Sept 2009.
- [49] D. Lingis, M. Gaspariūnas, A. Plukis, and V. Remeikis, “Improvements and validation of particle channeling model in GEANT4,” *Nuclear Instruments and Methods in Physics Research Section B: Beam Interactions with Materials and Atoms*, vol. 525, Aug 2022.

- [50] W. Scandale, A. Carnera, G. Della Mea, D. De Salvador, R. Milan, A. Vomiero, *et al.*, “Deflection of 400 GeV/c proton beam with bent silicon crystals at the CERN Super Proton Synchrotron,” *Phys. Rev. ST Accel. Beams*, vol. 11, June 2008.
- [51] C. Bierlich, G. Gustafson, L. Lönnblad, and H. Shah, “The Angantyr model for heavy-ion collisions in Pythia8,” *Journal of High Energy Physics*, vol. 2018, Oct 2018.
- [52] R. D. Maria *et al.*, “SixTrack Version 5: Status and New Developments,” in *Proc. IPAC’19*, Proceedings of the International Particle Accelerator Conference, JACoW, May 2019.
- [53] K. Dewhurst *et al.*, “Performance of a double-crystal setup for LHC fixed-target experiments,” in *Proc. IPAC’23*, Proceedings of the International Particle Accelerator Conference, JACoW, May 2023.
- [54] D. Thain, T. Tannenbaum, and M. Livny, “Distributed computing in practice: the condor experience..,” *Concurrency - Practice and Experience*, vol. 17, Apr 2005.